Photon Induced Coherence Loss in Atom Interferometry

by

Michael S. Chapman

A.B., Columbia University (1984)
B.S., Columbia University (1985)

Submitted to the Department of Physics
in partial fulfillment of the requirements
for the degree of

DOCTOR OF PHILOSOPHY

at the

MASSACHUSETTS INSTITUTE OF TECHNOLOGY

May 1995

Signature of Author _____
Department of Physics
May 31, 1995

Certified by _____
David E. Pritchard
Professor of Physics

Accepted by _____
George F. Koster
Chairman, Department Committee
on Graduate Studies

Photon Induced Coherence Loss in Atom Interferometry

by

Michael S. Chapman

Submitted to the Department of Physics
on May 31, 1995, in partial fulfillment
of the requirements
for the degree of
Doctor of Philosophy

Abstract

This thesis reports a study of the effects of spontaneous scattering of photons on the atomic coherences in an atom interferometer. We scattered single photons from the atoms in an atom interferometer and observed contrast loss and revivals that are directly related to the spatial separation of the deBroglie waves. We demonstrated that the fringe visibility can be *recovered* by detecting only the atoms which are correlated with photons emitted into a limited range of final directions. Other topics of research covered in this thesis are a demonstration of a separated-beam molecular interferometer and a near-field interference phenomena known as the Talbot effect.

Thesis supervisor: David E. Pritchard
Professor of Physics

to Elizabeth
and my family

Table of Contents

1. Introduction 9

1.1 Outline 9

1.2 Historical Background 10

1.3 The MIT Interferometer 13

2. Loss of Coherence in an Atom Interferometer due to Scattering a Single Photon 19

2.1. Introduction and Historical Background 19

2.2. Photon Scattering from Atoms in an Atom Interferometer: Coherence Lost and Regained (submitted for publication) 22

2.3. Theory 36

2.3.1. Loss of coherence due to entanglement with scattered photons 36

2.3.2. Recovering the lost coherence in a correlation experiment 55

2.4. Experimental Details 70

2.4.1 The MIT atom interferometer 70

2.4.2 Scattering a single photon 79

2.5. Additional Data 90

2.6. Discussion 94

3. Molecular Interferometry 99

3.1. Introduction 99

3.2. Optics and Interferometry with Na2 Molecules (to appear in Phys. Rev. Lett.) 102

3.3. Additional Data 117

4. The Talbot Effect 125

4.1. Introduction and Background 126
4.2. Near Field Imaging of Atom Diffraction Gratings: the Atomic Talbot Effect, Phys. Rev. A 51, R14 (1995) 130
4.3. Basic Theory 145
4.4. Numerical Calculations 148
Appendix A: Na Polarizability Reconsidered 153
Appendix B 165
B.1 Using a separated beam interferometer to measure tensor components of the electric polarizability of molecules. 165
Acknowledgments 171
References 173

1. Introduction

This thesis describes new experimental results in the emerging field of atom interferometry. The experiments described herein represent a major step forward in investigating some important problems in fundamental quantum mechanics such as the mechanism for the loss of coherence in quantum systems and the possible limits of quantum interference imposed by system size or complexity.

We have directly studied the loss of atomic coherence due to entanglement between two systems by scattering single photons from the atoms. We have demonstrated that the loss of interference depends on the spatial separation of the atom waves at the point of scattering. Furthermore, we have been able to recover the lost atomic interference in a novel correlation experiment by observing only the atoms correlated with photons scattered in certain directions.

We have also demonstrated the first molecular interferometer relying exclusively on interferences of center-of-mass coordinates. We observed high contrast molecular interference fringes despite the considerable increase of system size and complexity compared with atomic systems. Our measurement of the index of refraction for molecule waves demonstrates the potential of separated-beam molecular interferometry as a powerful tool in the field of molecular physics.

1.1 Outline

This thesis is divided into 4 chapters including this introduction. In this introduction, I will provide a short historical background of the field of atom

interferometry and an introduction to the interferometer we have developed at M.I.T. Chapter 2 describes our experimental investigation of the loss of atomic coherence in an atom interferometer due to photon scattering. Chapter 3 discusses the demonstration of the first molecular interferometer and a measurement of the index of refraction of neon gas for Na_2 deBroglie waves. Chapter 4 describes our demonstration of a self-imaging phenomena known as the Talbot effect that occurs in the near-field of a periodic diffractive object. I will conclude with a brief summary and outlook. Appendix A describes data analysis we undertook to verify the results of our measurement of the electric polarizability of sodium—the first atom interferometer experiment performed with physically isolated beams. Appendix B describes a method to measure the tensor components of the electric polarizability of molecules.

1.2 Historical Background

The field of atom interferometry can mark its beginning in 1991 with the demonstration of 4 different atom interferometers by groups in Konstanz [CAM91], Stanford [KAC91], Braunschweig [RKW91] and our group at MIT [KET91]. Two of these interferometers operate exclusively in the center-of-mass coordinates of the atoms and hence have direct light wave analogies, namely the Young's two slit experiment (Konstanz) and the Mach-Zender interferometer (MIT). The other two rely upon the interference of entangled states of internal and external degrees of freedom of the atom and are closely related to Ramsey's technique of separated oscillatory fields.

Several other atom interferometers were reported shortly after these initial demonstrations. They include a two-slit experiment using atoms dropped from a MOT [SST92], a longitudinal Stern-Gerlach experiment [RMB91], and 4-zone optical Ramsey experiment [SSM92]. Additionally, Clauser et al [CLL94] have demonstrated a near-

field three grating interferometer which is related to the Talbot effect, the near field self-imaging of a periodic structure. The technique of adiabatic passage has been used for an interferometer featuring beam splitters with very large momentum transfer [WYC94]. Recently, Kapitza-Dirac diffraction from a standing light wave has been employed to realize a three grating interferometer in Innsbruck.†

Several other groups are in the process of developing atom interferometers. A group in Colorado is pursuing a three-grating interferometer employing Bragg reflection from a standing light wave.* In Oregon, a slow atom version of our interferometer is being constructed.** One group is pursuing He diffraction from a cleaved crystal surface,*** while another is using "diffraction" from a time-dependent evanescent wave mirror [HSK94]. In the short span of 4 years, there have been 14 different atom interferometers either planned or demonstrated, employing 10 different physical mechanisms to coherently manipulate the atoms. The wide variety of techniques that can be used to create atomic interferences underlies one of the distinctions between atom interferometry and its electron and neutron predecessors.

Why all the interest and activity in atom interferometers? Aside from the compelling appeal of demonstrating quantum mechanical interference of such a complicated entity, the long term interest in the field will be ultimately based on the potential applications of atom interferometers to questions and measurements in both basic physics and applied technology. Already atom interferometers have been used in a number of such applications. They include the demonstration of a gravimeter with a

---

† J. Schmiedmayer, personal communication

* D. Gitner et al., from a talk at OSA94, Dallas, session ThAAA5

** T. Swanson, et al. from a talk at IQEC94, Anaheim, session QTuC7

*** J. Franson, personal communication.

precision of ~3 x $10^{-8}g$ [KAC92], a precision measurement of the photon recoil velocity [WYC93] and our measurements described below.

In our laboratory, we focused our efforts on developing an atom interferometer with physically separated and isolated interfering amplitudes, and subsequently performed several experiments with this unique interferometer [EKS93]. The first was a precision measurement of the ground state electric polarizability of sodium [ESC95]. Our measurement, with an overall accuracy of 0.35%, was over 20 times more accurate than the previous best absolute measurement [HAZ74], and 7 times more accurate than the previous accepted value obtained from a comparison of relative measurements of the polarizabilities of Na and He^* to the theoretically calculated polarizability of He^* [MSM74]. The increased accuracy of our measurement allows us to discriminate between ten or so theoretical calculations of this important atomic parameter.

While our first experiment demonstrated the potential for improved precision in atomic metrology, the next demonstrated that entirely new measurements become possible with a separated beam atom interferometer. In this experiment, we measured the index of refraction of various gases as seen by sodium matter waves [SCE95]. We developed semi-classical models to compare our results with theory which revealed that our measurements were especially sensitive to the long-range shape of the atom-atom potential, in contrast to most spectroscopic determinations of these potentials.

We also demonstrated a novel rephasing experiment by applying a differential magnetic field to the arms of the interferometer [SEC94]. In this experiment, the different ground state magnetic sublevels initially dephase due to their different magnetic projections. However, for applied fields for which the phase applied to all sublevels is an integer multiple of 2π, there is a dramatic rephasing or revival of the atomic interference

signal. We have extended this idea of "contrast interferometry" in a theoretical study of a new method to measure dispersive phase shifts [HPC95].

After having demonstrated the potential of our interferometer for measurements of atomic properties, we wished to turn our attention to problems in fundamental quantum mechanics which could be addressed with such a device. Two studies of this type form the heart of this thesis: a detailed study of the effects on the atomic interference due to entanglement with a large reservoir (free space modes of the vacuum radiation field) and a demonstration of a molecular interferometer operating exclusively in the external coordinates space of the molecules.

1.3 The MIT Interferometer

Before going on to describe the experiments undertaken for this thesis, it would be appropriate to describe briefly the atom interferometer we have developed at M.I.T. It was first demonstrated in 1991 and is described in detail in [KET91], [KEI91].

Our interferometer is the direct atom analog to the optical three grating Mach-Zender interferometer. Our interferometer uses binary amplitude gratings (i.e. slotted membranes) with sub-micron periods to diffractively split and recombine the atom beam as shown in Fig. 1.1. It is a feature of this type of interferometer that an interference pattern with the same spatial period as the gratings is formed at the plane of the third grating. The atomic interference pattern could be detected by scanning a narrow detector in this plane, however we use the third grating to mask the pattern. Atomic interference is detected by measuring the total transmitted atomic flux while varying the relative position of the gratings.

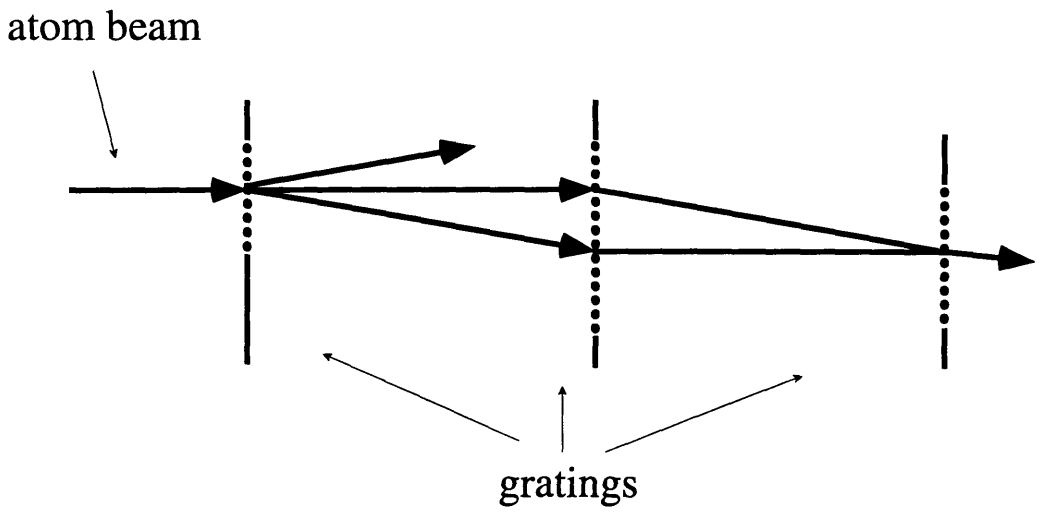

Fig 1.1: A schematic, not to scale, of our atom interferometer. The 0th and 1st order beams from the first grating strike the middle grating where they are diffracted to form an interference pattern in the plane of the third grating. The third grating acts as a mask for this pattern, and the detector, located beyond the third grating, records the total flux transmitted.

	Our interferometer	**Scaled (x 38,000)**
Wavelength	0.17Å (v = 1000 m/s)	6430Å (He-Ne laser)
Grating period	2000Å	7.6 mm
Grating separation	66 cm	25 km
Beam width at 2nd grating	40 μm	1.5 m
Beam separation at 2nd grating	55 μm	2.1 m

Table 1.1: Some parameters of the interferometer. The column at the right shows the corresponding parameters for a He-Ne interferometer with the same relative dimensions as our atom interferometer.

We fabricate the gratings using electron beam lithography techniques that we have developed in conjunction with Michael Rooks and others at the National Nanofabrication Facility at Cornell University [KSR91], [EKP92]. A electron microscope (TEM) picture of one such grating is shown in Fig. 1.2

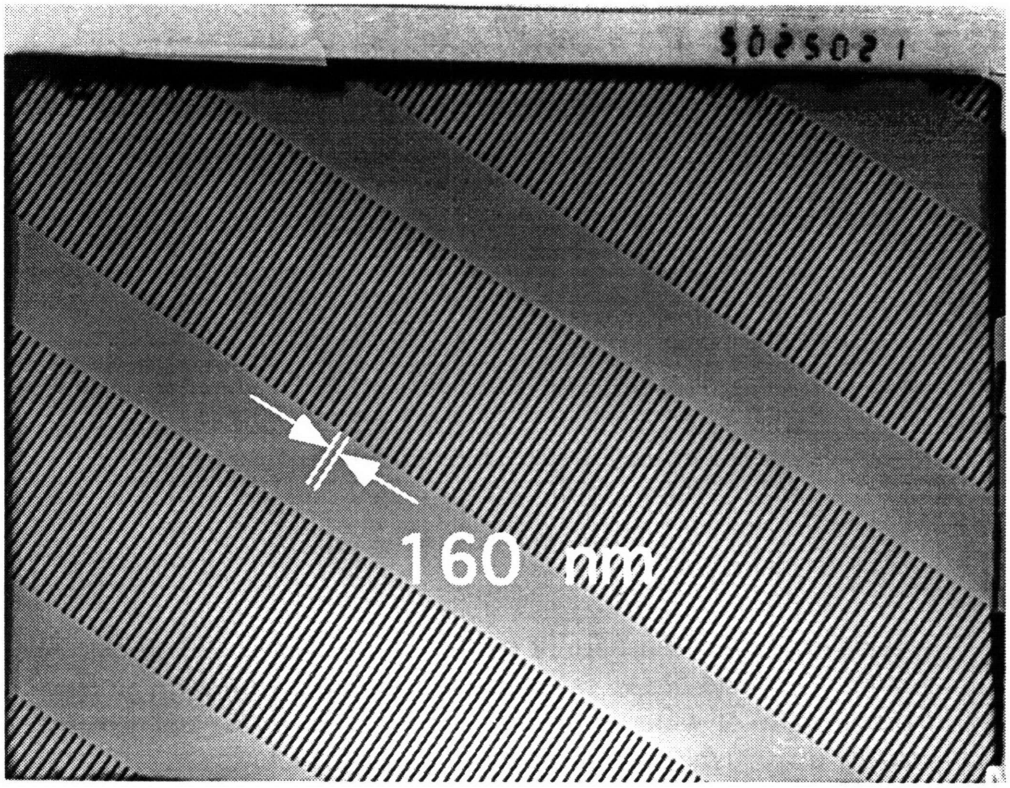

Fig 1.2: TEM image of a 160 nm period diffraction grating we fabricated (8000x magnified). It consists of an array of narrow slots etched in a thin ~200 nm membrane. The atoms pass through the slots (dark), but are blocked by the bars. The orthogonal bars form the support structure with a 5.0 μm period.

Atom diffraction from a single grating (first demonstrated here at MIT [KSS88]) is shown in Fig. 1.3—this pattern is a scan of the atomic beam intensity in the plane of the detector when only the 1st grating is in place. Of the many diffracted orders evident in

the graph, generally only the central (0th order) peak and one of the peaks to either side (±1st order) contribute to the interference signal measured in the interferometer.

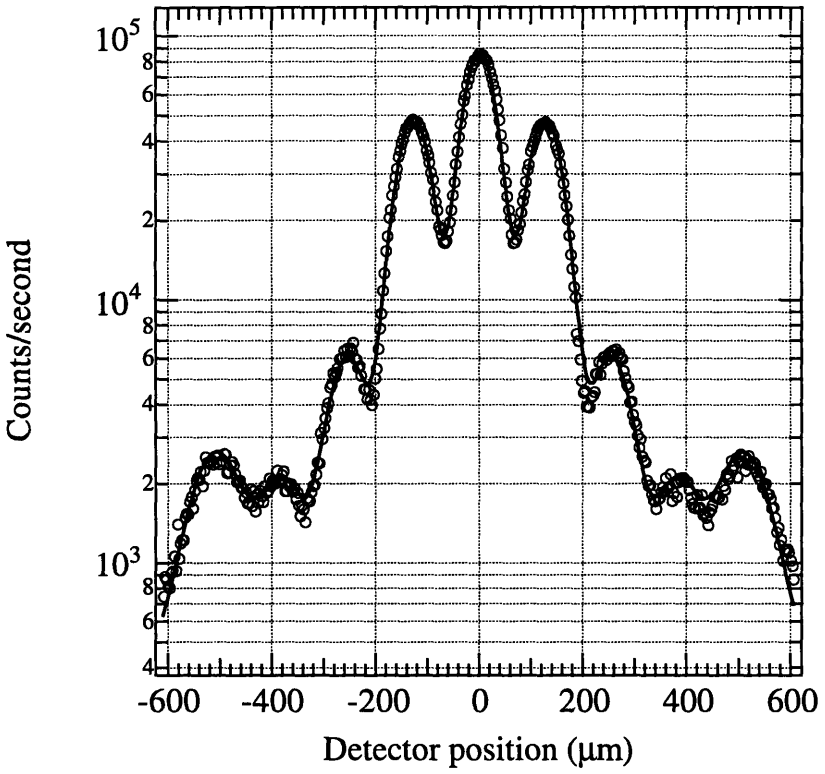

Fig 1.3: A typical diffraction pattern of sodium atoms from a 200 nm period grating. The solid line is calculated for a grating with average open fraction (ratio of width of opening to period) of 40 %, and a beam velocity of 1080 m/s corresponding to $\lambda_{dB} = 0.16$ Å.

When the 2nd and 3rd gratings are also moved into place, we record interference fringes of the type shown in Fig. 1.4. We have measured atomic fringe contrasts as high as 43% for our separated beam interferometer, which is more than 60% of the theoretical maximum. For experiments in which full separation of the atomic beams is not required, we can dramatically increase our interference signal by either removing the collimation

slits entirely, or changing our source expansion gas from argon to helium.* An example of the latter is shown in Fig. 1.5. Although the contrast in this case is somewhat lower, this is more than offset by the more than 10-fold increase in the average signal. In this configuration, we can determine the phase to within ~150 mrad with only 50 msec worth of data.

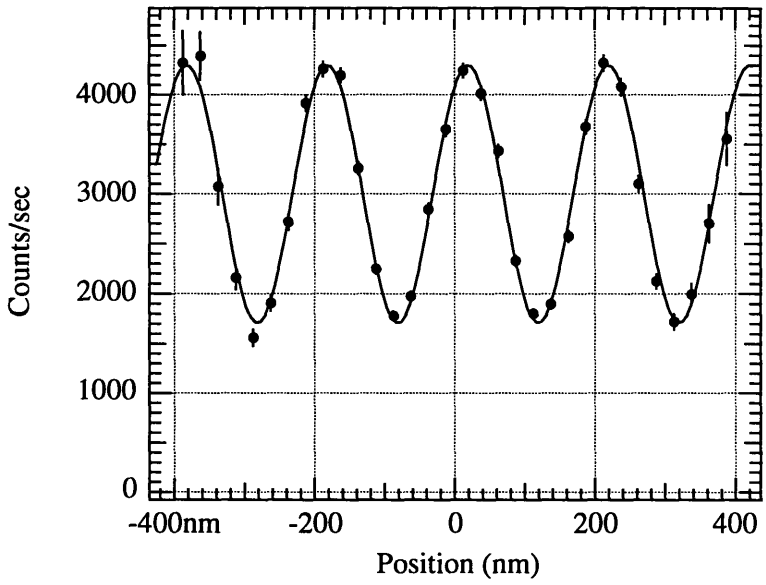

Fig 1.4: High contrast atomic interference pattern showing the detected atomic signal vs. grating position. The contrast (or fringe visibility) of this pattern is 43.1(6)%, and the phase uncertainty is 14 mrad. This data was taken in 20 s with an average count rate of 3000 counts/sec obtained by using argon as the source carrier gas.

* this increases the sodium beam velocity and thereby reduces the separation of the arms of the interferometer. This will be discussed in a later section.

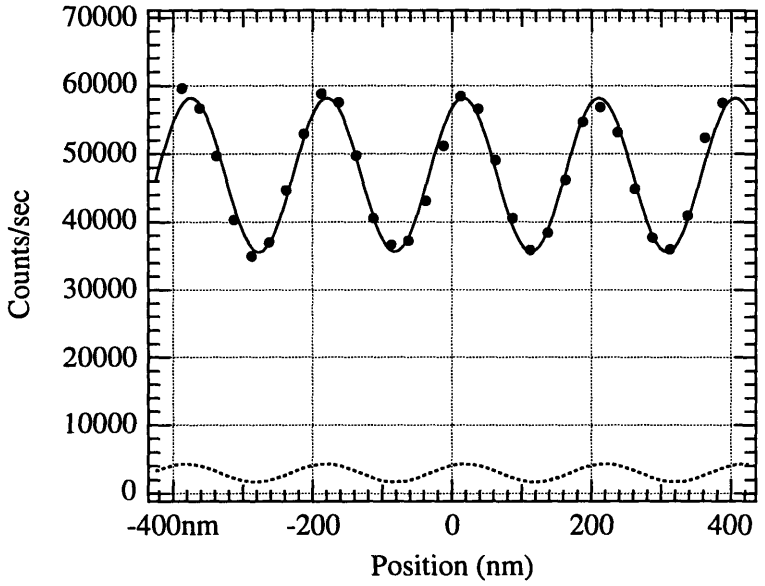

Fig 1.5: High contrast atomic interference pattern showing the detected atomic signal vs. grating position. The contrast (or fringe visibility) of this pattern is 24.2(2)%, and the phase uncertainty is 9 mrad. This data was taken in 10 s with an average count rate of 47000 counts/sec obtained by using helium as the source carrier gas. The dashed line is from the fit to the data in Fig. 1.4.

2. Loss of Coherence in an Atom Interferometer due to Scattering a Single Photon

This chapter will discuss the experiments we performed to measure the loss of atomic coherence due to entanglement with photons scattered from the atoms. This experiment demonstrated that the loss of coherence depends on the spatial separation of the interfering waves at the point of scattering compared with the wavelength of the scattering probe. Furthermore, we were able to demonstrate that the loss of coherence is not truly destroyed, but only entangled with the photons scattered into many final directions.

2.1. Introduction and Historical Background

The essence of this experiment is a very simple system shown in Fig. 2.2.1: single photons are scattered from atoms within a two-path atom interferometer at different locations corresponding to different spatial separations of the interfering atom waves.

If the scattered photons were collected with a microscope, they could be used to localize the atom with a maximum resolution limited to roughly half the wavelength of the photon. From the principle of complementarity, which forbids simultaneous observation of wave and particle behavior, we conclude that the atomic interference (a manifestly wave-like behavior) must be destroyed when the separation of the interfering paths exceeds the wavelength of the probe (i.e. when it is possible to identify which path

the atom traversed). Note that this is true whether or not one actually looks with the microscope—just being able to in principle is enough to destroy the interference pattern.

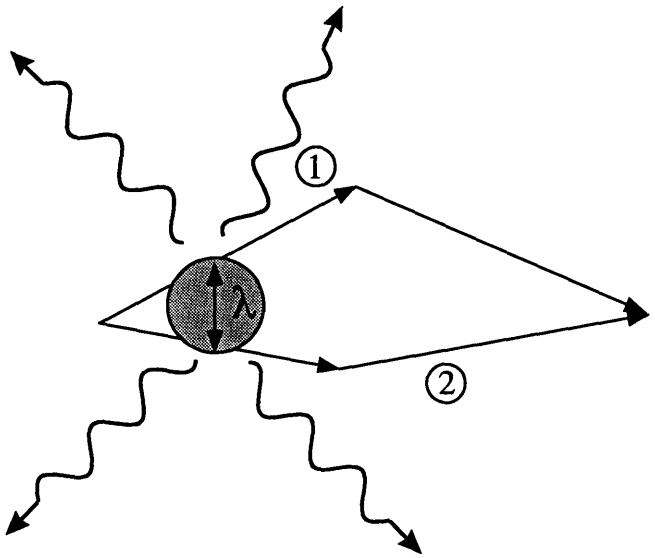

Fig. 2.2.1: Photons are scattered from a two-path atom interferometer. The photons can be collected with a microscope to measure which of the two paths the atom traversed, with a resolution limited by the wavelength of the photon, λ.

Of course, one cannot read very far into most introductory quantum mechanics textbooks before encountering a discussion along these lines. The specific two path interferometer usually discussed is the Young's two-slit experiment (for example [FRT78]). Indeed, according to Feynman, this experiment "has in it the heart of quantum mechanics. In reality it contains the only mystery" [FLS65]. Rightly so, for the interference of probability amplitudes is one of the most fundamental aspects of quantum theory. In the two-slit experiment, as in any two-path interferometer, the interference results from the superposition of two quantum mechanical amplitudes. When only one slit is open, the amplitude for passing through the closed slit is zero and the interference disappears. A more elaborate strategy to determine which path the particle traversed was

proposed by Einstein at the 1927 Solvay Congress [BOR49]. He suggested a *gedanken** experiment which he claimed permitted simultaneous observation of the wave and particle natures of a photon by measuring the recoil of the slit in Young's experiment. Bohr, in his famous reply, countered that the correct treatment of the problem required including the slit as part of the quantum mechanical system, and in so doing, showed that measuring the path of the particle implied, via Heisenberg's uncertainty principle, an uncertainty in its momentum sufficient to wash out the interference fringes.

Somewhat later, Feynman proposed a *gedanken* experiment now known as the "Feynman light microscope" in which scattered photons are used to measure "which-way" information in a two-slit experiment with electrons. In a sense, this *gedanken* experiment is a synthesis of the Einstein-Bohr *gedanken* experiment and the original Heisenberg microscope. In Feynman's analysis of his *gedanken* experiment, he showed in a very general way that the loss of visibility of the interference pattern is related to the degree to which one can determine the which-path information.

More detailed analysis of the relationship of the loss of interference and which-path information was first provided by Wooters and Zurek [WOZ79], and later by others [ZEI86], [SAI90]. Recently, Sleator et al. [SCP91] and Tan and Walls [TAW93] considered photon scattering from atoms in a two-slit experiment. While the two-slit gedanken experiment bears close resemblance to our study, there are important differences that we will highlight in the subsequent sections. With this preamble, I now include a copy of the paper we have submitted to Physical Review Letters describing our experiments.

---

* German for "thought" in the sense of hypothetical

2.2. Photon Scattering from Atoms in an Atom Interferometer: Coherence Lost and Regained (submitted for publication)

Michael S. Chapman[1], Troy D. Hammond[1], Alan Lenef[1], Jörg Schmiedmayer[1,2], Richard A. Rubenstein[1], Edward Smith[1], and David E. Pritchard[1]

[1] *Department of Physics and Research Laboratory of Electronics*
Massachusetts Institute of Technology, Cambridge, Massachusetts 02139, USA.

[2] *Institut für Experimentalphysik, Universität Innsbruck, A-6020 Innsbruck, Austria*

We have scattered single photons from interfering deBroglie waves in an atom interferometer and observed contrast loss and revivals that are directly related to the spatial separation of the deBroglie waves. Additionally, we have demonstrated that the fringe visibility can be recovered by detecting only atoms that are correlated with photons emitted into a limited angular range.

PACS number(s): 03.65.Bz, 03.75.Dg

Loss of coherence in one system A that results from entanglement or correlation with another system M has long been an important issue in quantum mechanics. It is of special interest both because of the difficulty of incorporating the resulting coherence loss into Schrödinger's equation describing system A and because of its relevance to understanding the measurement process in particular and the connection between quantum mechanics and classical mechanics in general [1]. A simple process resulting in entanglement is the elastic scattering of two particles, where the initial separable state evolves into an entangled state such that the total momentum and energy of the system is conserved for each possible outcome. Similar entangled states give rise to many fascinating quantum mechanical phenomena such as EPR pairs and multiparticle interferometry [2].

The details of the loss of coherence of one system entangled with another can be studied directly in interferometry experiments. This is often discussed in the context of "which-way" *gedanken* experiments where the visibility of the interference fringes of A is reduced by attempting to measure which path the particle traversed using system M [3-5]. In the Feynman light microscope *gedanken* experiment, scattered photons provide which-path information in a Young's *gedanken* two-slit experiment with electrons [4] or atoms [6,7]. Complementarity suggests that fringe contrast must disappear when the slit separation is greater than the wavelength of light, since, in principle, one could detect the scattered photons to determine through which slit the atom passed. Indeed, photon scattering has been used to completely destroy atomic interference fringes for interfering path separations much larger than the photon wavelength [8].

In the experiment reported here we studied the loss of atomic coherence due to photon scattering in a three-grating Mach-Zender atom interferometer [9] (see Fig. 1). By scattering single photons from the atoms within the interferometer at a variable

distance downstream of the first grating, we measured the gradual loss and revival of the atomic fringe visibility (contrast) as a function of the spatial separation d of the interfering paths of the interferometer at the point of scattering. We then demonstrated that the lost interference could be partially regained in a novel correlation experiment.

For our experimental configuration, the atom wavefunction at the third grating may be written $\psi(x) = u_1(x) + e^{i\phi_0} u_2(x) e^{ik_g x}$ where $u_{1,2}$ are (real) amplitudes of the upper and lower beams respectively, $k_g = 2\pi/\lambda_g$ where λ_g is the period of the gratings, and ϕ_0 is a relative phase we may take to be zero. To describe the effects of scattering within the interferometer, we first consider an atom within the interferometer elastically scattering a photon with well-defined incident and final (measured) momenta, $\vec{k}_i$ and $\vec{k}_f$ with $|\vec{k}_i| = |\vec{k}_f| = k$. With the scattering, the atomic wavefunction becomes

$$\psi'(x) \propto u_1(x - \Delta x) + e^{i\phi_0} u_2(x - \Delta x) e^{ik_g x + \Delta\phi} \tag{1}$$

The resulting atomic interference pattern shows no loss in contrast but acquires a phase shift [10,11]

$$\Delta\phi = \Delta\vec{k} \cdot \vec{d} = \Delta k_x d \tag{2}$$

where $\Delta\vec{k} = \vec{k}_f - \vec{k}_i$, and $\vec{d}$ is the relative displacement of the two arms of the interferometer at the point of scattering. Additionally, there is a spatial shift of the envelope of the atomic fringes due to the photon recoil given by $\Delta x = (2L - z)\Delta k_x / k_{atom}$, where $k_{atom} = 2\pi/\lambda_{dB}$, and $(2L - z)$ is the distance from the point of scattering to the third grating.

When the direction of the scattered photon is not observed, the atom interference pattern is given by an incoherent sum of the interference patterns with different phase shifts [12] corresponding to different final photon directions (i.e. a trace over the photon states),

$$C'\cos(k_g x+\phi')=\int d(\Delta k_x)P(\Delta k_x)C_0\cos\left(k_g x+\Delta k_x d\right) \tag{3}$$

where $P(\Delta k_x)$ is the probability distribution of transverse momentum transfer and C_0 is the original contrast or visibility of the atomic fringe pattern. For the case of scattering a single photon, $P(\Delta k_x)$ (shown in the inset to Fig. 2) is given by the radiation pattern of an oscillating dipole [13]. The average transverse momentum transfer is $\hbar\Delta\bar{k}_x=1\hbar k$ (the maximum of $2\hbar k$ occurs for backward scattering of the incoming photon and the minimum of $0\hbar k$ occurs for forward scattering). Due to the average over the angular distribution of the scattered photons, there will be a loss of contrast ($(C'\le C_0)$) and a phase shift ϕ' of the average atomic interference pattern. It follows from Eq. 3 that the measured contrast (phase) of the interference pattern as a function of the separation d of the atom waves will vary as the magnitude (argument) of the Fourier transform of $P(\Delta k_x)$. Eq. 3 is equivalent to the theoretical results obtained for the two-slit *gedanken* experiment [6,7] (in which case d is the slit separation), even though explicit which-path information is not necessarily available in our Mach-Zender interferometer in which the atom wavefunctions can have a lateral extent (determined by the collimating slits) much larger than their relative displacement, d.

In our experimental apparatus shown in Fig. 1, a beam of atomic sodium with a narrow rms velocity distribution (<4%) is produced by a seeded inert gas supersonic source. The beam is collimated by two slits separated by 85 cm. The atom interferometer uses three 200 nm period nanofabricated diffraction gratings separated by 65 cm. We record interference fringes of the form $\bar{N}\left(1+C\cos\left(k_g x+\phi\right)\right)$, where $\bar{N}$ is the average count rate, by measuring the atomic flux through the three gratings while varying the transverse positions of the gratings [9].

Single photons are scattered from the atoms within the interferometer by using a laser beam to resonantly excite the atoms, which then decay back to the ground state via

spontaneous emission. The atoms are excited from the $F = 2, m_F = 2$ ground state to the $F' = 3, m'_F = 3$ excited state using resonant $\sigma+$ polarized laser light ($\lambda_{photon} = 589$ nm). This ensures that the excitation and subsequent spontaneous emission occur within a closed two-state system. The atomic beam is prepared in the $F = 2, m_F = 2$ state by optical pumping with a $\sigma+$ polarized laser beam intersecting the atomic beam before the first collimating slit. We typically achieve ~95% optical pumping, which we determine (within a few percent) using a two-wire Stern-Gerlach magnet to measure state-dependent deflections of the atomic beam.

The excitation laser beam is focused to a ~15 μm waist (FWHM of the field) along the atom propogation direction. A cylindrical lens is used to defocus the beam in the y–direction to ensure uniform illumination over the full height of the atomic beam (~1 mm). The transit time through the waist is smaller than the lifetime of the excited state, hence the probability for resonant excitation in the two-state system shows weakly damped Rabi oscillations, which we observe by measuring the atomic deflection from the collimated atom beam as a function of laser power. To achieve one photon scattering event per atom, we adjust the laser power to the first maximum of these oscillations, closely approximating a π-pulse.

To study the effects of photon scattering on the atomic coherence as a function of the separation d, the excitation laser beam is translated incrementally along the atomic beam axis. The contrast and the phase of the interference pattern are determined at each point, both with and without the photon scattering.

In the first part of our experiment, we make no attempt to correlate the detected atoms with the direction of the scattered photon. The results of this study are shown in Fig. 2. First, we observe that, as expected, scattering the photons before and immediately after the first grating does not affect the contrast or the phase of the atomic interference

pattern. For small beam separations, where $\Delta\bar{k}_x d << \pi$, the phase of the fringes increases linearly with d with slope 2π determined by the average momentum transfer of $1\hbar k$. The contrast decreases sharply with increasing beam separation d and falls to zero for a separation of about half the photon wavelength, at which point $\Delta\bar{k}_x d \approx \pi$. This would occur exactly at $d = \lambda/2$ if the scattered photon angular distribution were isotropic. As d increases further, a periodic rephasing of the interference gives rise to partial revivals of the contrast and to a periodic phase modulation. The fit, based on Eq. 3, includes contributions from atoms that scattered 0 or 2 photons and is in good agreement with the data. The effects of velocity averaging are minimal for the narrow velocity distribution of our beam.

The phase shift $\Delta\phi$ resulting from the entanglement is, in our experiment, distinct from the "deflection" of the atom Δx due to the photon recoil. The difference is clear: the displacement of the envelope is ~100–200 fringes in our experiment, whereas $\Delta\phi$ is at most only a few fringes. Furthermore, as the point of scattering is moved further downstream, the displacement of the fringe envelope actually decreases slightly for a given $\vec{k}_f$, while the corresponding phase shift monotonically increases. Therefore, the measured loss of fringe visibility cannot be simply understood as resulting from the transverse deflections of the atom at the detection screen (in our case the third grating) due to the photon momentum transfer as it is for the two-slit *gedanken* experiments.

We point out that Δx (or equivalently the x–component of the photon momentum transfer) is precisely what is measured in determining the transverse momentum distribution of an atomic beam after scattering a photon. These distributions have been measured for diffraction of an atomic beam passing through a standing light wave undergoing a single [14] or many [15] spontaneous emissions and for a simple collimated beam excited by a travelling light wave [16].

We now describe a variant of our experiment in which the atoms observed are correlated with photons scattered in a narrow range of directions. Under these conditions, we have demonstrated that the coherence lost as d increases may be partially regained. In principle, this could be achieved by detecting the photons scattered in a specific direction in coincidence with the detected atoms. Such an approach is not feasible in our experiment for a number of technical reasons. However, we have performed a unique experimental realization of this type of correlation experiment made possible because the deflection of the atom Δx is a measurement of the final photon momentum projection, k_x and hence Δk_x.

By using very narrow beam collimation in conjunction with small detector acceptance, we selectively detect only those atoms correlated with photons scattered within a limited range of Δk_x, resulting in a narrower distribution $P'(\Delta k_x)$ in Eq. 3. This is achieved by using 10 μm slits and a 10 μm wide third grating, which can be translated to preferentially detect atoms that have received different momentum transfers. In contrast, for the first part of our experiment, we used 40 μm wide collimating slits and a 50 μm wide third grating to be sure that all momentum transfers were detected.

The experimental procedure for the correlation experiment begins by first taking data as in Fig. 2 with wide collimation slits and gratings to verify the experimental alignment and laser intensity. The experiment is then repeated with narrow slits in place, for three different positions of the narrow third grating (refered to as Cases I-III) corresponding to different momentum transfer distributions accepted by the detector, $P_i'(\Delta k_x)$, i = I, II, III.

The contrast is plotted as a function of d for Cases I and III where we preferentially detect atoms that scattered photons in the forward and backward direction, respectively. The contrast for Case II is similar to Case I and is not shown. The measured contrasts in

this figure are normalized to the $d = 0$ (laser on) values [17]. The contrast falls off much more slowly than previously—indeed we have regained over 60% of the lost contrast at $d \approx \lambda/2$.

The contrast falls off more rapidly for the faster beam velocity (Case III, $v_{beam} = 3200$ m / s) than the slower beam velocity (Cases I and II, $v_{beam} = 1400$ m / s) because the momentum selectivity is correspondingly lower. The final beam profile at the third grating is a convolution of the initial trapezoidal profile of the atomic beam [18] and the distribution of deflections $\Delta x \propto \Delta k_x$ [13]. The initial and final profiles are shown in the upper inset of Fig. 3 for $v_{beam} = 1400$ m / s. For a faster beam velocity, the different photon recoils are less separated in position at the detector, resulting in poorer selectivity.

The phase shift is plotted as a function of d for the three cases in the lower half of Fig. 3. The slope of Case III is nearly 4π indicating that the phase of the interference pattern is predominantly determined by the backward scattering events. Similarly, the slope of Case I asymptotes to zero due to the predominance of forward scattering events. Case II is an intermediate case in which the slope of the curve, ~3π, is determined by the mean accepted momentum transfer of $1.5\hbar k$. The lower inset shows the transverse momentum acceptance of the detector for each of the three cases (i.e. the functions $P_i'(\Delta k_x)$), which are determined using the known collimator geometry and beam velocity. The fits for the data in Fig. 3 are calculated using Eq. 3 and the modified distributions, $P_i'(\Delta k_x)$ and include effects of velocity averaging as well as atoms that scattered 0 or 2 photons.

In summary, we have directly measured the loss of atomic coherence in an atom interferometer caused by entanglement with single scattered photons. We have exploited the ability of our experiment to measure the photon's final momentum via the deflection

of the atom to select only those atoms that had scattered photons into a limited angular range, thereby partially regaining the lost coherence. This shows that the atomic coherence is not truly destroyed, but only entangled with photons scattered into different modes of the vacuum radiation field.

This work was supported by the Army Research Office contracts DAAL03-89-K-0082, and ASSERT 29970-PH-AAS, the Office of Naval Research contract N00014-89-J-1207, and the Joint Services Electronics Program contract DAAL03-89-C-0001. We thank Michael Rooks and other staff at the National Nanofabrication Facility at Cornell University for their help in grating fabrication. J.S. acknowledges support from the Austrian Academy of Sciences.

References

1. J.A. Wheeler and W.H. Zurek. *Quantum Theory and Measurement* (Princeton University Press, Princeton, 1983).

2. For an overview, see D.M. Greenberger, M.A. Horne and A. Zeilinger, Physics Today, 22 (1993), and references therein.

3. N. Bohr in *A. Einstein: Philosopher - Scientist* edited by P. A. Schilpp p. 200-241 (Library of Living Philosophers, Evaston, 1949); a detailed analysis is given in: W. Wooters and W. Zurek, Phys. Rev. D **19** 473 (1979).

4. R. Feynman, R. Leighton and M. Sands. *The Feynman Lectures on Physics* (Addison-Wesley, Reading, MA, 1965)vol. 3, p. 5-7

5. A. Zeilinger. in *New Techniques an Ideas in Quantum Mechanics* , p. 164, edited by (New York Acad. Science, New York, 1986).

6. T. Sleator, O. Carnal, T. Pfau, A. Faulstich, H. Takuma and J. Mlynek. in *Laser Spectroscopy X* , p. 264, edited by M. Dulcoy, E. Giacobino and G. Camy (World Scientific, Singapore, 1991).

7. S.M. Tan and D.F. Walls, Phys. Rev. A **47**, 4663 (1993)

8. F. Riehle, A. Witte, T. Kisters and J. Helmcke, Appl. Phys. B **54**, 333 (1992). U. Sterr, K. Sengstock, J.H. Muller, D. Bettermann and W. Ertmer, Appl. Phys. B **54**, 341 (1992). J.F. Clauser and S. Li, Phys. Rev. A **50**, 2430 (1994). M.S. Chapman, C.R. Ekstrom, T.D. Hammond, R.A. Rubenstein, J. Schmiedmayer, S. Wehinger and D.E. Pritchard, in press.

9. D.W. Keith, C.R. Ekstrom, Q.A. Turchette and D.E. Pritchard, Phys. Rev. Lett. **66**, 2693 (1991). J. Schmiedmayer, M.S. Chapman, C.R. Ekstrom, T.D. Hammond, S. Wehinger and D.E. Pritchard, Phys. Rev. Lett. **74**, 1043 (1995).

10. C. Bordé, Phys. Lett. A **140**, 10 (1989)

11. P. Storey and C. Cohen-Tannoudji, J. Phys. II France **4**, 1999 (1994)

12. A. Stern, Y. Aharonov and Y. Imry, Phys. Rev. A **41**, 3436 (1990)

13. L. Mandel, J. Optics (Paris) **10**, 51 (1979)

14. T. Pfau, S. Spalter, C. Kurstsiefer, C.R. Ekstrom and J. Mlynek, Phys. Rev. Lett. **29**, 1223 (1994)

15. P.L. Gould, P.J. Martin, G.A. Ruff, R.E. Stoner, J.L. Picque and D.E. Pritchard, Phys. Rev. A **43**, 585 (1991)

16. B.G. Oldaker, P.J. Martin, P.L. Gould, M. Xiao and D.E. Pritchard, Phys. Rev. Lett **65**, 1555 (1990)

17. Because of the narrow acceptance of the detector for this correlation experiment, $C(\text{laser off}) \neq C(\text{laser on})$ even when $d = 0$.

18. N.F. Ramsey. *Molecular Beams* (Oxford University Press, Oxford, 1985)

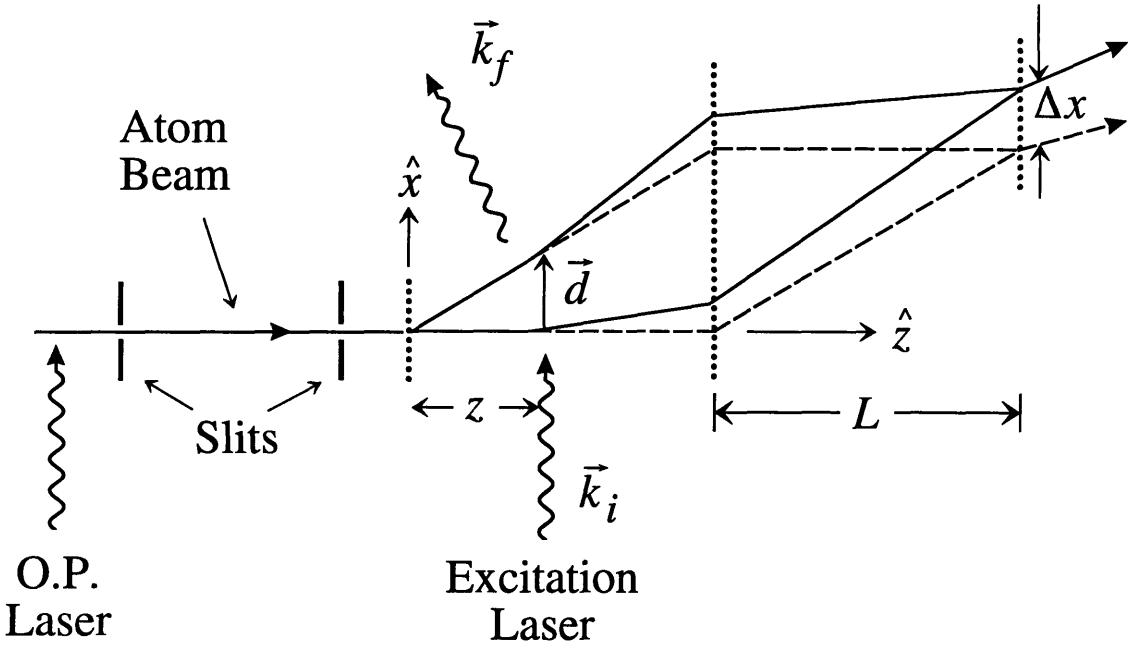

Figure 1: A schematic, not to scale, of our atom interferometer. The original classical trajectories of the atoms (dashed lines) are altered (solid lines) due to scattering a photon (wavy lines). The atom diffraction gratings are indicated by the vertical dotted lines.

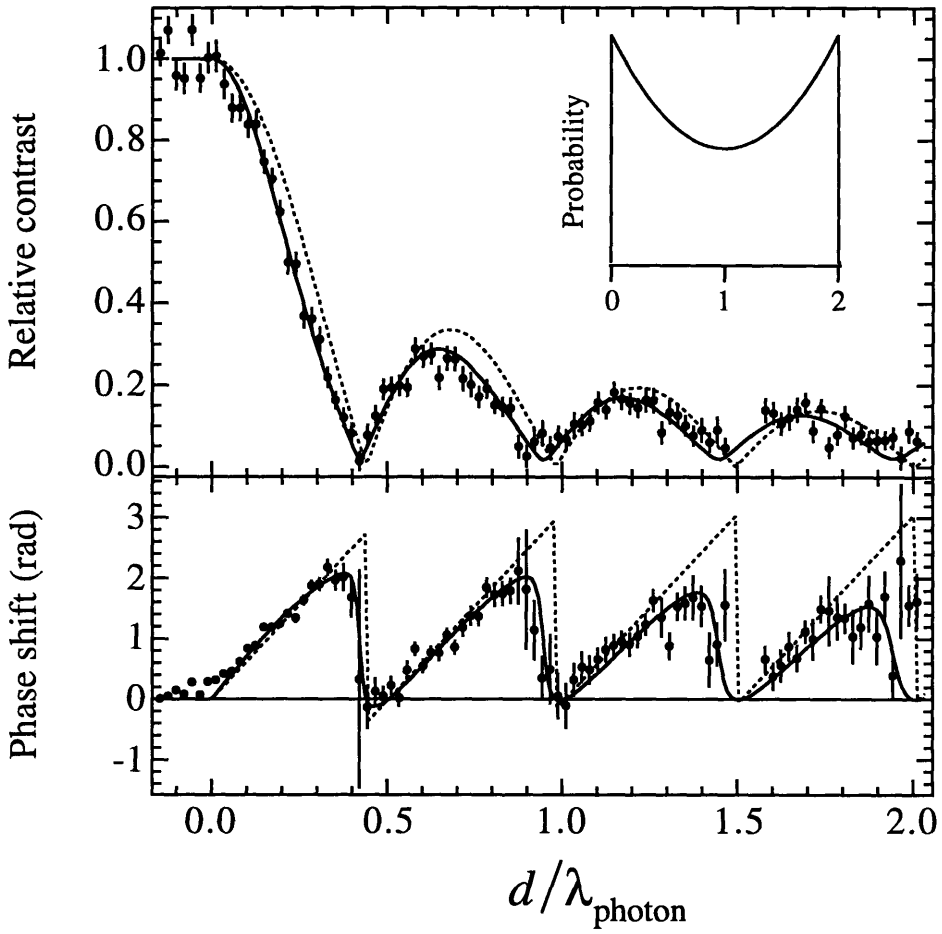

Figure 2: Relative contrast C(laser on)/C(laser off) and phase shift of the interferometer as a function of d, where $d = z\lambda_{dB}/\lambda_g$ and $d < 0$ indicates scattering before the first grating. For these data, the beam velocity was 3200 m/s ($d = \lambda_{photon}$ at z = 11 mm), there was 20 s of data per point, $\overline{N}$ = 31 kcps and C(laser off) = 11%. The dashed curve corresponds to purely single photon scattering, and the solid curve is a best fit that includes contributions from atoms that scattered 0 photons (5%) and 2 photons (18%). The inset shows $P(\Delta k_x)$, the distribution of the net transverse momentum transfer.

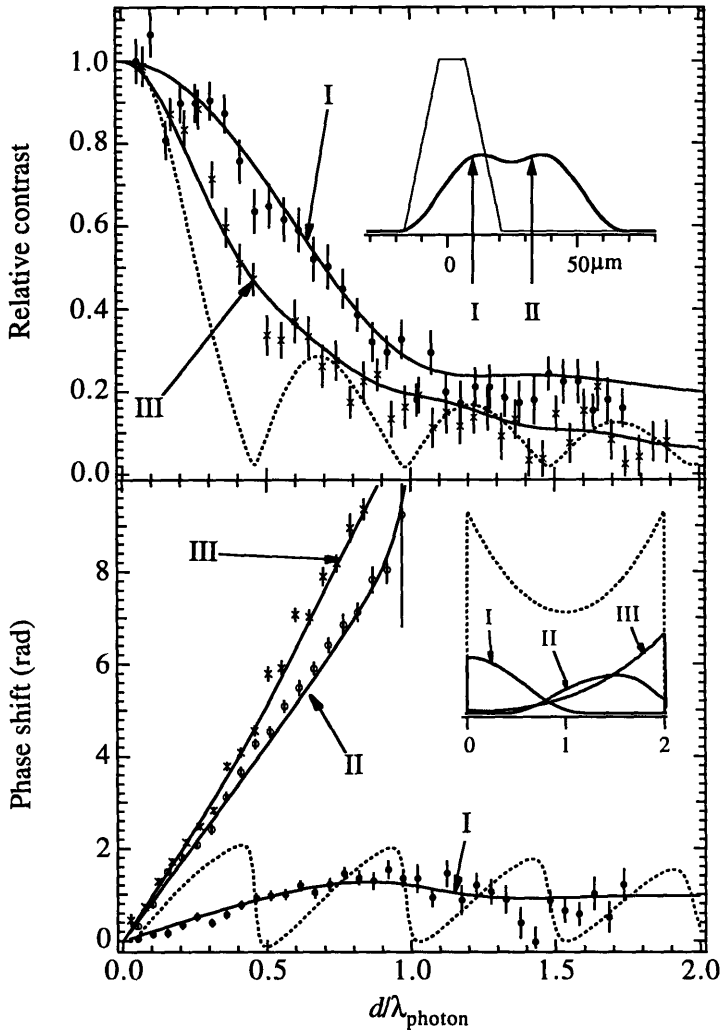

Figure 3: Relative contrast and phase shift of the interferometer as a function of d for the cases in which atoms are correlated with photons scattered into a limited range of directions. The solid curves are calculated using the known collimator geometry, beam velocity, and momentum recoil distribution and are compared with the uncorrelated case (dashed curves). The upper inset shows atomic beam profiles at the third grating when the laser is off (thin line) and when the laser is on (thick line) for $v_{beam} = 1400$ m / s. The arrows indicate the third grating positions for Cases I and II. The lower inset shows the acceptance of the detector for each case, $P_i'(\Delta k_x)$, compared to the original distribution (dotted line). The curves are calculated using the known collimator geometry, beam velocity, and momentum recoil distribution. For Cases I and II, $\overline{N}$ = 0.8 kcps and $C_0(d = 0)$ = 15%. For Case III, $\overline{N}$ = 2 kcps and $C_0(d = 0)$ = 24%.

2.3. Theory

The goal of this section is to give some of the theoretical details relevant to our experiment— in particular, how the contrast and phase of the atomic interference is affected due to scattering a single photon, and how these effects are modified under different experimental conditions.

2.3.1. Loss of coherence due to entanglement with scattered photons

Scattering a photon with a well-defined initial and final direction

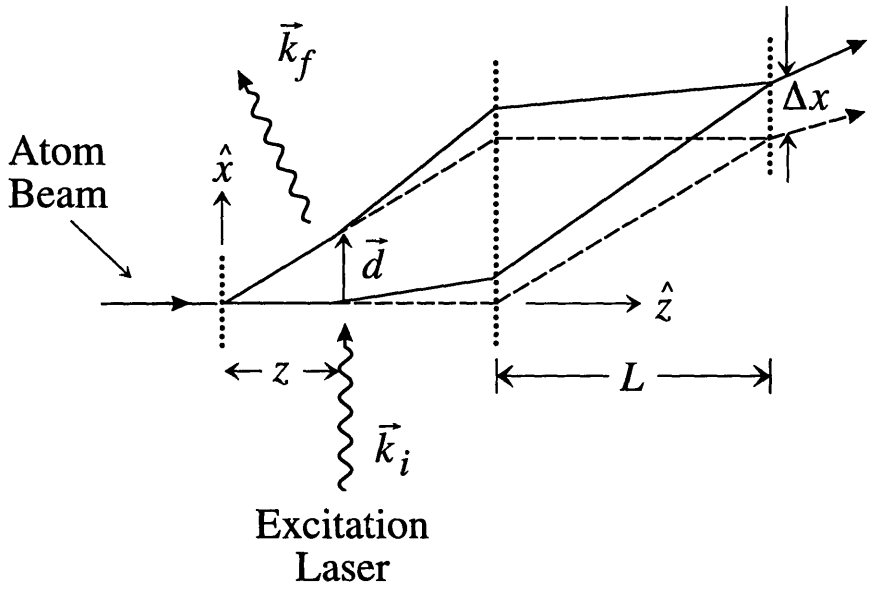

Fig. 2.3.1: A schematic, not to scale, of our atom interferometer. The original classical trajectories of the atoms (dashed lines) are altered (solid lines) due to scattering a photon (wavy lines). The atom diffraction gratings are indicated by the vertical dotted lines.

The atom interferometer we will consider in this section is a three grating Mach-Zender design schematically shown in Fig. 2.3.1. The atomic beam is coherently split by the first grating and then recombined by the second grating to form a spatial interference pattern in the plane of the third grating. We may write the wavefunction for this interferometer quite generally at the plane of the third grating as

$$\psi(x) \propto u_1(x) + e^{i\phi_0} u_2(x) e^{ik_g x} \tag{2.1}$$

where $u_{1,2}$ are the amplitudes of the upper and lower beams respectively, $k_g = 2\pi/\lambda_g$ where λ_g is the period of the gratings, and ϕ_0 is the phase difference between the two beams. Including the additional phase factor ϕ_0, allows us to specify $u_{1,2}$ as real functions with no loss in generality. In this case, the probability density for recording an atom at a location x is

$$I(x) = |\psi(x)|^2 = u_1^2 + u_2^2 + 2u_1 u_2 \cos(k_g x + \phi_0) \tag{2.2}$$

which may be written

$$I(x) = I_0(x)\left[1 + C_0 \cos(k_g x + \phi_0)\right] \tag{2.3}$$

where C_0 is the contrast of the interference pattern and $I_0(x)$ is the envelope function of the fringes which is slowly varying with respect to λ_g.

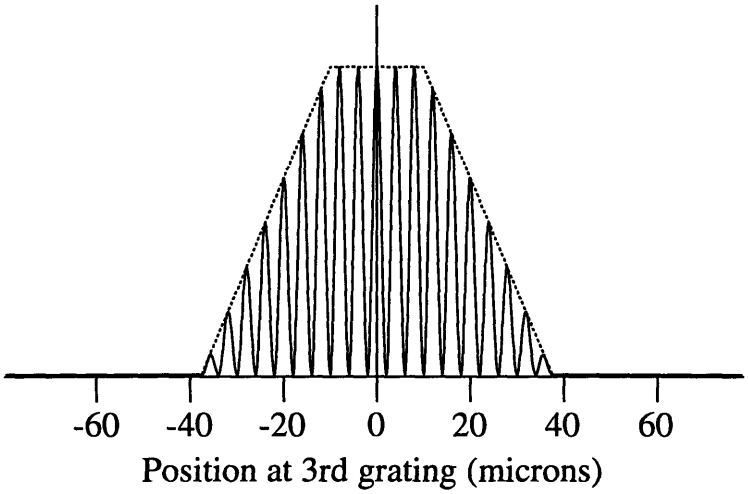

Fig 2.3.2: The probability density for detecting an atom at the plane of the 3rd grating, $I_0(x)$. The envelope function is a trapezoid determined by the collimation slits—this envelope is for 20 μm slits in our apparatus. The fringe pattern is for C_0 = 100% and $\phi_0 = 0$. *Note:* the fringes shown in this figure have a period of 4 μm, which is 20x larger period than the actual period (200 nm) of the fringes in our experiment.

We now wish to consider the scattering of a photon from the atoms within the interferometer. Specifically, let us consider the elastic scattering of a photon with a well-defined incident and final momentum $\vec{k}_i$ and $\vec{k}_f$, ignoring recoil so that $\left|\vec{k}_i\right| = \left|\vec{k}_f\right| = k$. In this case, the atom wavefunction becomes

$$\psi'(x) \propto u_1(x-\Delta x) + e^{i\phi_0} u_2(x-\Delta x) e^{ik_g x + \Delta\phi} \tag{2.4}$$

which results in an atomic interference pattern

$$I(x) = I_0(x-\Delta x)\left[1 + C_0 \cos(k_g x + \phi_0 + \Delta\phi)\right] \tag{2.5}$$

The key results are: (1) the interference pattern has the same contrast as before, (2) the pattern has acquired a phase shift $\Delta\phi$ and (3) the envelope of the fringes has shifted by an amount Δx. The phase shift of the atomic fringes is given by

$$\Delta\phi = \Delta\vec{k} \cdot \vec{d} = \Delta k_x d \tag{2.6}$$

where $\Delta\vec{k} = \vec{k}_f - \vec{k}_i$ is the net momentum transfer to the atom and $\vec{d}$ is the relative displacement of the two arms of the interferometer at the point of scattering. This phase shift arises from the atom-photon interaction [BOR89], [STC94] and will be discussed below.

The shift of the centroid of the envelope, Δx, is just the classical deflection of the atom due to the photon recoil and is given by

$$\Delta x = \Delta v_x t' = (2L - z)\Delta k_x / k_{atom} \tag{2.7}$$

where $\Delta v_x = \hbar \Delta k_x / m_{atom}$ is the x-component of the recoil velocity, $t' = (2L - z)/v_z$ is the transit time to the third grating, and we have used the deBroglie wave relation $k_{atom} = 2\pi/\lambda_{dB} = mv_z/\hbar$ for the longitudinal velocity of the atom.

The expression in Eq. 2.5 is a central result of this chapter. It states that the effect of scattering a single photon from each atom passing through the interferometer does not destroy the interference, *if the initial and final momenta of the photon are well-determined (i.e. prepared and measured, respectively).*

The results expressed in Eq 2.4 may be understood by writing the atom-photon wavefunction at the point of scattering.* The initial state of the atom can be written in either the position or momentum representation

$$|\varphi\rangle = \int d\vec{K}\tilde{\varphi}(\vec{K})\left|\vec{K}\right\rangle = \int d\vec{r}\,\varphi(\vec{r})|\vec{r}\rangle \tag{2.8}$$

Choosing the momentum representation for the moment, we can write the initial atom + photon wavefunction $|\psi_{in}\rangle = |\varphi\rangle \otimes \left|\vec{k}_i\right\rangle$ as

---

* this treatment closely follows that given in [CBA91]

$$|\psi_{in}\rangle = \int d\vec{K}\tilde{\varphi}(\vec{K})\left|\vec{K}\right\rangle \otimes \left|\vec{k}_i\right\rangle \tag{2.9}$$

After the scattering, the wavefunction becomes

$$\begin{aligned} \left|\psi_{fin}\right\rangle &= \int d\vec{K}\tilde{\varphi}(\vec{K})\left|\vec{K}+\vec{k}_i-\vec{k}_f\right\rangle \otimes \left|\vec{k}_f\right\rangle \\ &= e^{i(\vec{k}_i-\vec{k}_f)\cdot\vec{R}}\int d\vec{K}\tilde{\varphi}(\vec{K})\left|\vec{K}\right\rangle \otimes \left|\vec{k}_f\right\rangle \\ &= e^{i(\vec{k}_i-\vec{k}_f)\cdot\vec{R}}\left|\varphi\right\rangle \otimes \left|\vec{k}_f\right\rangle \end{aligned} \tag{2.10}$$

where we have used $\left|\vec{K}+\vec{k}_i-\vec{k}_f)\right\rangle = e^{i(\vec{k}_i-\vec{k}_f)\cdot\vec{R}}\left|\vec{K}\right\rangle$ where $\vec{R}$ is the position operator. We can now use the position representation to write

$$\left|\psi_{fin}\right\rangle = \int d\vec{r}e^{i(\vec{k}_i-\vec{k}_f)\cdot\vec{r}}\varphi(\vec{r})|\vec{r}\rangle \otimes \left|\vec{k}_f\right\rangle \tag{2.11}$$

from which we can see that the atom-photon scattering has the effect of applying a linearly varying phase to the spatial wavefunction. This, of course, is analogous to the effects on the atomic wavefunction when a transverse magnetic field linear gradient is applied to the interferometer for a short distance along the atom trajectory. In this case, the field gradient will exert a force on the atoms $\vec{F} = \nabla(\vec{\mu}\cdot\vec{B})$ which will change the transverse momentum of the atoms by $\Delta k_x \propto \mu_x(\partial B_x/\partial x)\delta\tau$ where $\delta\tau$ is the transit time of the atom through the gradient field. The atomic trajectories will be deflected proportional to the momentum kick and the transit time to the detector as before (see Eq. 2.7). The atomic fringes will be phase shifted proportional to the separation of the arms of the interferometer $\Delta\phi = \Delta k_x d \propto \left[\mu_x(\partial B_x/\partial x)\delta\tau\right]d$. Hence, just as for the case of photon scattering, the phase shift is zero when the gradient field is applied before or at the 1st grating, and it increases as the field is applied further downstream from the grating and the beam separation increases. In contrast, the deflection of the atomic trajectories are independent of the beam separation, and only depend on the transit time to the detector.

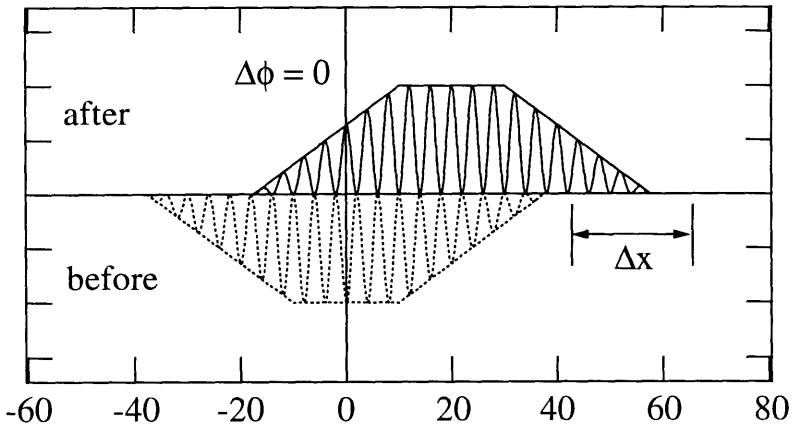

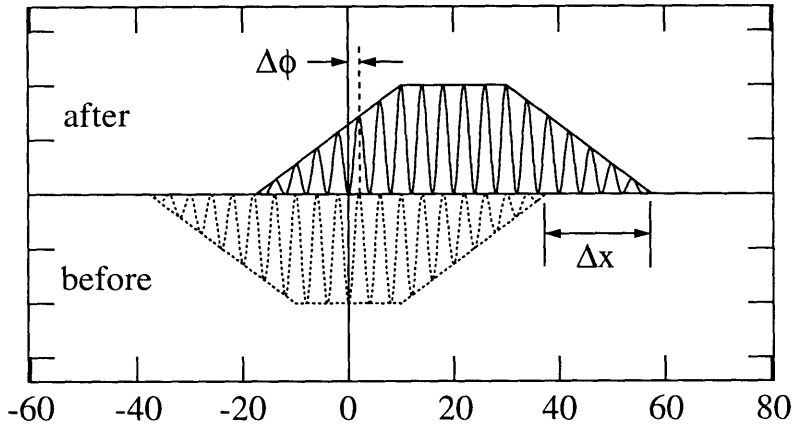

Fig. 2.3.3: These figures illustrate the distinction between Δx and $\Delta\phi$. In both figures, the deflected atomic fringes (solid) are shown opposite the undeflected (dashed). Both cases correspond to the same Δk_x and hence the same Δx, however, in the top graph $d = 0$ so $\Delta\phi = 0$ whereas in the bottom graph d is such that $\Delta\phi = \Delta k_x d = \pi$.

When the direction of the scattered photon is not measured

The remaining question to be answered is what is the resulting atomic interference pattern when the final photon is not observed. For simplicity, we will assume that the

initial photon momentum (and direction), $\vec{k}_i$, is still well-defined and oriented along the x-axis for example. The final photon angular direction is not measured, and hence we can only determine a given probability $P(\vec{k}_f)$ that it scattered along any particular direction (we restrict the discussion to elastic scattering). The atomic interference term will then be given by an *incoherent* sum of interference patterns with different phase shifts weighted by the probabilities $P(\vec{k}_f)$ [SAI90].

$$C\cos(k_g x+\phi')=\int d\vec{k}_f P(\vec{k}_f)C_0\cos\left(k_g x+\Delta\vec{k}\cdot\vec{d}\right)\delta\left(|\vec{k}_f|-k\right) \tag{2.12}$$

where the delta function restricts the integration to elastic scattering (i.e. the integration is just over the final direction of $\vec{k}_f$). We will find it useful to rewrite Eq. 2.12 in terms of Δk_x as

$$C\cos(k_g x+\phi')=\int d(\Delta k_x)P(\Delta k_x)C_0\cos\left(k_g x+\Delta k_x d\right) \tag{2.13}$$

Due to the average over the different final directions of the scattered photon, the atomic interference pattern will in general have reduced contrast $(C\le C_0)$ and a phase shift ϕ'. But importantly, the averaging is parameterized by d as well as $P(\Delta k_x)$, so that the effects of scattering will be minimal for $\Delta k_x d << \pi$ quite independently of $P(\Delta k_x)$, and the effects will become more pronounced for larger d. We can express the phase shift and contrast of the final fringe pattern in terms of Fourier transforms by using the identity $\cos(\alpha+\beta)=\cos\alpha\cos\beta-\sin\alpha\sin\beta$ as follows:

$$C'\cos(k_g x+\phi')=A(d)\cos\left(k_g x\right)-B(d)\sin\left(k_g x\right) \tag{2.14}$$

where we have defined the relative contrast $C'=C/C_0$. $A(d)$ and $B(d)$ are the Fourier cosine and sine transforms of $P(\Delta k_x)$ respectively,

$$A(d)=\int d(\Delta k_x)P(\Delta k_x)\cos(\Delta k_x d) \tag{2.15}$$

$$B(d)=\int d(\Delta k_x)P(\Delta k_x)\sin(\Delta k_x d) \tag{2.16}$$

Considering Eq. 2.14 for $x = 0$ and $k_g x = \pi/2$, we find the following expressions for the relative loss in contrast and the phase shift:

$$C' = \sqrt{A^2(d) + B^2(d)} \tag{2.17}$$

$$\tan(\phi') = B(d)/A(d) \tag{2.18}$$

or, since the complex Fourier transform is $F(d) = A(d) + iB(d) = |F|e^{i\phi'}$, we can say that the relative contrast (phase) of the fringes is given by the magnitude (argument) of the Fourier transform of $P(\Delta k_x)$.

The case of isotropic emission

Before we go on to consider exact forms of the distributions $P(\Delta k_x)$, let us first consider a simple example: isotropic scattering of single photons with wavelength λ_{photon}. If we ignore $\vec{k}_i$ (which we can if we excite the atom with a laser beam oriented perpendicular to the plane of the interferometer), then $\Delta k_x = k_{f,x}$ and $P(\Delta k_x)$ is a uniform constant over the interval $-k \leq \Delta k_x \leq k$, whose Fourier cosine transform is

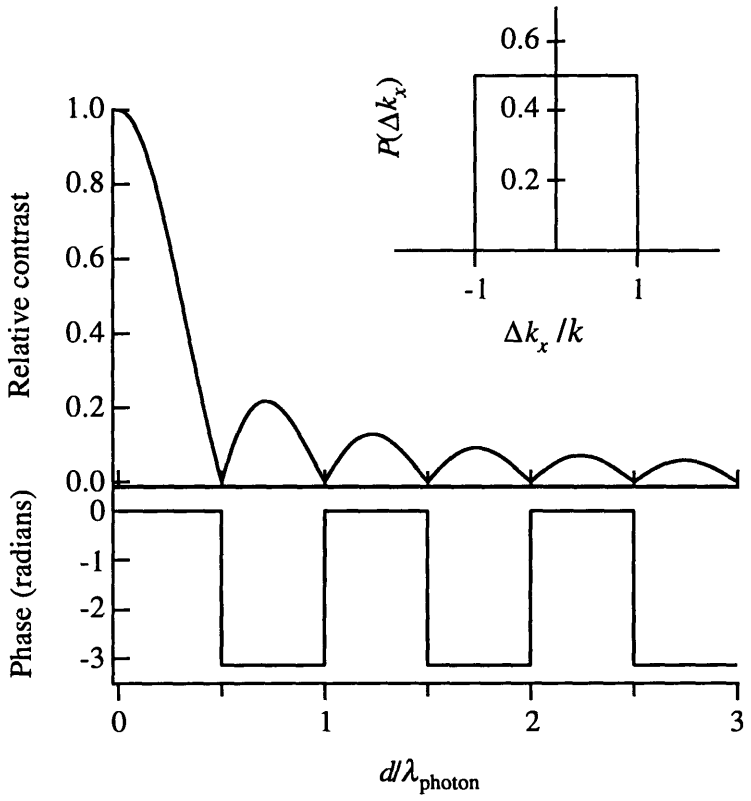

Fig 2.3.4: The relative contrast and phase shift of the atomic interference fringes for isotropic emission of a photon plotted versus the separation of the arms of the interferometer at the point of emission. The inset shows the uniform distribution of Δk_x over the interval $-k \leq \Delta k_x \leq k$ characteristic of isotropic emission of a photon.

$A(d)=\sin(kd)/kd$. Note that $B(d)=0$ because $P(\Delta k_x)$ is an even function. The contrast and phase of the interference pattern are shown in Fig 2.3.4. The contrast falls off rapidly and disappears completely at $d=\lambda_{photon}/2$ where $kd=\pi$. As d continues to increase, there is a revival in contrast, and the revived fringes are 180° out of phase with the original pattern. This cycle repeats with the phase shifting 180° each time relative to the previous revival.

The case of dipole emission

Although the result shown if Fig 2.3.4 is illustrative of the general problem, elastically scattered light from an atom is not generally isotropic. For a two-level atom, the angular probability distribution is given by the dipole emission pattern. For linear polarization corresponding to emission with $\Delta m=0$, the angular distribution is $P(\theta)=(3/8\pi)\sin^2\theta$, while for circular polarization with $\Delta m=\pm 1$ we have $P(\theta)=(3/16\pi)(1+\cos^2\theta)$.* These distributions are shown in Fig. 2.3.5. Also shown in this figure is $P(k_x)$, for the case in which the symmetry axis of the emission is aligned along the x axis (i.e. θ is the angle from the x-axis) which are obtained by integrating over y and z. For both linear polarization and circular polarization, the projections are the same [MAN79]

$$P(k_x)=\frac{3}{8k}\left(1+\frac{k_x{}^2}{k^2}\right) \quad \text{for} \quad -k\le k_x\le k$$
$$=0 \quad \text{otherwise} \tag{2.19}$$

---

* note, for linear polarization, θ is defined with respect to the polarization axis, while for circular polarization, it is defined with respect to the propagation axis $\hat{k}_i$ (see for example [WEI78], [MAN79])

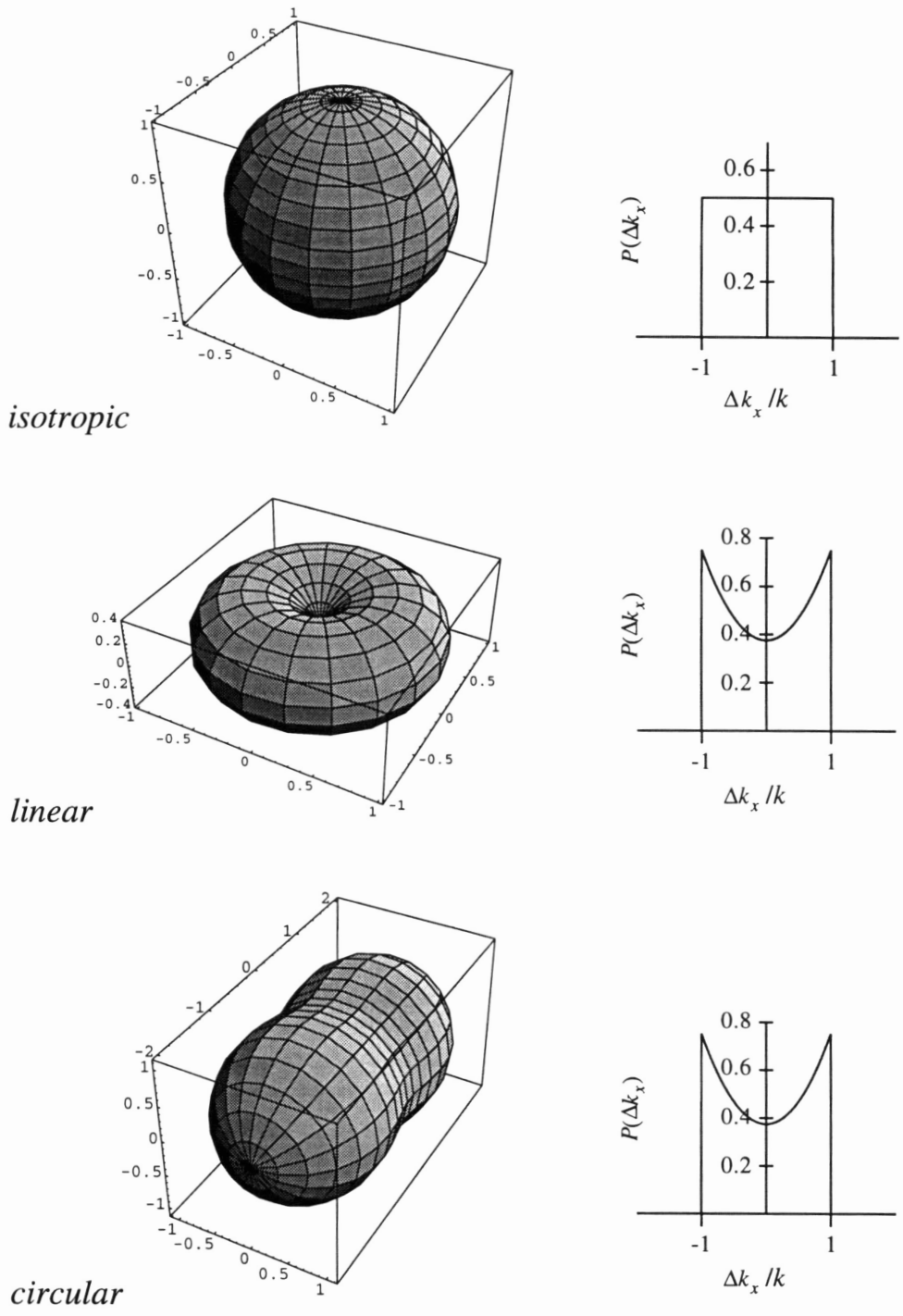

Fig. 2.3.5 Left graphs: Angular distribution of scattered radiation for isotropic emission, and dipole emission for linear and circular polarization. Right graphs: The corresponding distributions for the projection onto the x-axis (the axis of symmetry for the lower left distribution).

Henceforth, we will restrict our discussion to the case of circular polarization aligned along the x-axis. The total distribution $P(\Delta k_x)$ includes the contribution from the initial excitation photon (i.e. $\Delta k_x = k_{f,x} - k_{i,x}$). For the case when the initial photon propagates in the x-direction, the final distribution will be offset by k,

$$P(\Delta k_x) = \frac{3}{8k}\left[1+\left(1-\frac{\Delta k_x}{k}\right)^2\right] \quad \text{for} \quad -k \le \Delta k_x \le k \qquad (2.20)$$
$$= 0 \quad \text{otherwise.}$$

The Fourier cosine and sine transforms of this function are readily calculated to be

$$A(d) = \frac{3}{4(kd)^3}\left[kd + kd\cos(2kd) - \sin(2kd) + (kd)^2\sin(2kd)\right] \qquad (2.21)$$

$$B(d) = \frac{3}{2(kd)^3}\sin(kd)\left[kd\cos(kd) - \sin(kd) + (kd)^2\sin(kd)\right], \qquad (2.22)$$

and the contrast will vary with the separation d as,*

$$C'(d) = \frac{3}{2}\left|\frac{\cos kd}{kd^2} + \frac{\sin kd}{kd} - \frac{\sin kd}{kd^3}\right|. \qquad (2.23)$$

This function is shown in Fig. 2.3.6 along with the corresponding phase shift. The loss in contrast is qualitatively similar to the case of isotropic emission but with sharper and slightly shifted structure. The phase shift is markedly different. This is because the initial excitation is aligned along the x-axis, and hence the distribution is no longer symmetric. The reason the phase grows linearly with d with a slope of 2π may be understood by considering scattering when $d << \lambda$. In this case, we are averaging over a distribution of phase shifts (see Fig. 2.3.7) much smaller than π, and the resulting phase shift will be determined by the average of the distribution of phase shifts (i.e. $2\pi d/\lambda$)

---

* to minimize the algebra, we can determine this from the simpler case of the symmetric distribution in Eq. 2.15 [TAW93].

At the point which the contrast falls to zero, the phase undergoes a discontinuous jump of $-\pi$, just as in the isotropic case.

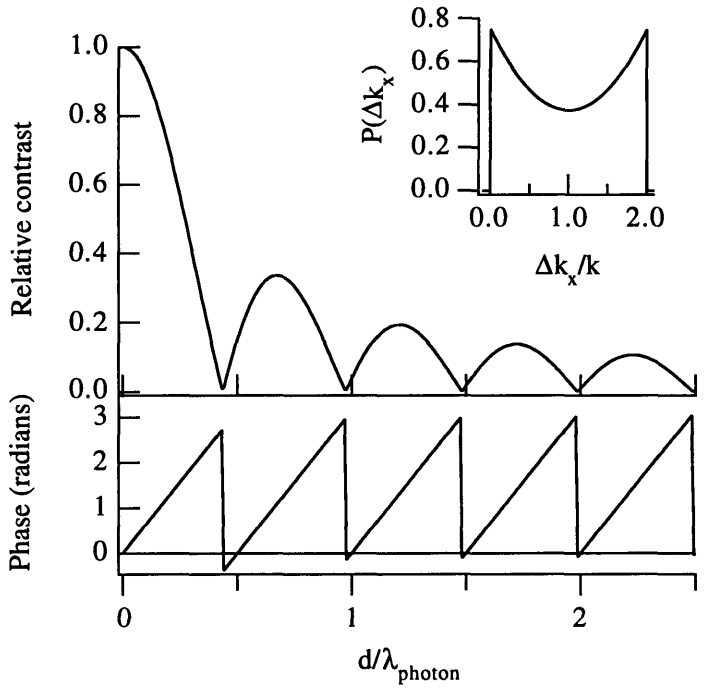

Fig. 2.3.6: The relative contrast and phase shift of the atomic interference pattern for single photon scattering for the case of circular polarization along the x-axis.

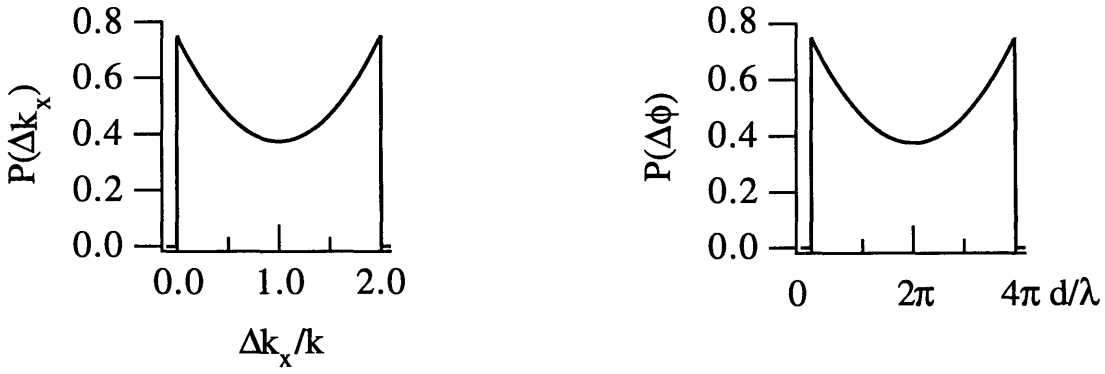

Fig 2.3.7: The distribution $P(\Delta k_x)$ is plotted on the left. On the right, this distribution is redisplayed in terms of the distribution of phase shifts $P(\Delta\phi)$, $\Delta\phi = \Delta k_x d$ over which we average to determine the final interference pattern.

Distribution of atomic velocities

The proceeding analysis was based on a monochromatic atomic beam in that we implicitly assumed that scattering at a given distance z from the 1st grating corresponded to a particular separation $d = \theta_{diff} z = \left(h/mv\lambda_g\right)z$. For an atomic beam with a finite velocity distribution, we must average over $d(v)$ to calculate the expected loss in contrast and phase shift. We use a supersonic beam in our experiment which features a very narrow velocity distribution, typically $\Delta v/v \leq 4\%$ rms. To calculate the effects of this distribution, we integrate the functions $A(d)$ and $B(d)$ over the gaussian velocity distribution (i.e. over the distributions of $d(v)$). The result is shown in Fig. 2.3.8. As we can see, the effects are minimal for small average separations where the averaging is over a relative small spread of phase shifts, and become more pronounced for larger separations.

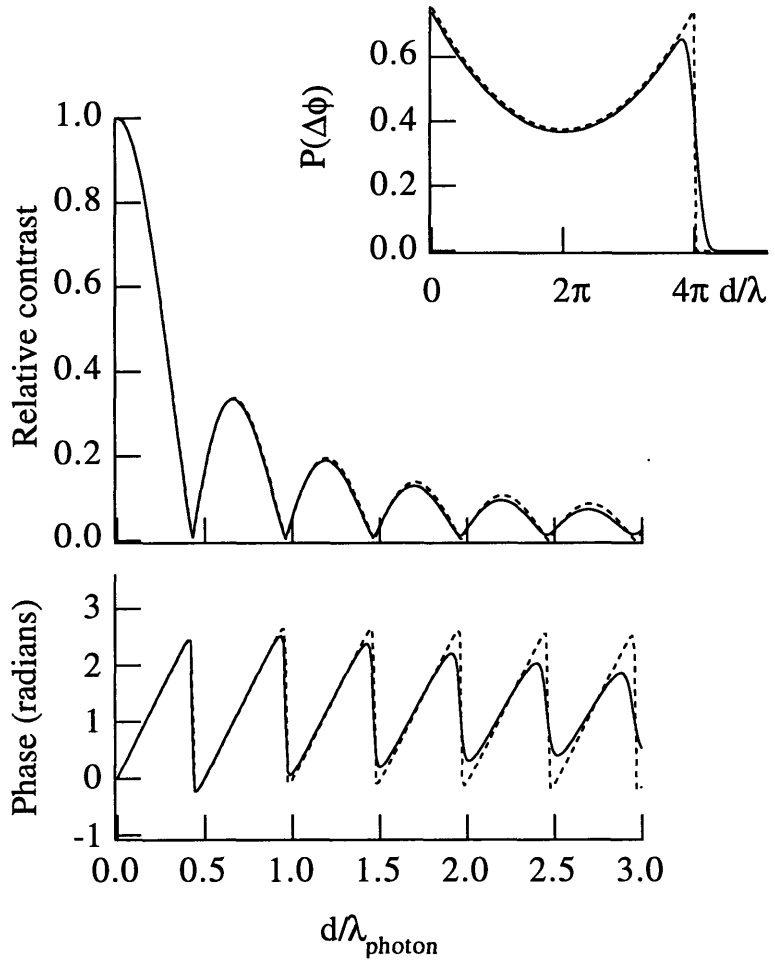

Fig. 2.3.8 The effects of an atomic beam with a 5% rms velocity distribution (solid curves) characteristic of a supersonic expansion source compared to a monochromatic beam (dashed curves). Although the distribution of momentum transfer $P(\Delta k_x)$ is unaltered, the distribution of phase shifts $P(\Delta\phi)$, $\Delta\phi = \Delta k_x d(v)$ is smoothed out asymmetrically.

Scattering more or less than a single photon

The other effect we need to consider to model our experiment is the effects of scattering more or less than a single photon. As will be described later, to scatter a single photon for each atom, we excite the atoms as they traverse a resonant laser beam. The

power of the beam is adjusted so that the atom leaves the beam in the excited state, shortly after which it spontaneously decays. Due to the possibility of decay during this excitation, there will always be some atoms that are not fully excited (i.e. do not scatter any photons) or that cycle more than once and scatter more than one photon. The net relative phase shift imparted to an atom scattering N photons is just given by the sum of the individual events

$$\Delta\phi_{total} = d\sum_{i=1}^{N}\Delta k_{x,i} \tag{2.24}$$

Hence, we need only to calculate the net distribution of Δk_x—the total transverse momentum imparted to the atom. For our purposes, it will suffice to limit N to 2. The distribution $P_2(\Delta k_x)$ corresponding to 2 scattering events is given by the auto-correlation function of $P(\Delta k_x)$ [MAN79], and is

$$\begin{aligned} P_2(\Delta k_x) &= \frac{9}{64k}\left[4\eta - 4\eta^2 + 2\eta^3 - \eta^4/3 + \eta^5/30\right] \quad \text{for} \quad 0 \le \eta \le 2 \\ &= f(4-\eta) \quad \text{for} \quad 2 < \eta \le 4 \end{aligned} \tag{2.25}$$

where $\eta \equiv \Delta k_x/k$. This distribution, shown in the inset to Fig. 2.3.9, is peaked at $\Delta k_x = 2k$. Also shown in this figure is the contrast and phase of the atomic interference pattern corresponding to scattered exactly two photons from each atom. In this case, the contrast falls off much faster, however weak revivals still persist. The phase shift now increases continuously with a slope of 4π determined by the average $\Delta\bar{k}_x = 2k$ whereby $\Delta\bar{k}_x d = 4\pi(d/\lambda)$.

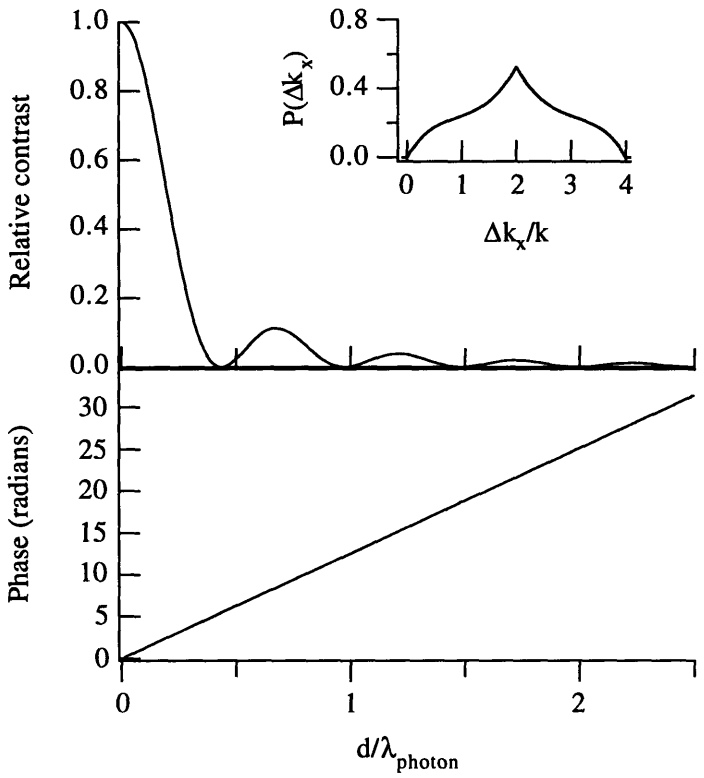

Fig. 2.3.9: The contrast and phase of the atomic interference for the case in which each atom scatters exactly 2 circularly polarized photons. The contrast falls off faster than for one photon scattering, and the phase increases in a continuous fashion with a slope of 4π.

In general, of course, we try to minimize the probability that the atoms scatter either no photons or two photons. To examine the less than ideal cases, we use the net distribution of Δk_x expressed as

$$P_{total}(\Delta k_x) = w_0\delta(\Delta k_x) + w_1 P(\Delta k_x) + w_2 P_2(\Delta k_x) \tag{2.26}$$

or equivalently

$$\begin{aligned} A_{total}(d) &= w_0 + w_1 A(d) + w_2 A_2(d) \\ B_{total}(d) &= w_1 B(d) + w_2 B_2(d) \end{aligned} \tag{2.27}$$

where $w_{0,1,2}$ refer to the percent of zero, one and two photon events, and $A_2(d)$ and $B_2(d)$ are the transforms of $P_2(\Delta k_x)$. In Fig. 2.3.10, we examine the effects of different fractions of atoms that scatter no photons. We note that both phase and contrast are significantly altered. As expected, as the fraction of atoms that scatter no photons increases, the resultant atomic interference more closely resembles its original form (i.e. the relative contrast tends toward unity and the phase shift tends toward zero).

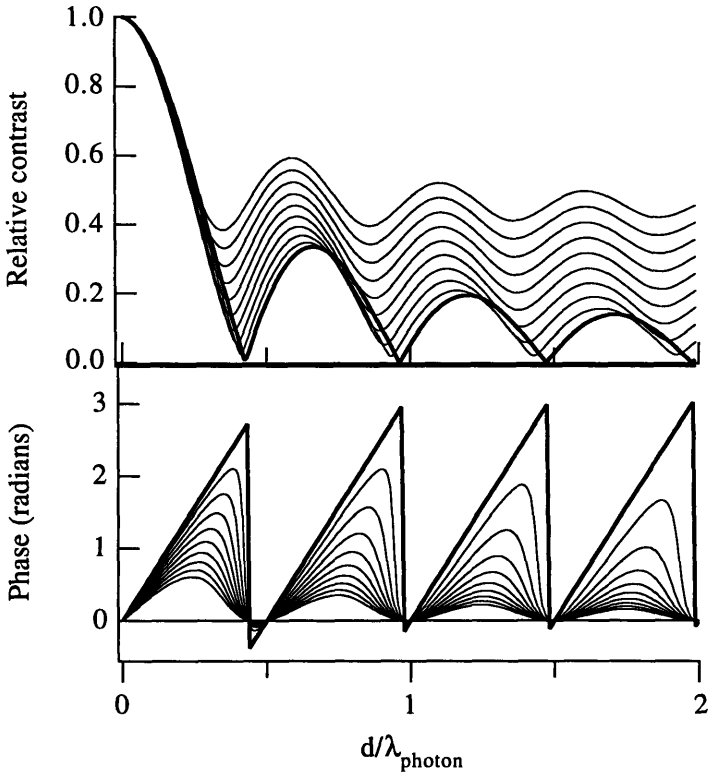

Fig. 2.3.10 The contrast and phase of the interferometer for different fractions of atoms that do not scatter any photons. The thin curves are for 5-45% zero photon scattering progressively. The thick curves are for 100% single photon scattering.

In Fig. 2.3.11, we show similar curves for different fractions of 2 photon scattering events. Notably, the phase is largely insensitive to this variation, however, the strength of the contrast revivals diminishes with increasing number of 2 photon events.

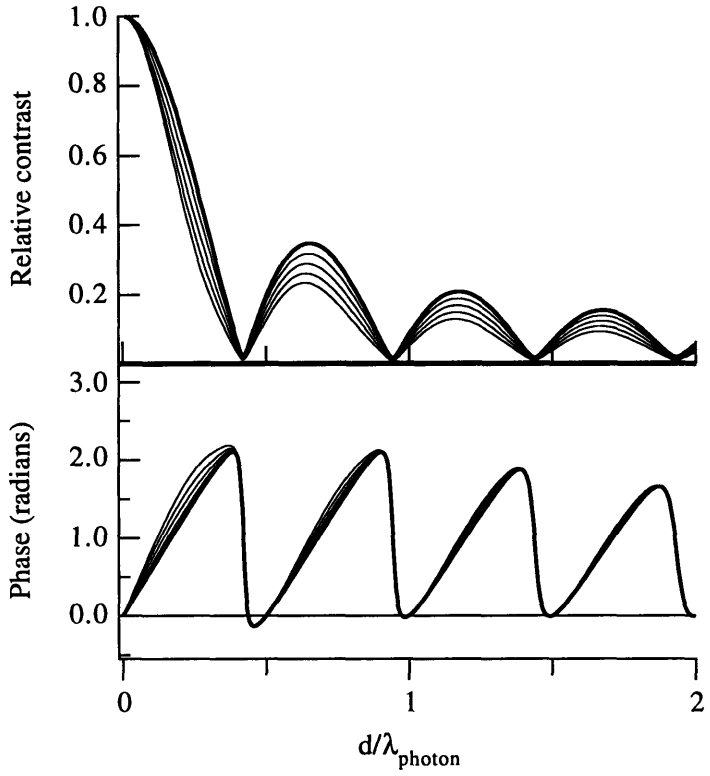

Fig. 2.3.11 The contrast and phase of the interferometer for different fractions of atoms that scatter 2 photons (10-40% progressively (thin lines), 0% thick line). For all the curves in this plot, the ratio of zero to one photon events is held fixed at 5%.

2.3.2. Recovering the lost coherence in a correlation experiment

As we have discussed, if the direction of the scattered photon is well-determined, there will be no loss of contrast in the atomic fringe pattern, but the pattern will acquire a phase shift $\Delta\phi = \Delta\vec{k} \cdot \vec{d} = \Delta k_x d$. So if the direction of the final photon were measured for each atom, we could fully recover the contrast of the atomic fringe pattern by considering only those atoms that scattered photons in a particular direction or sorting the atomic counts according to the directions of the measured photons.

A standard technique for this type of correlation experiment is using coincidence detection of the photons and atoms. A single-photon detector is required for this technique, and one counts only the atoms detected in coincidence with the detection of a photon. To achieve good photon angular resolution, the solid angle acceptance of the photon detector would be limited. An example of what one could expect for a limited, but finite, angular acceptance of the photon detector is shown in Fig. 2.3.12.

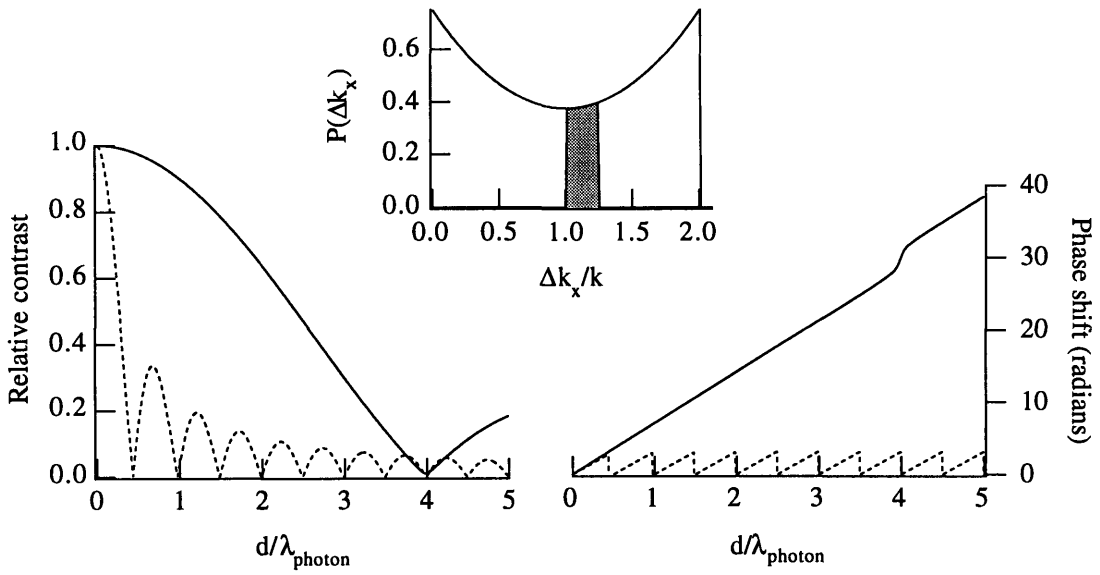

Fig. 2.3.12 The contrast and phase of the atomic fringes calculated for a coincidence experiment (solid lines) compared with the original uncorrelated case (dashed lines). For the coincidence experiment, the angular acceptance of the photon detector is arranged to accept only photons that scattered with $1.0k \leq \Delta k_x \leq 1.25k$ as indicated in the central figure.

Even though the angular acceptance of the photon detector is only ~15°, the effects on the contrast and phase of the atomic fringes are very pronounced when compared to the uncorrelated case. The contrast falls off much more slowly and does not fall to zero until $d = 4\lambda$, which corresponds to the fact that the modified detector acceptance has reduced the width of the distribution $P(\Delta k_x)$ by a factor of 8. The effects on the phase of the fringes is equally pronounced: rather than ratchetting back to zero, the phase continues to increase with a slope of ~2.25π determined by $\Delta\bar{k}_x = 1.125k$ whereby $\Delta\bar{k}_x d = 2.25\pi(d/\lambda)$. Similarly to the uncorrelated case, the phase undergoes a π jump at the point where the contrast disappears.

The technical challenges associated with realizing a coincidence experiment such as this are significant. In our experimental apparatus, the principle limitation is the

relatively slow response time of the atom detector (~1 ms). To prevent or minimize false coincidence counts, the atom beam flux at the point of scattering would have to be limited to significantly less than 1 kHz times the photon detector efficiency. At such a low rate, it would be very difficult to extract the photon or the atomic signal from the background.

Instead, we have devised a different type of correlation experiment that uses the transverse momentum imparted to the atom by the scattered photon to spatially select atoms based on the direction of the photons they scattered. In a sense, it is equivalent to a coincidence experiment with 100% photon detection efficiency (even though we do not detect the photon) because the atomic momentum and photon momentum are entangled. The basic idea of the experiment is depicted in Fig 2.3.13. For the uncorrelated experiment, a wide detector was employed to detect all the atoms, irrespective of the direction of the scattered photon. For the correlation experiment, a narrow detector was used to detect only those atoms that scattered photons within a particular range of Δk_x. Note that this method only selects the atoms based on the transverse component of the recoil momentum, however this is the optimum choice because only this component affects the atomic interference.

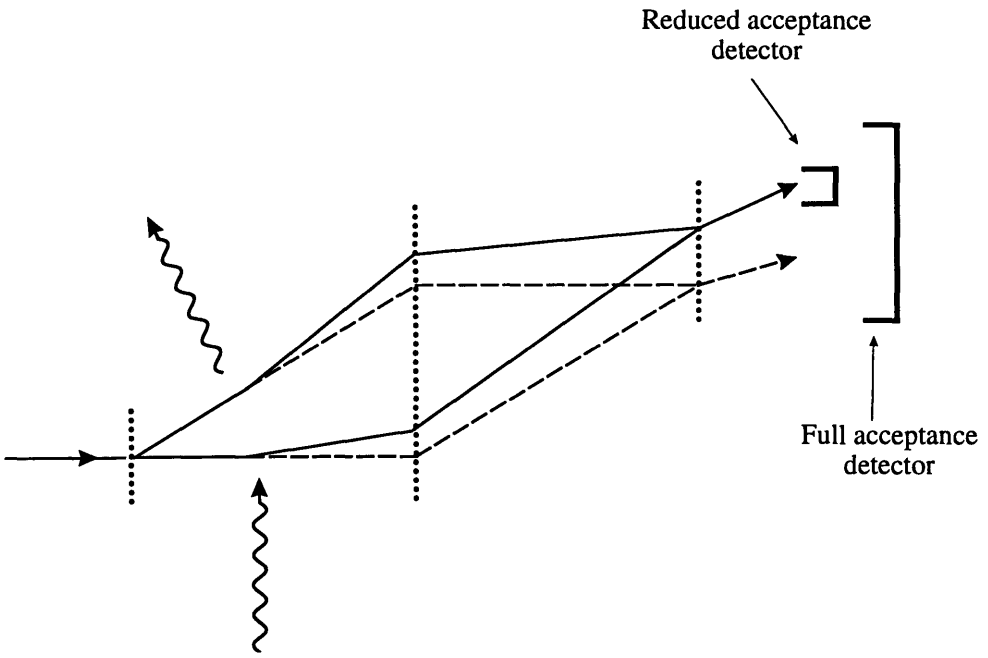

Fig. 2.3.13. The basic idea for the correlation experiment is quite simple. A narrow atom detector is used to select atoms based on the transverse momentum recoil imparted by the scattered photon. In the case shown in this figure, the narrow atom detector is situated to accept the deflected atoms (solid trajectories) and not the undeflected atoms (dashed trajectories corresponding to forward scattering of the photons).

Final beam profile at 3g

Of course this method can only work if the magnitude of the momentum recoil is larger than the initial distribution of transverse momenta in the atomic beam. Indeed, the resolution of this technique is determined by this ratio in conjunction with the acceptance (or width) of the detector. This is illustrated in Fig. 2.3.14 in which the initial beam profile in plane of the detector is shown along with profiles for the photon scattering. These distributions, $I_f(x)$ are calculated by convolving the initial trapezoidal profile $I_0(x)$ with the distribution of deflections due to the photon scattering, $P(\Delta x)$,

$$I_f(x) = \int dx' P(x - x') I_0(x') \tag{2.28}$$

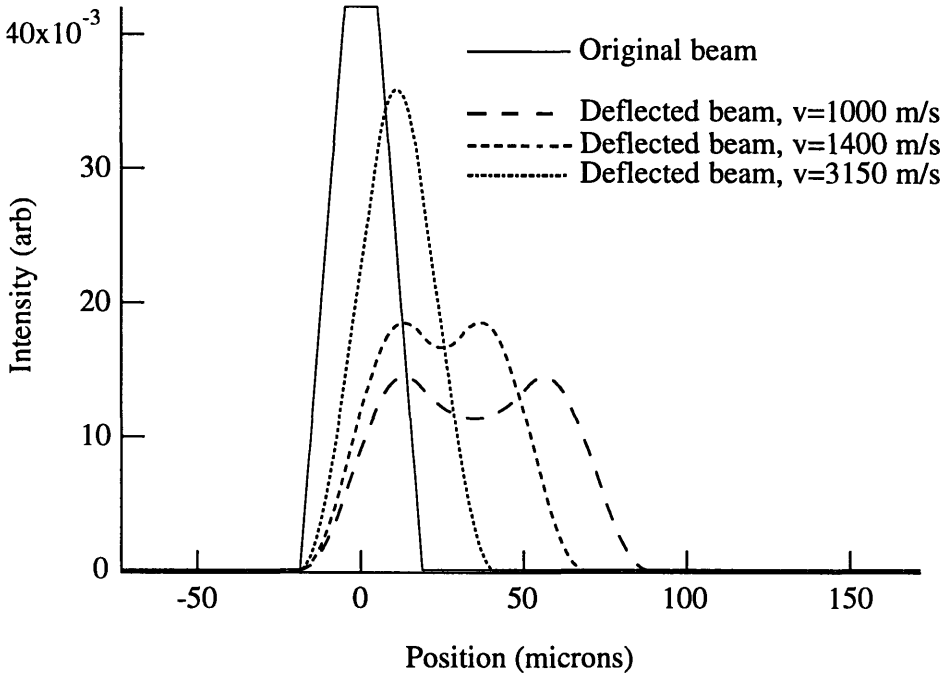

Fig. 2.3.14 The normalized intensity profiles of the atom beam at the third grating for scattering a single photon from atomic beams with different velocities. These are compared with the original intensity profile determined by the collimation geometry (two 10 μm slits separated by 87 cm).

The transverse momentum spread of the atomic beam is determined by the collimation geometry and the beam velocity. For 10 μm slits separated by 87 cm as in our machine, the angular divergence of the beam is ~12 μrad which corresponds to transverse velocity spread of 3.7 cm/s for a beam velocity of 3200 m/s and 1.2 cm/s for a beam velocity of 1000 m/s (note that we have ignored diffraction from the 2nd slit, which begins to be appreciable (~2 μrad angular divergence for a 1000 m/s beam velocity). These are comparable to the recoil velocity $\hbar k / m$, which is 2.9 cm/s for sodium. From

Fig. 2.3.14, it is clear that greater selectivity for a given collimator geometry is provided by slower atomic beams.

Calculating the modified distributions

Because of the initial transverse velocity distribution of the atomic beam, the subset $P'(\Delta k_x)$ of the full distribution $P(\Delta k_x)$ selected using this method will not be as sharply defined as the hypothesized case depicted in Fig. 2.3.12. The new distribution $P'(\Delta k_x)$ is determined by first calculating the distribution in the spatial domain

$$P'(\Delta x) = \int dx'\, I_0(x') P(\Delta x - x') W(x_0 - x') \tag{2.29}$$

where $W(x)$ is the window function of the narrow detector

$$\begin{aligned} W(x) &= 1 \quad \text{for} \quad -\Delta w/2 < x < \Delta w/2 \\ &= 0 \quad \text{otherwise,} \end{aligned} \tag{2.30}$$

Δw is the width of the detector opening (in our case determined by the width of the 3rd grating window) and x_0 is the offset of the detector opening from the undeflected beam centroid. From $P'(\Delta x)$, the corresponding distribution in momentum space $P'(\Delta k_x)$ is found by using the relation $\Delta x \approx 2L\Delta k_x / k_{atom}$ (valid for $z << L$ as is the case here).

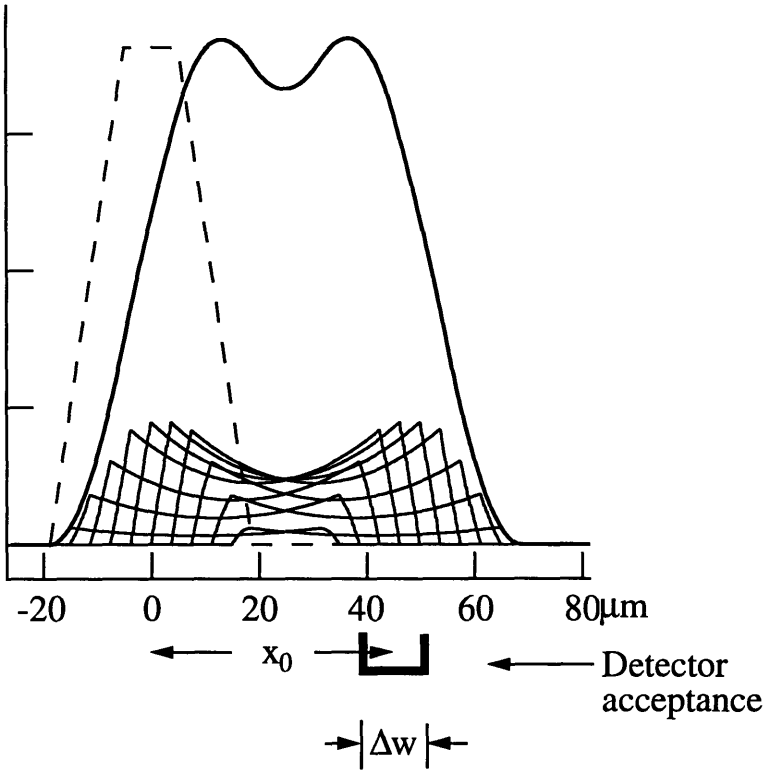

Fig 2.3.15 This figure illustrates the calculation of $P'(\Delta k_x)$. The initial beam profile (dashed) is sliced up into many pieces, each of which is spread out by the photon recoil (thin lines of small amplitude). The sum of these contributions is represented by the thick line.

Once the modified distribution $P'(\Delta k_x)$ is found, the relative contrast and phase shift are calculated in the same manner as before. One such calculation is shown in Fig 2.3.16 for a 10 μm collimating slits, a 10 μm wide 3rd grating and a beam velocity of 1400 m/s. As we can see, the net result is very similar to the calculation for the coincidence technique in Fig. 2.3.12. In this case, because the subselected distribution $P'(\Delta k_x)$ is not sharply delimited on both sides as in Fig. 2.3.12, the contrast does not exhibit revivals, but instead gradually declines. In this case, the detector position was chosen to preferentially detect atoms that scattered with $\Delta k_x = 2k$, and hence the phase increases as $\Delta\phi = 4\pi(d/\lambda)$. Note that the area under $P'(\Delta k_x)$ is not normalized to one

as it was $P(\Delta k_x)$; this reflects the fact that we are selecting only a limited subset of the original distribution.

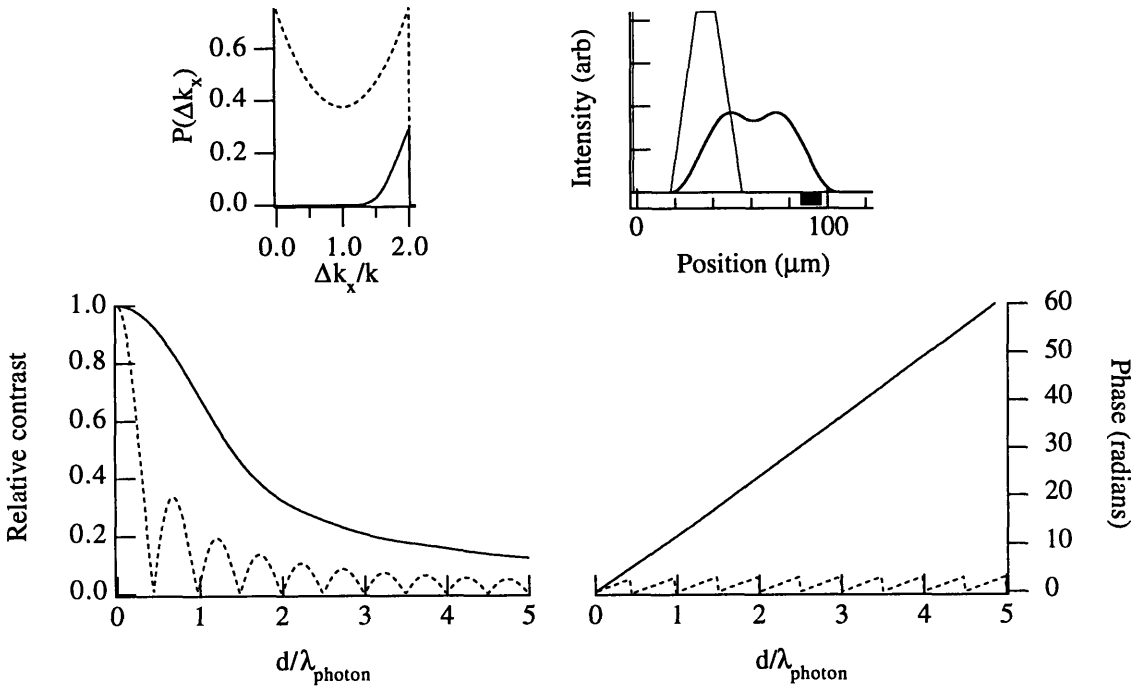

Fig. 2.3.16 The contrast and phase of the atomic fringes calculated for the correlation experiment (solid lines) compared with the original uncorrelated case (dashed lines). The upper left graph shows the detected distribution $P'(\Delta k_x)$ of photon recoils along with the original distribution $P(\Delta k_x)$ (dashed). The upper right graph shows the width and position of the detector (solid rectangle) with respect to the initial and deflected atomic beam profiles. Note that the profiles are offset from the collimation axis (of the 2 slits)—this is the offset of the interfering paths of the interferometer as shown in Fig. 2.3.13.

Other considerations

As in the uncorrelated case, we need to consider the effects of the velocity distribution of the atomic beam and imperfect single photon scattering. For the case of imperfect single photon scattering, we proceed as before by incorporating additional terms into $P(\Delta x)$ (again, we find it more convenient to work in the spatial domain)

$$P_{total}(\Delta x) = w_0\delta(\Delta x) + w_1 P(\Delta x) + w_2 P_2(\Delta x) \tag{2.27}$$

as in Eq. 2.26. This distribution is then used in Eq. 2.29 to find the subselected distribution $P'(\Delta x)$ from which we can determine the relative contrast and phase shift of the atomic fringe pattern. The effects of the finite velocity distribution are also calculated as before by averaging over the distribution of separations $d(v)$ of the interfering components at the point of scattering. An example of the combination of these effects is shown in Fig. 2.3.17. The configuration studied in this figure is identical to that in Fig. 2.3.16, except instead of 100% single photon scattering, we assume that only 80% of the atoms scattered a single photon, and that the rest either do not scatter any photons (5%) or scatter two (15%). Additionally, we include the effects of a 5% velocity distribution of the atomic beam.

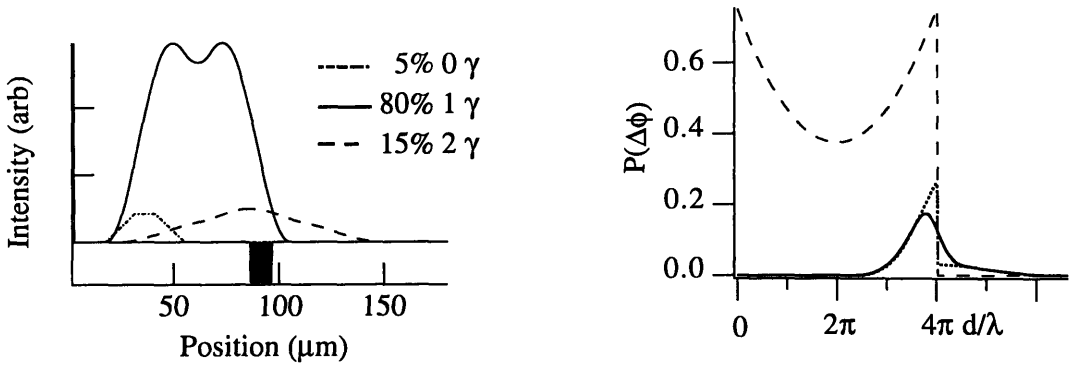

Fig 2.3.17 The left graph shows the undeflected atomic beam profile (dotted), the deflected profile for one photon scattering (solid) and the deflected profile for two photon scattering (dashed). The relative height of these profiles corresponds to their relative weight (5%, 80% and 15% for zero, one and two photon scattering respectively). The width and position of the detector is indicated by the filled rectangle. The right graphs shows the detected distribution (dotted) compared with the original (dashed). The solid curve includes the averaging over the 5% velocity distribution.

In the left graph of the figure, the initial atomic beam profile is plotted along with the single photon scattering and two photon scattering deflected profiles, each weighted their relative abundance (i.e. 5%, 80% and 15% weighting respectively). It is clear that in this case, the atoms that do not scatter any photons are not accepted by the detector, and therefore do not have any effect. This is not true for the two photon scattering contribution, which modifies the accepted distribution $P'(\Delta\phi)$* as shown in the right graph—the distribution now has a tail corresponding to momentum transfers with $\Delta k_x > 2k$ associated with two photon events. The effect of the 5% velocity distribution is to smooth out the sharp transition at $\Delta\phi = 4\pi d / \lambda$ in the distribution $P'(\Delta\phi)$ (right graph, solid curve).

---

* recall that $P'(\Delta\phi)$ is obtained by substituting $\Delta\phi = \Delta k_x d(v)$ into the expression for $P'(\Delta k_x)$ (see Fig. 2.3.7)

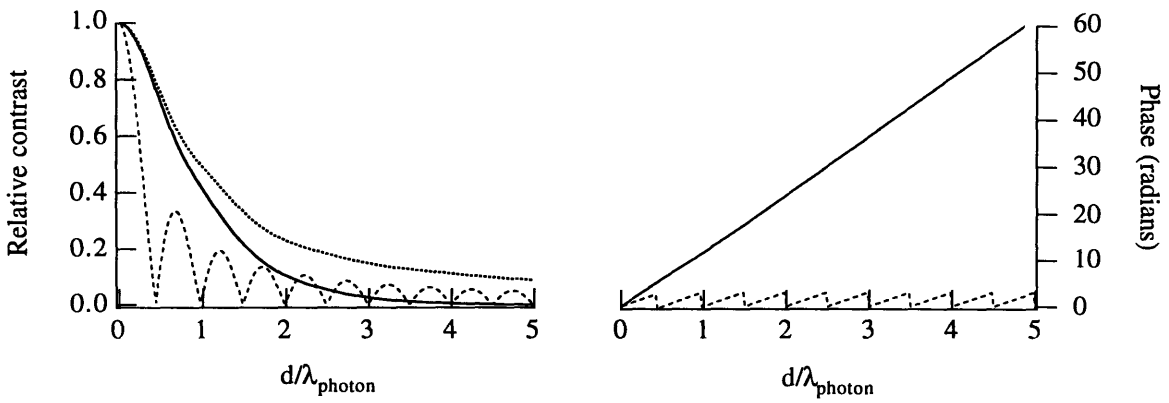

Fig 2.3.18 The contrast and phase of the atomic fringes for the distribution $P'(\Delta\phi)$ in Fig 2.3.17 (solid and dotted lines) compared with the original uncorrelated case (dashed). The solid curves are for a 5% velocity distribution, while the dotted curves are for a monochromatic velocity.

The contrast and phase calculated using $P'(\Delta\phi)$ are shown in Fig. 2.3.18. The effects of the 15% two photon events are not that significant in this case, as can be seen by comparing the contrast and phase in this figure to Fig. 2.3.16 where 100% single photon scattering was assumed. The 5% velocity distribution has a negligible effect on the phase, however the contrast damps out to zero considerably faster. Indeed, the effect of a 5% velocity distribution on the contrast is much more significant here than in the uncorrelated case (see Fig. 2.3.8). This is because, here, the distribution $P'(\Delta k_x)$ is concentrated around $\Delta k_x = 2k$, and hence the relative change of the corresponding distribution $P'(\Delta\phi)$ due to the average over $d(v)$ is much larger than in the uncorrelated case. Note that for the same reason, the effects of the velocity distribution for $P'(\Delta k_x)$ centered around $\Delta k_x = 0k$ are much less than in the case shown here.

Other interference orders

To simplify the discussion, up until now we have only considered two interfering paths in the atom interferometer. Not only is there another pair of interfering paths symmetric to the collimation axis, but there are many other diffracted orders contributing to the total atomic intensity in the plane of the third grating. Several of these other paths are shown in Fig. 2.3.19 (their mirror counterparts are not shown).

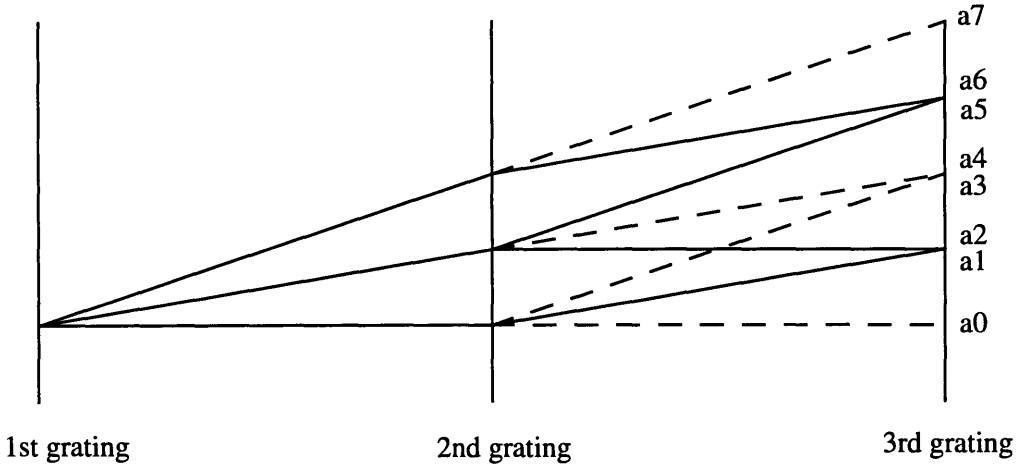

Fig. 2.3.19 Several of the more significant paths in the interferometer (their mirror counterparts are not shown). Usually, we are only concerned with the interferences between paths a1 and a2, however, for a 1st grating with a small open fraction, interferences between paths a5 and a6 (which have equal path length) can become important. The dashed paths do not contribute to the interference signal, however they reduce the contrast of the interference fringes if they contribute to the detected signal.

The relative amplitude of the different paths depends on the open fractions of the 1st and 2nd gratings (see e.g. [BOW80] and also [ECK93] for a discussion specific to our interferometer) and are listed in Table 2.1. The average intensity at each location is given by a sum of each amplitude squared (e.g. $[(a1)^2 + (a2)^2]$ for our usual fringe envelope), whereas the relative interference signal is given by the cross-term 2(a1*a2). The interference term 2(a5*a6) can be important if the open fraction of the 1st grating is small

(< 40%), but it is usually insignificant for 1st grating open fractions close to 50%, in which case the amplitude a6 is very small.

Path	Relative amplitude
a0	$\beta_1\beta_2$
a1	$\beta_1\beta_2\mathrm{sinc}(\pi\beta_2)$
a2	$\beta_1\mathrm{sinc}(\pi\beta_1)\beta_2\mathrm{sinc}(\pi\beta_2)$
a3	$\beta_1\beta_2\mathrm{sinc}(2\pi\beta_2)$
a4	$\beta_1\mathrm{sinc}(\pi\beta_1)\beta_2$
a5	same as a2
a6	$\beta_1\mathrm{sinc}(2\pi\beta_1)\beta_2\mathrm{sinc}(\pi\beta_2)$
a7	$\beta_1\mathrm{sinc}(2\pi\beta_1)\beta_2$

Table 2.1: Amplitudes of some of the more important paths in the interferometer. β_i refers to the open fraction (ratio of slit width to grating period) of the ith grating. Note that for gratings with smaller open fractions, higher order diffracted paths become more significant and should be included. [note: $\mathrm{sinc}(x) \equiv (\sin x)/x$]

In Fig. 2.3.20, the average atomic intensity profile in the plane of the 3rd grating is shown for 1st and 2nd grating open fractions close to 50% and a beam velocity of 3000 m/s. In this case, the different orders are partially overlapping so the contributions from the different orders must be added to determine the intensity at a given location,. This is also true for the *interference* signal. In particular, with reference to Fig. 2.3.19, the interference signal at 0 μm is the (incoherent) sum of the separate interference patterns corresponding to the two interference orders in solid outline (i.e. there are no additional interferences between a given path and its mirror counterpart).

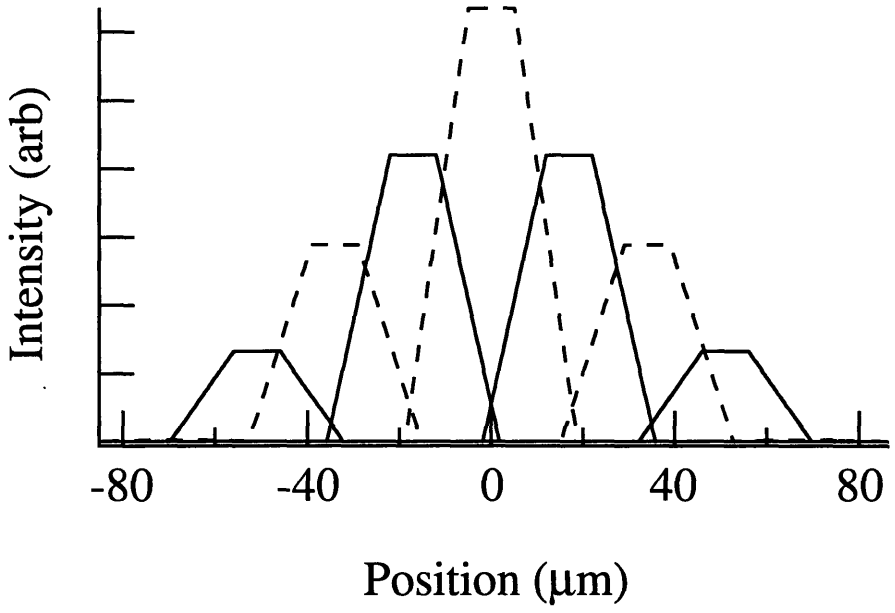

Fig. 2.3.20 Average atomic intensity profile in the plane of the 3rd grating for the paths shown in Fig. 2.3.19. This is for 1st and 2nd grating open fractions of 47% and a beam velocity of 3000 m/s. The solid curves show the locations of possible interference, while the dashed curves correspond to non-interfering contributions (background). Note that in this case, the intensity in the +/- 3rd orders (centered at +/- 52 ¨μm) is almost entirely due to path a5, and the interference signal in this order is actually negligible.

The presence of the other interfering orders can result in very curious effects for particular detector locations in the correlation experiment. This is illustrated in Fig. 2.3.21, where the detector is located in a region of overlap for the deflected beam profiles (upper left graph). As a result, the detected distribution $P'(\Delta k_x)$ has contributions from both interference orders. However, the contribution from the left interference order at this location is peaked around $\Delta k_x = 2k$ and the contribution from the right interference order is peaked around $\Delta k_x = 0k$. Hence, when they are summed, the resulting $P'(\Delta k_x)$ is very similar in structure to the original, uncorrelated distribution. As a result, the contrast of the atomic fringe pattern versus the separation

shows revivals as in the original uncorrelated experiment, however, the strength of the revivals is higher because of the increased peak to valley heights in $P'(\Delta k_x)$.

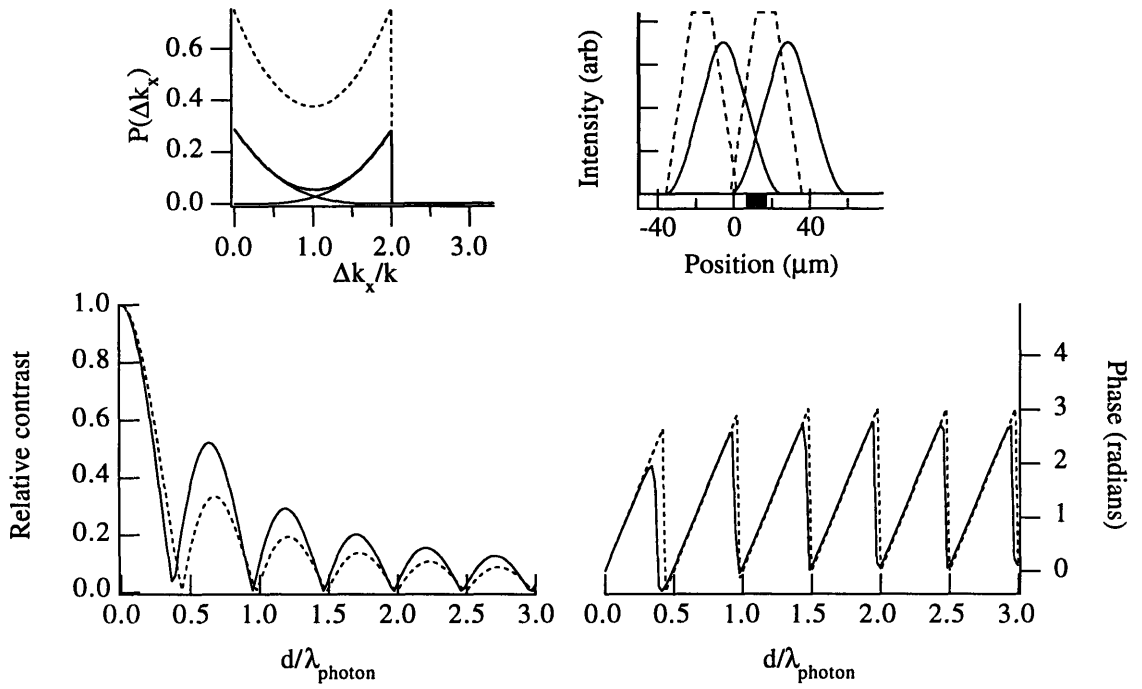

Fig. 2.3.21 A case in which the detector is located at a position of overlap between the two interference orders originally symmetric to the collimation axis (upper right graph, the dashed lines correspond to the undeflected beam profiles, and the solid lines are the deflected profiles). The upper left graph shows the contributions from each interference order to the total detected distribution . The lower graphs show the atom fringe contrast and phase (solid curves) compared with the uncorrelated case (dashed curves).

2.4. Experimental Details

In this section, I will describe some of the experimental apparatus and techniques we used to carry out this experiment.

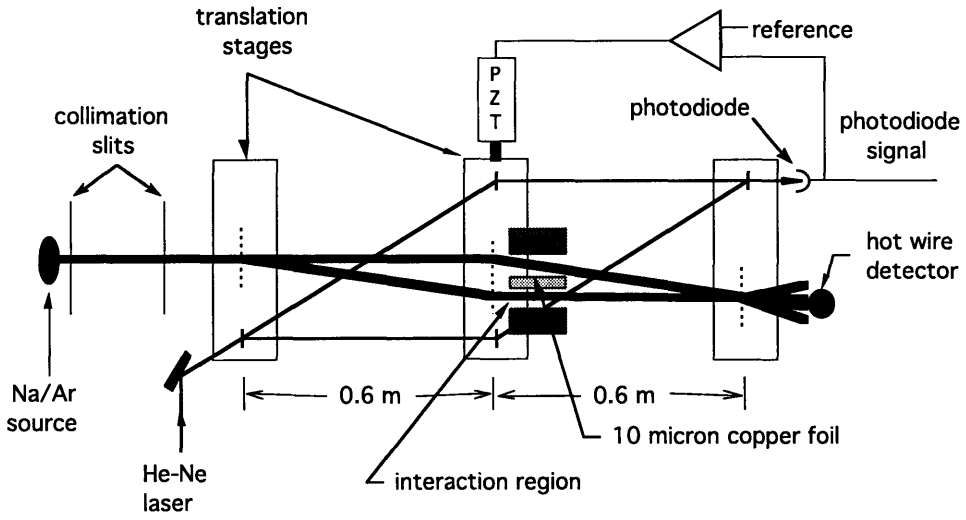

Fig 2.4.1: A schematic, not to scale, of our atom interferometer (thick lines are atom beams). The 10 cm long interaction region with the 10 μm thick copper foil between the two arms of the interferometer is positioned behind the 2nd grating (not used for the experiments in this chapter). An optical interferometer (thin lines are laser beams) measures the relative positions of the 200 nm period atom gratings (which are indicated by vertical dashed lines).

2.4.1 The MIT atom interferometer

The interferometer used for these experiments was first demonstrated in 1991. Although many improvements have been realized since then, many necessary to make it a separated beam interferometer, the machine is fundamentally unchanged. A schematic of the experimental apparatus is shown in Fig. 2.4.1. It features an atomic beam machine

with high atomic flux and a narrow velocity distribution. Three nanofabricated diffraction gratings are used for the (matter) optical elements of the interferometer. Below, I will describe these elements, and I will summarize modifications we made.

Item	Dimension
atom grating period	200 nm
laser grating period	1.333 μm
source – 1st slit dist.	~15 cm
distance between slits	87 cm
2nd slit – 1st grating dist.	~10 cm
grating separation	66 cm
3rd grating – detector separation	26 cm
total (source-detector)	~204 cm

Table 2.1: Some important dimensions in the machine.

The atomic beam machine

The atomic beam machine features: (1) a ~3 m long multi-sectioned vacuum chamber, (2) a supersonic inert gas expansion source seeded with sodium, (3) narrow beam collimation, and (4) a scanning hot-wire ionization detector for the sodium.

Although unassuming in appearance, this machine† has a rich history including the work performed in this lab on atomic diffraction from standing light waves [MOW84], [GOU85], [MAR87], [OLD90], the first demonstration of diffraction from a

† much of apparatus is from a machine originally constructed to do RF spectroscopy of van der Waals molecules [MAT74].

nanofabricated grating, the demonstration of one of the first atom interferometers [KEI91],* and the demonstration and use of the only atom interferometer with physically isolated interfering beams [EKS93]. The research performed with this machine has been the source of over 20 refereed papers and 7 Ph.D. theses over the last ten years.

This beam machine has been described many times, most recently in Chris Ekstrom's thesis [EKS93], but the reader is also referred to the detailed discussions in [GOU85] and [MOW84].

The vacuum chamber

The vacuum chamber is divided into three sections: (1) the source/differential pumping chamber, (2) the main chamber, and (3) the detector chamber. These are separated by homemade plexiglass gate valves that can be closed to individually isolate each chamber. The supersonic source in our apparatus produces a significant gas load (~0.5 torr ℓ / sec) and the basic strategy behind the vacuum system is to use a series of differential pumping regions with small openings between the chambers to improve the vacuum in each successive stage of the machine. Basic parameters of the system are given in Table 2.2.

* published simultaneously with the Young's two-slit demonstration by Mlynek's group [CAM91]

Section	Pump	Typical pressure	
source	Stokes ring jet diffusion	~2-8 x 10^{-3}	torr
1st differential	NRC 10" diffusion	~5 x 10^{-6}	
2nd differential	4" diffusion	~5-8 x 10^{-7}	
main chamber	NRC 4" belly diffusion	1-4 x 10^{-7}	
detector	Varian V80-A turbo	1-3 x 10^{-7} 3-7 x 10^{-8}	 (cold-trapped)

Table 2.2: Some parameters of the vacuum system

No major changes were implemented in the vacuum system, however I will make note of a few minor changes and general observations. First with regard to the Stokes pump. We found it necessary to boost the 208 line voltage to the Stokes pump by an additional 30 volts or so (by using a variac with an isolation transformer) in order to sufficiently heat the oil reservoir (the reservoir should be ~210°C). The pump is designed to operate at 230V thus it is not so surprising that this was necessary. The pump oil should be checked every 2 months—it seems to be consumed on that time scale and the pump will overheat dangerously if it runs dry.

Our strategy on vacuum bakeouts of the machine and general vacuum practices continues to evolve. Although in the past we have tried to improve the vacuum in the main chamber and detector chamber by gently baking at ~60°C (a limit imposed by the motorized micrometers in the chamber), our current feeling is that this is probably not necessary and may instead hasten the demise of the variety of motorized positioners in the machine. Even after being open to air for ~2 weeks, it takes only 2-3 days for the vacuum in the main chamber to fall below the 1 x 10^{-6} level.

The source

The atomic sodium beam is produced in an inert gas supersonic expansion seeded with sodium vapor. The most important feature of this source is that it produces a beam with a narrow longitudinal velocity distribution (< 5% rms), which is necessary for most of the experiments we have undertaken. An additional feature of this source (of which we have taken considerable advantage) is that the velocity of the sodium is (to a good approximation) determined by the mass of the inert "carrier" gas $v \approx \sqrt{5kT/m_{carrier}}$, and hence we can vary the velocity of our source by changing the carrier gas.

Almost all of the previous work performed with this beam machine used argon as the carrier gas, which provided a beam velocity of ~1000 m/s. In order to achieve mostly single photon scattering for the experiments in this chapter, we usually used helium as the carrier gas (~3000 m/s)—the faster beam velocity minimizes the transit time through the excitation laser beam. We experienced a bit of serendipity the first time we ran the source with helium carrier gas. As the source filled with helium, the detected intensity of the sodium beam dramatically increased by a factor of 50—to over 10^5 counts/sec through all three gratings. This increased beam intensity has been of great benefit to the experiments described in this chapter.

One of the first projects I undertook upon joining the laboratory was to rebuild the atomic source.* The new source, although similar in basic design, featured more rugged construction that led to higher reliability. Additionally, this new source provided a much more intense sodium beam (factor of 10). The reasons for this are not entirely clear, however, we may point to some (perhaps) important differences: (1) we now load the source by removing the reservoir completely which allows us to put a full charge of ~20 g

* the details are described in [EKS93]

of sodium in at a time, (2) we purify the inert carrier gas with a two-stage getter system, (3) the carrier gas is more efficiently preheated before entering the reservoir, and (4) the reservoir is cleaned between each loading. We have found it necessary to reload the source every 5-10 experimental runs (~100 hrs) which is slightly inconvenient—a possible improvement would include a larger reservoir and nickel gasket conflat seal for easy access.

We have developed a few new tricks in dealing with the inevitable clogging of the 70 μm nozzle with sodium. Our basic strategy in heating up the source in preparation for a run is to turn on the nozzle and skimmer heaters first, and after they have reached close to full temperature (typically $T_{skimmer} = 500^{o}C$, $T_{nozzle} = 700^{o}C$), the other heaters for the rest of the source are turned on. Following this procedure generally avoids clogging, however, special care is required the first time the source is warmed after reloading. In this case, the temperature of the reservoir should be increased very gradually over 3-4 hrs. If the nozzle does clog, the source can be cycled in ~2 hrs by venting the chamber with nitrogen gas and pulling the source out when its temperature falls below $300^{o}C$. The nozzle typically clogs after a run if the nozzle heater is turned off. A very effective way to unclog the nozzle is to squirt it with water which reacts with the (small) amount of sodium causing the clog. This works best if done before the sodium has had a chance to react with the air. This procedure is usually followed by reaming with a 50 μm wire combined with blasting compressed air back down into the nozzle opening.

A short note about the skimmer. We use a 0.5 mm orifice skimmer manufactured by Beam Dynamics, Inc. (Minneapolis, MN). We have experimented with a smaller 0.2 mm skimmer to try to minimize the gas load into the 1st differential pumping region, and did not notice a significant difference. We have noticed a significantly longer lifetime from the current skimmers we are using which are plated with rhodium to reduce corrosion.

The slits

The collimation for the atomic beam is provided by two slits separated by 87 cm. For most of our experiments (although not those described in this chapter), 20 μm wide stainless steel slits corresponding to 23 μrad beam divergence have provided a nice compromise between beam signal and collimation. The experiments described in this chapter required optically pumping the atomic beam before the slits, and then maintaining this polarization throughout the interaction laser beam (see the subsequent sections). Due to the rapid transit of the atom by a slit, any residual magnetism of the slit could cause non-adiabatic transitions (Marjorana flops) and hence a loss in polarization. We found significant loss in atomic polarization using the stainless steel slits, even after they were demagnetize. The solution was to use silicon slits that we fabricated at NNF using the same techniques that we use for making the grating windows. This offered the added advantage that 5 (parallel) slits with different widths could be written onto one chip which gave us the capability to quickly change the collimation of the beam without having to rotationally realign the slits each time.

Because of the huge increase in sodium flux when He is used as the carrier gas, it was necessary to incorporate a heater to the 1st slit assembly to prevent clogging of the slits. We used a standard co-axial heater by ARI Industries (Addison, IL) similar to those used for the source and found heating the assembly to 100^{o}C to be sufficient.

The detector

The sodium atoms are ionized using a ionizing hot-wire detector [RAM85], and the ions are individually detected by a channeltron electron multiplier (CEM). We use a thin rhenium wire (50 μm diameter) supplied by H. Cross (Weehawken, NJ). The wire is ~1 cm in length and held at each end by a thin crimped s.s. hypodermic tube. The wire is operated at a current of 140 mA which provides a low background rate (typically ~100-

200 counts/sec) and a ~1 ms time response. Between runs, the wire is maintained at 200 mA to keep it clean. Prior to running, we oxidize the wire for ~30 s at 200 mA with 5×10^{-4} torr O_2 to increase the sensitivity of the wire and then step the current down to 140 mA over an hour or so. The height of the atomic beam is restricted to a maximum of 3 mm by an aperture in front of the wire. We tried shortening the length of the wire to 3 mm to reduce the background counts (which we assume to scale linearly with the length of the wire), however the temperature gradients over the active area of the wire became too large.

To obtain the highest angular selectivity in the collimated atomic beam system, it is necessary that the wire be straight and parallel with the collimation slits. The thermal expansion for the wire from room temperature to 850°C is ~85 μm (assuming a thermal expansion coefficient of 10^{-5}/°C) which is more than enough to relax any initial tension applied to the wire during mounting. As a result it is difficult to keep the wire from acquiring a significant bend when hot. To remedy this, we have incorporated a soft leaf spring (folded piece of 0.010" s.s. shim stock) into the wire mounting rig to keep the wire under tension as it heats up, and we have included a mechanical stop to limit the maximum expansion to less than 200 μm so that heated wire is not stretched to the breaking limit—this is shown in Fig 2.4.2. The mechanical limit must be reset each time the wire is cooled back down to room temperature because the wire undergoes permanent (plastic) deformation.

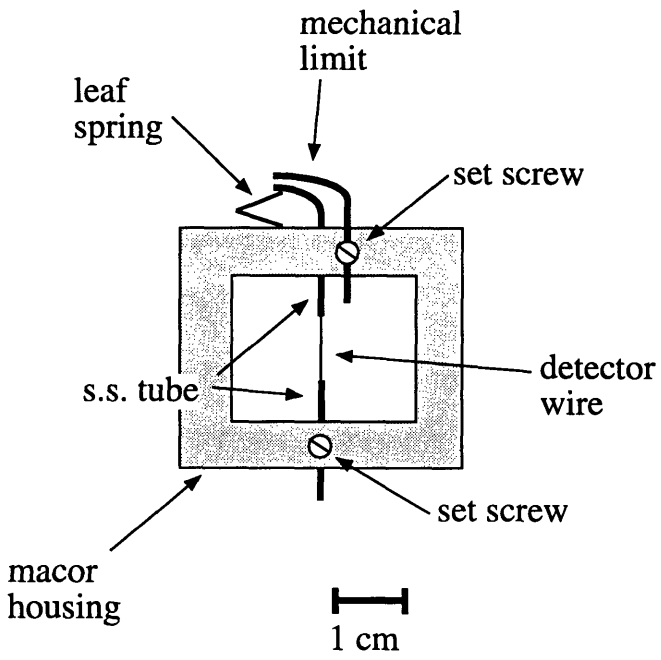

Fig. 2.4.2 Side view of hot wire assembly showing the spring-loading for the wire.

How much beam?

With two 20 μm collimating slits in place (but no gratings), a source reservoir temperature of 650°C, and the detector located on the maximum of the beam profile, we typically measure count rates of about 2000 cps per micron of detector height using argon as the carrier gas and 50 times that for helium carrier gas.

The gratings

We fabricate the gratings at the National Nanofabrication Facility (NNF) at Cornell University. The basic techniques were developed by Michael Rooks and David Keith [KSR91] and remain essentially unchanged. We made recent trips to the NNF in Sept. 93 and Sept. 94 to fabricate additional gratings.

In the first trip, we concentrated on fabricating a large supply of 200 nm period gratings for general use in the interferometer although we also fabricated a small supply

of additional gratings with a variety of periods (294.5, 400, 589, 600, 800 nm) for possible future use. The gratings from this trip performed somewhat worse than those from the previous trip [EKS93] in that the contrast of the atomic fringe pattern was limited to less than 20% with these gratings (compared to 27% for earlier gratings). Nonetheless, these gratings proved to be completely adequate for the experiments in this chapter.

In the second trip, we focused on improving the large scale dimensional coherence of the gratings (i.e. the degree to which the positions of the bars of the grating correspond to the ideal periodic grating). One of the possible source of deviations is thermal drifts of the e-beam during the time it takes to write a grating (~10 min). In order to minimize these effects, we periodically corrected the e-beam registration using reference marks previously written on the gratings. This entailed several extra wafer processing steps (to write and develop the reference marks) and considerably more programming for the e-beam, but the gratings we made using these methods have produced the highest atom fringe contrast to date (43%, see Fig. 1.4). Additionally, with these gratings, the height of the atomic beam can be increased to the full height of the gratings without any loss in contrast.

During this trip, we also made the 200 nm period gratings with narrow 10 μm wide windows needed for the correlation experiment, and we made gratings with extra large areas (800 μm x 800 μm) for use in a Sagnac rotation measurement.

2.4.2 Scattering a single photon

A major challenge of this experiment was developing the techniques to scatter single photons from each atom that traversed the interferometer. The technique we use is spontaneous scattering—the atoms are excited by passing through a resonant laser beam,

after which they decay back to the ground state via spontaneous emission. The laser beam used to excite the atoms is narrowly focused to a ~15 μm waist (FWHM of the field), corresponding to a transit time of 5 ns for atoms traveling at ~3000 m/s (He carrier gas). This is shorter than the lifetime of the excited state (16 ns), thereby minimizing spontaneous emission while the atom is in the laser field and providing better control over the atom-laser interaction. A cylindrical lens is used to defocus the beam in the vertical direction to ensure uniform illumination over the full height of the atomic beam (~1 mm).

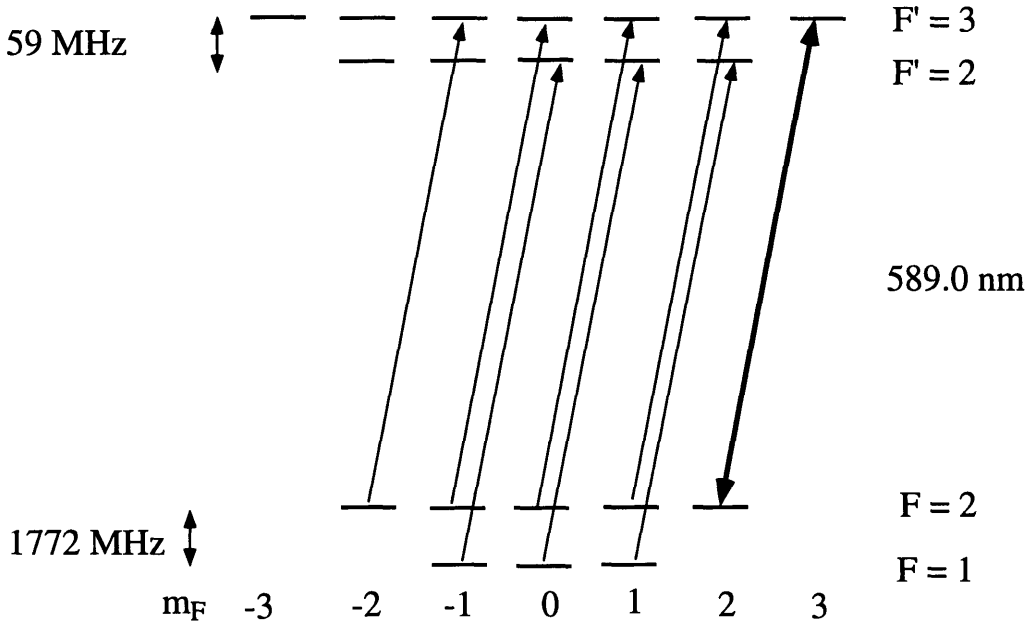

Fig. 2.4.3 Hyperfine structure of the D2 transition of sodium (unimportant levels not shown). The atoms are first optically pumped to the $3S_{1/2}\,F=2,m_F=2$ state to create an effective 2-state system between this state and the $3P_{3/2}\,F'=3,m'_F=3$ excited state. Subsequently the atoms are excited with a π-pulse to scatter a single photon.

The atoms are excited from the $3S_{1/2}\,F=2,m_F=2$ ground state to the $3P_{3/2}\,F'=3,m'_F=3$ excited state using a σ^+ polarized laser beam. This ensures that the excitation and subsequent spontaneous emission occurs within a closed two-state system (see Fig 2.4.3). The atomic beam is prepared in the $3S_{1/2}\,F=2,m_F=2$ state by optical

pumping with a circular polarized laser beam intersecting the atomic beam before the first collimating slit. The laser frequency is tuned to the $F = 2 \rightarrow F' = 3$ resonance and has sidebands at 1.713 GHz to pump the atoms out of the $F = 1$ state. Weak magnetic guide fields (4 gauss) are used to provide a quantization axis for the optical pumping and to maintain the atomic polarization throughout the scattering region, and non-magnetic collimating slits are used to avoid atomic depolarization due to diabatic transitions.

Optics

Laser light at 589.0 nm for our experiment is generated by a Coherent 599 dye laser pumped by a Coherent Innova 90 argon ion laser operating at 514 nm. Typically 150-200 mW of single mode light is generated by the dye laser. The output beam is passed through an EOM to generate sidebands at 1.713 MHz. The light then proceeds to a fiber coupler where it is launched into ~30 m of single mode polarization preserving optical fiber leading to the atomic beam machine. To achieve high coupling efficiency (~50%) without upsetting the stability of the dye laser, it was necessary to install an optical isolator (a Faraday rotator) to prevent the back-reflection from the fiber face from feeding back into the laser.

The optics setup for the optical pumping beam and the locking beam is shown in Fig. 2.4.4.

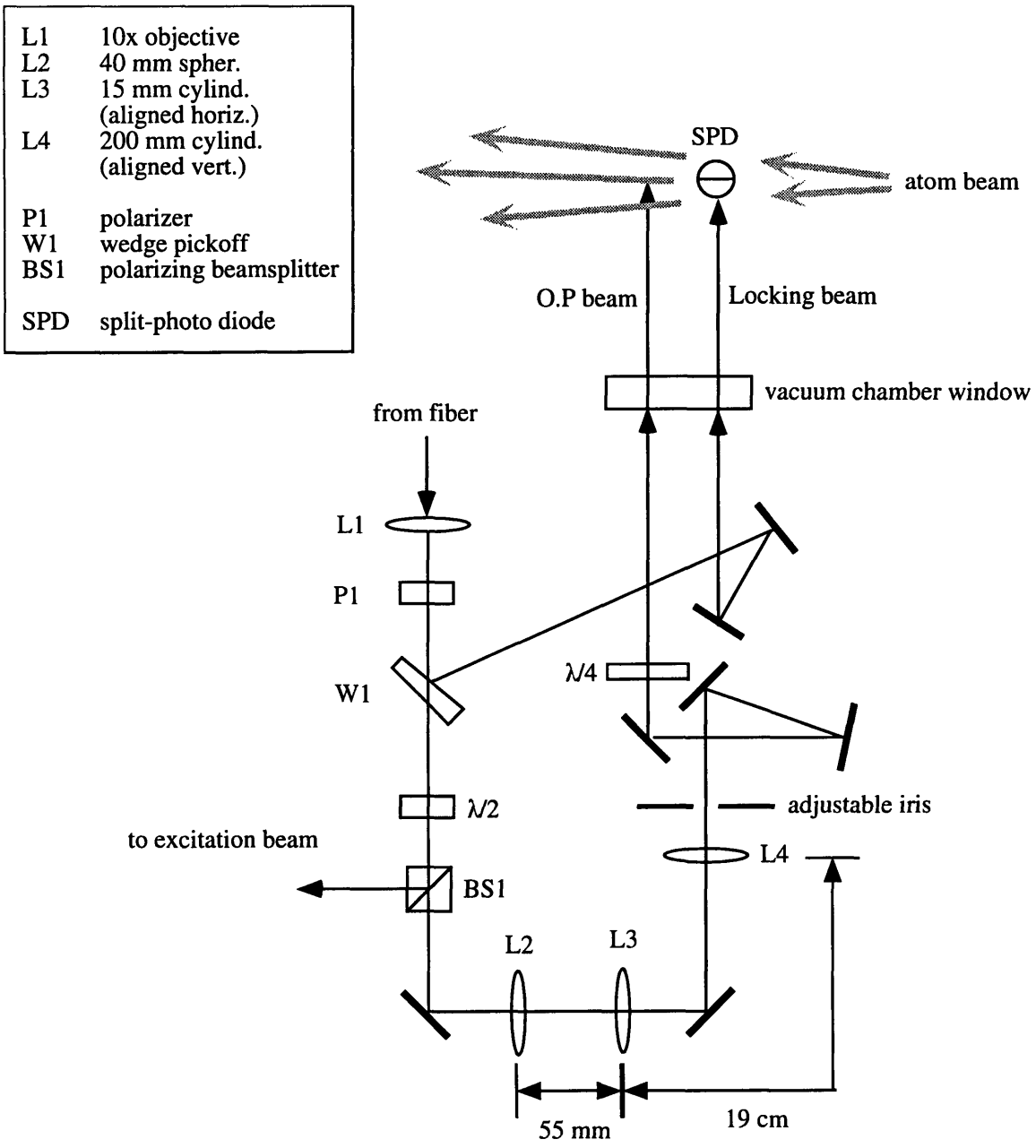

Fig. 2.4.4 A schematic of the optical set-up for the optical pumping beam and the locking beam. This arrangement allows independent angular and intensity control of the optical pumping beam and locking beam. The distance from L4 to the atomic beam is 100 cm. L3 is mounted on a translation stage for adjustable vertical focus of the laser beam, and the adjustable iris is used to set the horizontal width of the beam.

The light exiting the fiber is collimated by a microscope objective (L1), and passed through a linear polarizer to clean up the polarization. A portion of the beam is then picked off with a wedge and directed into the atomic beam for the long term frequency lock servo system. This system is largely the same as in [GOU85]; it uses a split photo diode (SPD) to servo the position of the fluorescent spot in the atomic beam. The position of this spot is frequency dependent due to the spatially varying Doppler shift of the diverging atom beam, and hence the position of the spot is a measure of the laser frequency.

The majority of the laser beam continues through the wedge and passes through a half-wave plate and polarizing beam splitter cube we use as a variable beam splitter between the optical pumping beam and the excitation beam. Using cylindrical lenses, the optical pumping beam is shaped into an ellipse 10 mm along the axis of the atomic beam and 3 mm high. This beam then passes through a quarter wave plate to produce circular polarization and is sent into the vacuum chamber to intersect the atomic beam.

We now turn our attention to the laser beam used to scatter the single photons from the atoms. The principle requirements of the setup for the excitation beam are a very narrow waist (15 μm FWHM of the *field*) along the direction of the atom beam, a uniform field intensity over the height (1 mm) of the atomic beam, and the ability to scan this beam along the atom beam over 10 cm. Additionally, we wanted to keep all of the optics external to the vacuum system for convenient adjustment. The optical set-up we used to fulfill these requirements is shown in Fig. 2.4.5.

The excitation beam is taken from the beamsplitter BS1 and passed through a simple telescope (L5 and L6) to pass through a intensity stabilizer (Thorlabs, CR200-A). The beam chopper is a simple solenoid actuated device controlled by our data acquisition system. The laser beam is spatially filtered using a 5x microscope objective and a 50 μm

pinhole. The beam is then recollimated in the horizontal direction with L8, while a cylindrical lens (L7) defocuses the beam in the vertical direction. The final folding mirror, quarter wave plate and focusing lens (L9) are mounted on a motorized translation stage (T1) which moves parallel to the atomic beam and is controlled by our computer data acquisition system. The final focusing lens (L9) is mounted on a 3-axis translation stage (not shown) to allow precise control of the laser focus.

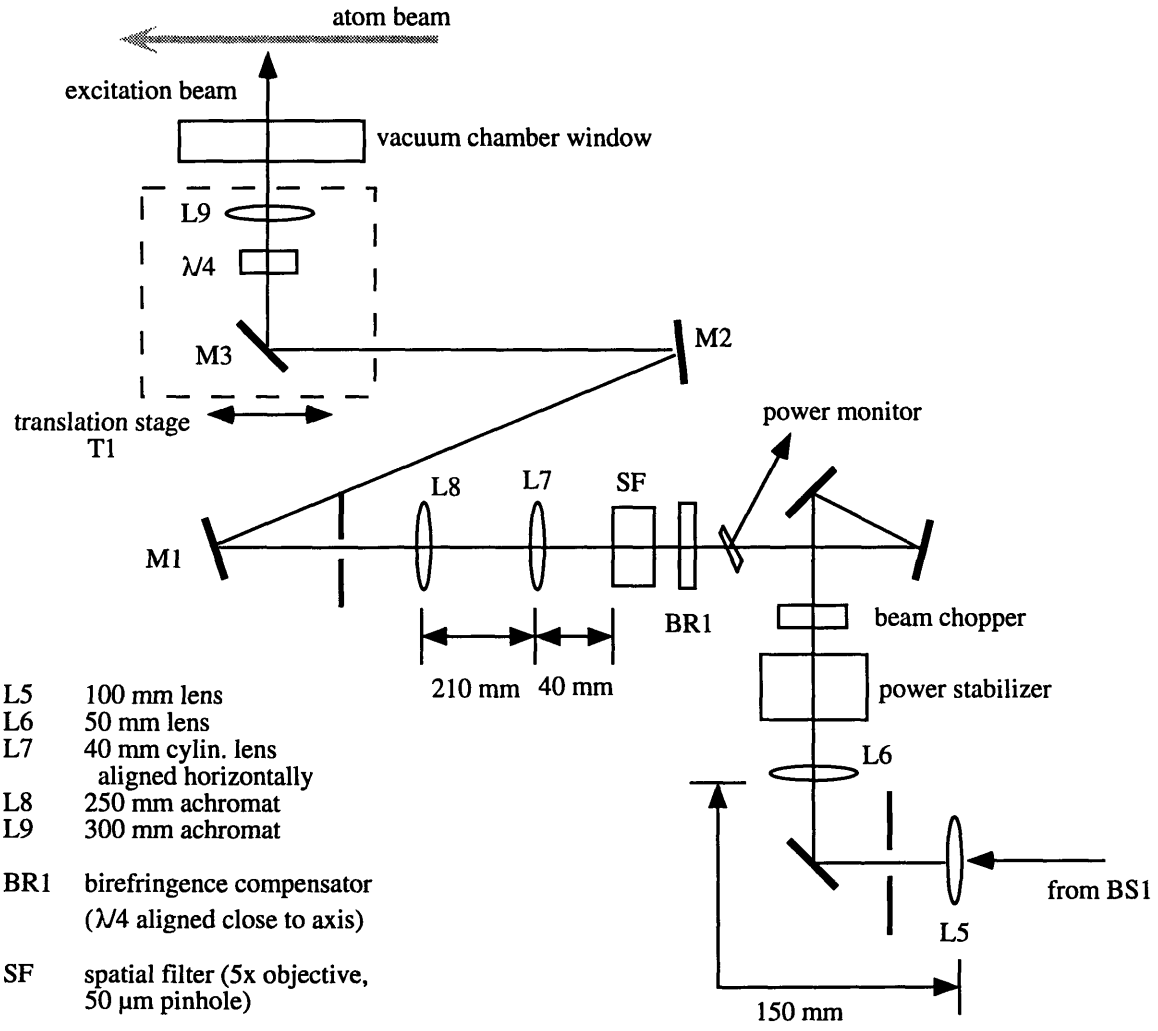

Fig. 2.4.5 Schematic of the optics for the excitation laser beam.

The focus of the entire system (minus the vacuum window) is measured outside of the vacuum chamber by inserting a mirror between the final focusing lens (L9) and the vacuum window to redirect the laser beam to a homemade profilometer. The profilometer consists of a photodiode masked by a 3 μm slit which is scanned across the laser beam profile using a small motorized translation stage oriented perpendicular to the laser propagation axis. The entire assembly itself is mounted on T1 so that the laser profile can be easily measured for different stage locations in order to check the horizontal collimation of the laser beam incident on M3. A typical waist measurement is shown in Fig. 2.4.6.

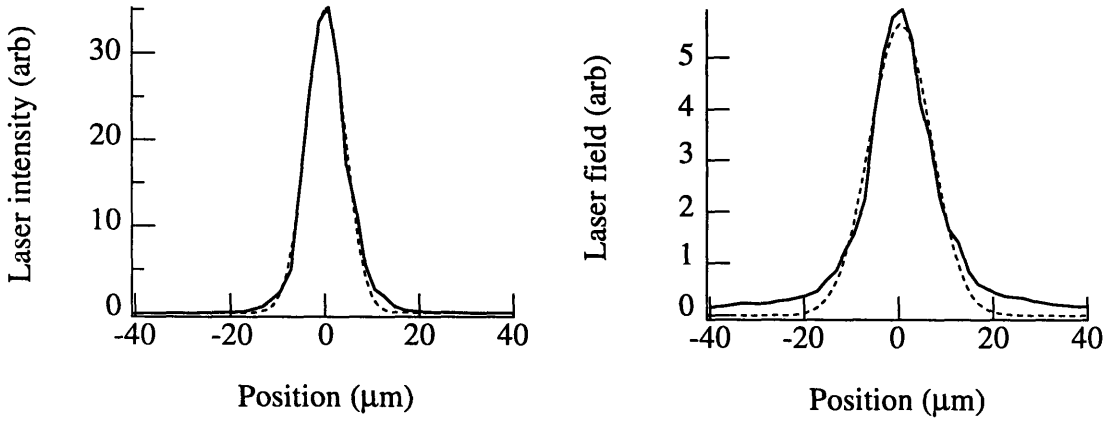

Fig 2.4.6 Measurement of the laser waist (horizontal) using the profilometer. The graph on the left shows the intensity profile, while the graph on the right displays the field profile (square root of the intensity). The solid lines are the measured values and the dashed lines are fits to gaussians. The fits indicate a FWHM of 9 μm for the intensity profile and 15 μm for the field profile.

Polarized Atomic Beam

I will briefly describe our technique for optically pumping the atomic beam. First the atomic beam is setup with only the 2nd collimation slit in place and the optical pumping beam blocked. Using helium carrier gas (beam velocity is ~3000 m/s), the

beam profile in the detector plane (the so-called pinhole image of the source) is ~180 μm wide. The detector wire is moved 300 μm in the positive photon recoil direction from the peak of the pinhole image, corresponding to a 15 $\hbar k$ momentum recoil. When the optical pumping beam is then turned on, the atoms are kicked over into the detector, and the alignment and power of the laser beam are adjusted to maximize the atomic count rate. At this point, the 1st collimation slit is moved into position by translating it to maximize the throughput to the detector. Typical power levels for the optical pumping beam are 15-20 mW. The polarization of the atomic beam is determined by using a 2-wire Stern-Gerlach magnet to measure the state-dependent deflections of the atomic beam. The Stern-Gerlach magnet is located 20 cm after the 1st grating and consists of two 1/8" water-cooled copper conductors 10 cm long in the standard 2-wire configuration [RAM85]. A typical determination of the atom beam polarization using the Stern-Gerlach magnet is shown in Fig. 2.4.7. The atomic polarization is optimized by adjusting the magnetic guide fields and the intensity and polarization of the optical pumping laser beam.

One important advantage in optically pumping on this cycling transition is that the atoms that pass through both slits have necessarily scattered many photons and are likely to become polarized. Furthermore, this procedure minimizes the background due to molecules, because the collimation slits are aligned to pass only the deflected atoms.

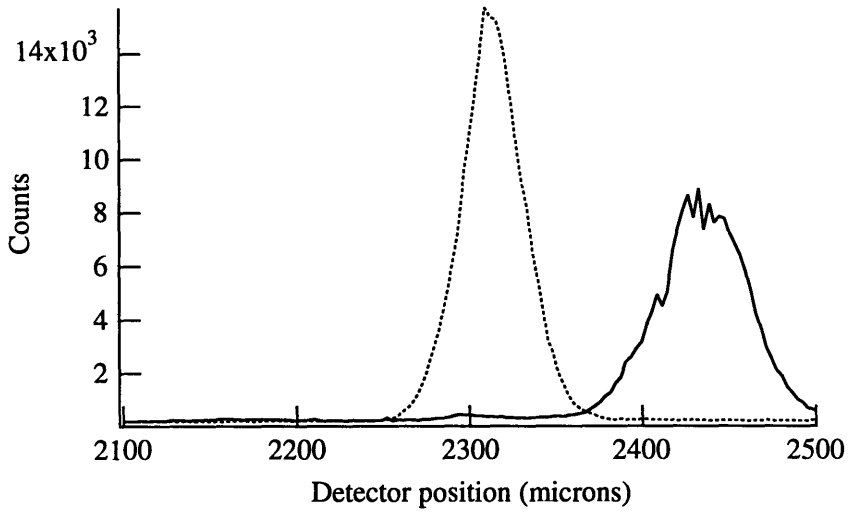

Fig 2.4.7 Using the 2-wire Stern-Gerlach magnet to analyze the optical pumping. The dashed trace is a scan of the collimated optically pumped atomic beam. The solid curve is taken with the Stern-Gerlach magnet on (I = 490 A) from which we can determine that the polarization of the atomic beam is > 95%.

Excitation laser beam alignment

The excitation laser beam has a narrow waist whose depth of focus is only ~150 μm. To align it with the atomic beam, we take advantage of the fact that for moderate laser intensities the number of photons scattered is limited by the transit time of the atoms through the laser beam. Thus adjusting the focus of the laser beam to minimize the number of deflected atoms assures that the atomic beam passes through the laser waist. This is achieved by positioning the detector wire many (~5) photon recoils away from the atomic beam axis and adjusting the position of the final focusing lens (L9) to minimize the atom detector signal.

With a well-aligned focus, the probability for resonant excitation in the two-state system is approximated by the Rabi formula $P(g \rightarrow e) = \sin^2(\omega_R t/2)$, with $\omega_R = 2\pi \cdot 10MHz\sqrt{I/(12mW/cm^2)}$ for the $3P_{3/2}$ transition and I is the (position-dependent) intensity of the excitation laser. To fully excite the atoms, the total laser

power is adjusted to approximately produce a π-pulse (i.e. $\omega_R t = \pi$). This power is empirically determined by measuring atomic deflection from a collimated beam as a function of laser power. The detector wire is displaced from the atomic beam axis by a distance corresponding to a single photon recoil, and we measure the Rabi oscillations in the detector count rate as a function of power. This is shown in Fig. 2.4.8.

Finally, it is important that the excitation laser beam remain in focus and well-aligned with the atomic beam as the point of scattering is varied (i.e. as the translation stage is moved parallel to the atomic beam). This requires first of all that the laser beam incident on the final folding mirror be well-collimated in the horizontal direction. This is verified by measuring the laser focus using the profilometer for different positions of the translation stage as described above. Additionally, it is essential that the motion of the translation stage (T1) and the propagation direction of the laser beam incident on M3 both be parallel to the atomic beam. These alignments are verified by measuring the Rabi oscillations and the alignment of the laser beam and atom beam focus for different stage positions.

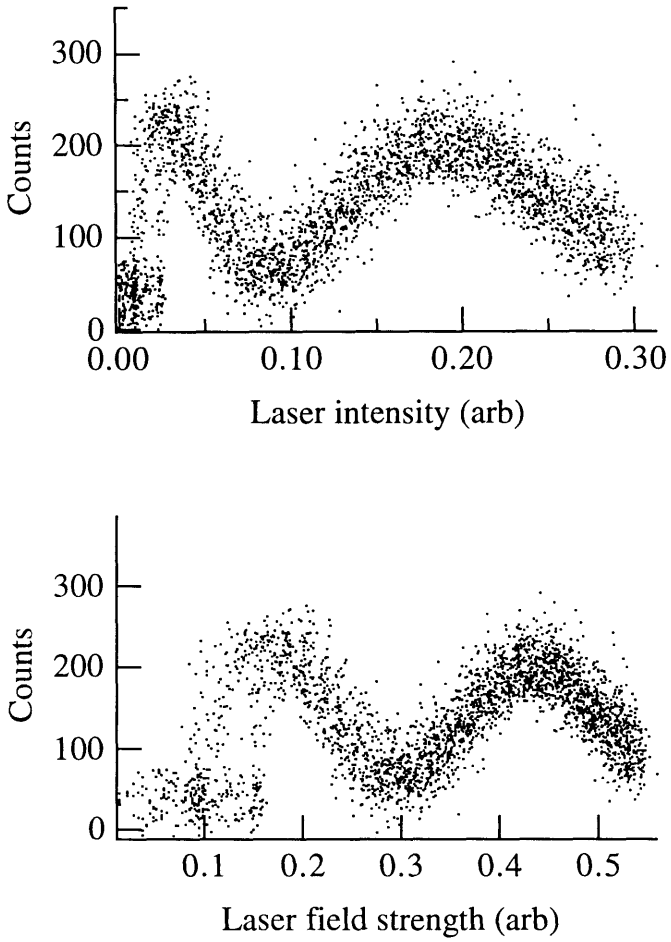

Fig 2.4.8 Using Rabi flops to set the laser intensity. The detector is displaced from the collimation axis one photon recoil, and we measure the count rate as a function of laser intensity (top). As the power increases, the atoms have an oscillatory probability of being excited that is given by the Rabi formula. In the bottom graph the data is plotted versus the laser field strength (square root of the intensity). To scatter a single photon, we set the power to the value at the first maximum of these oscillations, which closely corresponds to a π-pulse.

2.5. Additional Data

In this section, additional data from the correlation experiment will be presented. In these data, the detector position was chosen to accept contributions from more than one interference order (see Fig. 2.3.19 and discussion). These data were taken using a 1st grating with a relatively small open fraction (~30%) and so the 2nd diffracted order from this grating is not negligible. Thus interference contributions from the interference orders involving the terms 2(a5*a6) discussed in Sec 2.3.2 are significant and need be considered.

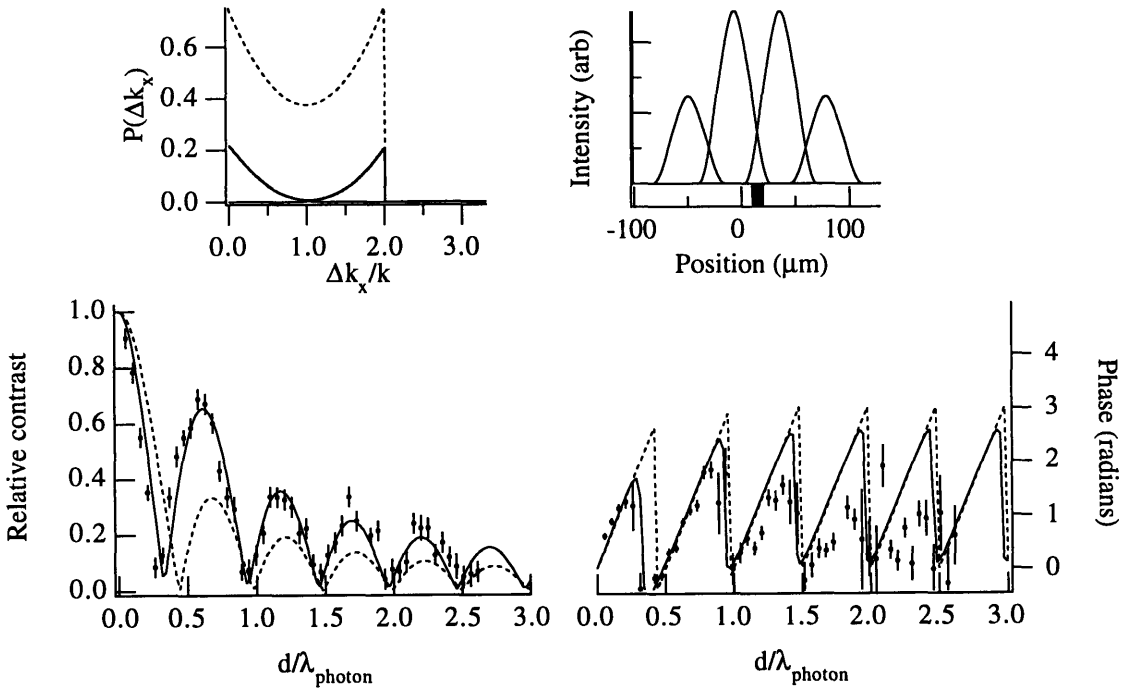

Fig. 2.5.1 Experimental data (solid markers) for the detector centered between the deflected profiles of the 2 central interference orders as shown in the upper right graph. The solid curves in the lower graph are calculated with the modified distribution shown in the upper left graph, and are compared with the original (dashed).

In Fig 2.5.1, results are presented for the case in which the detector (3rd grating) is centered between the deflected profiles of the two principle interference orders. This case is very similar to that calculated in Fig. 2.3.19. As predicted by the calculation, the contrast shows striking revivals—the first revival is twice as high as for the uncorrelated case. The agreement with the calculation is quite good for the contrast data. For the phase data, the agreement is very good up until $d = \lambda$, and less satisfactory thereafter. The data indicate that the beam velocity here (and in the subsequent figures in this section) was 15% lower than usual which may be due to a lower carrier gas pressure used to maximize the atomic flux (see Chap 4.).

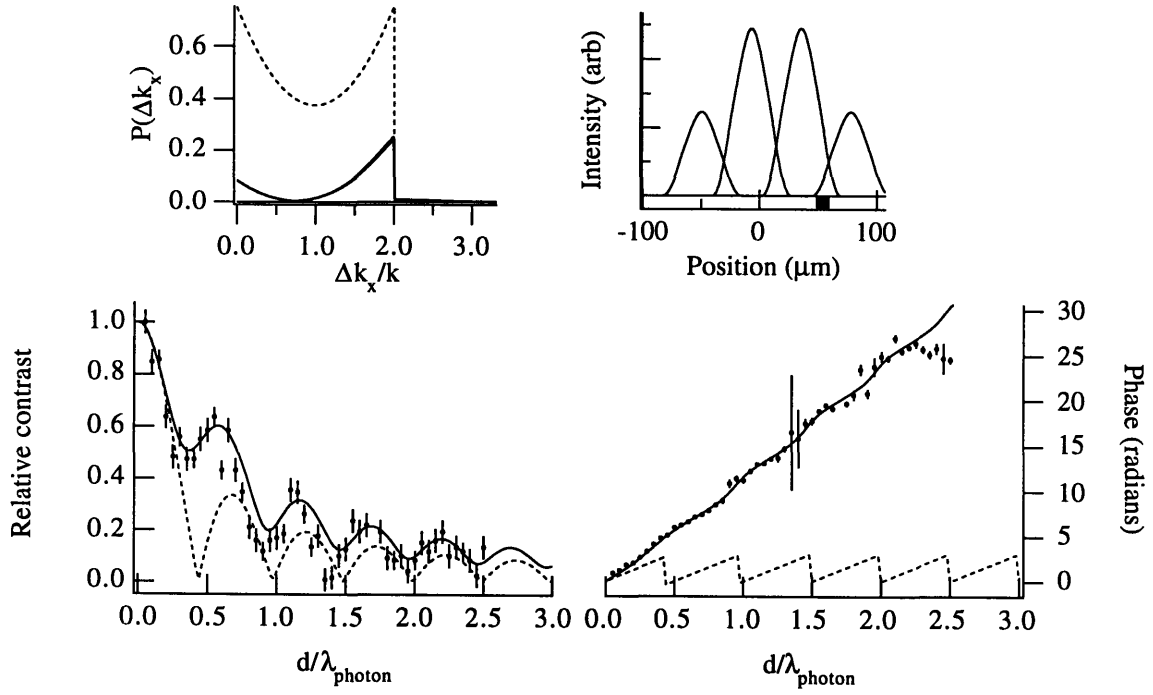

Fig 2.5.2 Experimental data (solid markers) for the detector centered between the deflected profiles of the 2 rightmost interference orders as shown in the upper right graph. The solid curves in the lower graph are calculated with the modified distribution shown in the upper left graph, and are compared with the uncorrelated case (dashed).

In Fig. 2.5.2, the detector was located between the two rightmost interference orders. The deflected profiles in the upper right graph indicate the relative strength of the *interference* signal (that is their relative weight is (a5*a6)/(a1*a2)). Because of the different relative strengths, the distribution $P'(\Delta k_x)$ is skewed towards $\Delta k_x = 2k$ even though the detector is centered between the two interferometers. The skew of $P'(\Delta k_x)$ favors the backward scattering events and determines the phase shift of the interference pattern. The contrasts shows modulation, but because of the skew of the distribution, the cancellation between the $\Delta k_x = 0k$ and $\Delta k_x = 2k$ contributions is not perfect and the contrast does not fall to zero near $d = \lambda / 2$ as in Fig. 2.5.1.

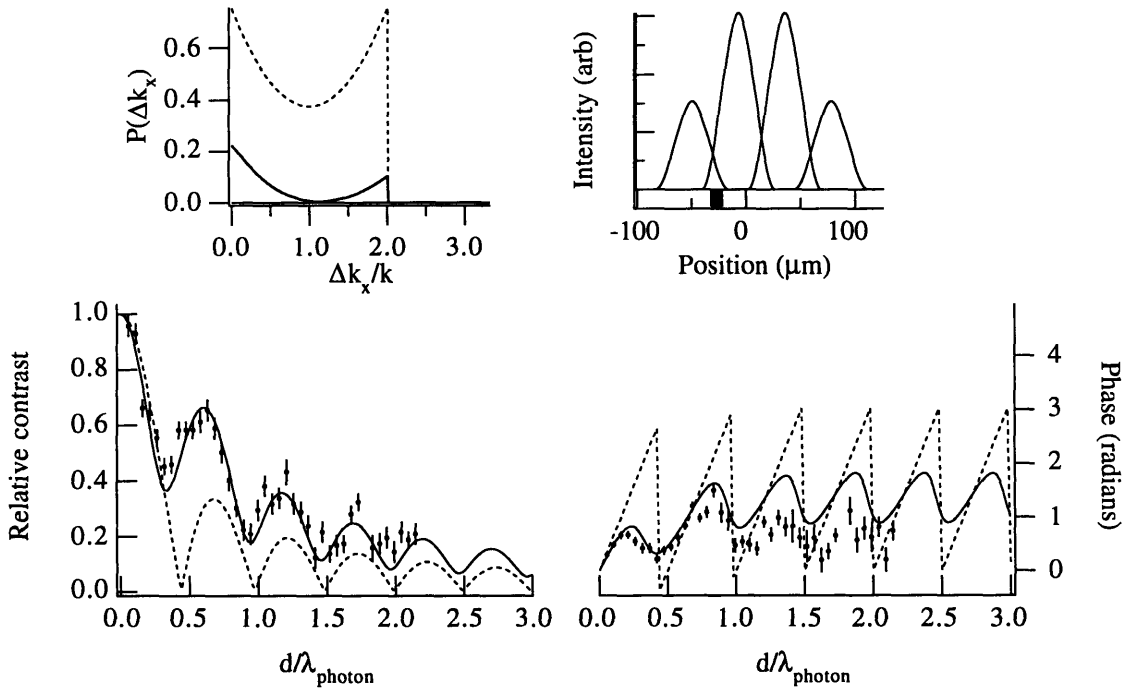

Fig 2.5.3 Experimental data (solid markers) for the detector centered between the deflected profiles of the 2 rightmost interference orders as shown in the upper right graph. The solid curves in the lower graph are calculated with the modified distribution shown in the upper left graph, and are compared with the original (dashed).

In Fig 2.5.3, the detector is now located between the leftmost interference orders, and the situation is very similar to the case in Fig 2.5.2 except that the skew is in the other direction. This is reflected in the phase data, which are now dominated by the $\Delta k_x = 0k$ contributions.

2.6. Discussion

Relation to other experimental work

Photon scattering has been used to completely destroy atomic interference to suppress one of the recoil components in 4-zone Ramsey-Bordé interferometers [RWK92], [SSM92]. Photon scattering has also been used to completely destroy atomic interference in a Lau interferometer [CLL94]. Additionally, we have used photon scattering to destroy atomic interference in our work in molecular interferometry described in the next chapter. In all these cases, the scattering occurred at large separation of the interfering atomic wavefunctions and completely destroyed the interference—no attempt was made to study the loss of interference as a function of the separation.

Recently, Pfau et al [PSK94] have measured the effects of a single spontaneous emission on the transverse momentum distribution of an atomic beam. Their measurement can be understood from Fig. 2.3.14. In shown in this figure, the initial transverse momentum distribution of the beam is modified by the photon scattering. Of course if we deconvolve the momentum transfer due to the photon scattering from the initial momentum distribution we will end up where we started, namely with the distribution of transverse momentum recoil $P(\Delta k_x)$. By measuring this distribution, they inferred the effects on the spatial coherence of the beam using the van Cittert-Zernike theorem of classical optics [BOW80], which relates the Fourier transform of the momentum distribution of the beam to the spatial coherence of the source (see also [CBA91]). In fact, their experiment used a standing light wave grating of variable period, although measuring the profiles of a well-collimated beam as depicted in Fig. 2.3.14 would be entirely equivalent.

Relation to 2-slit *gedanken* experiment

The original Feynman's light microscope *gedanken* experiment with electrons [FLS65] and the atom versions discussed more recently [SCP91], [TAW93] were discussed in terms of the Young's two-slit experiment with the photon scattering occurring close to the slits. In these *gedanken* experiments, the loss of fringe contrast is parameterized by d / λ_{photon} where d is now the slit separation instead of the spatial displacement of the wavefunctions as in our case. Except for this difference, the theory for these experiments predicts the same results for the loss of contrast and phase shift of the fringes.

However, if there is not a notable difference in the theoretical results, there is in the physical explanation of the loss of contrast. In the two-slit version of the experiment, the phase shift of the interference pattern $\Delta\phi$ is the same as the classical deflection of the atom Δx (more precisely $\Delta\phi = 2\pi\Delta x / p$ where p is the period of the fringes at the detector plane). Hence the loss of interference is often explained as a "washing out" of the fringes due to the deflection of the fringes produced by the momentum kicks of the photons. In our experiment Δx is clearly distinct from $\Delta\phi$ and much larger, but, more importantly, only weakly dependent on d. Hence the loss of interference cannot be simply understood as the results of the "deflection" of the fringes—indeed, the deflections Δx in our case are largest for scattering at—or before—the 1st grating where the effects on the atomic interference is smallest. In fact, it is precisely because Δx is much larger than $\Delta\phi$ in our experiment and only weakly dependent on d that we can recover the interference in our correlation experiment.

Using a gradient field to recover the contrast

The correlation experiment is based on the "spatial filtering" of the atoms as a function of the momentum transferred to the atoms by the scattered photon. By this we mean that the lateral position of the atom at the third grating is correlated with the direction of the scattered photon. Instead of using a small acceptance detector to select a subset of the atoms as we did in the correlation experiment, we can use the spatial filtering to actually reverse (partially) the effects of the photon scattering. For this experiment, we need to fully isolate the two interfering beams at the *2nd* grating with a physical barrier as in our atomic polarizability experiment [ESC95]. We scatter single photons from the atoms to reduce the atomic fringe contrast just as before. Now, we apply a transverse linear gradient potential to *one* of the beams (shown in Fig. 2.6.1). To the extent that the atoms are spatially filtered at location of the applied potential, the strength of the potential can be chosen to cancel the gradient phase associated with the photon scattering. The extent of this reversal will depend on the initial transverse momentum spread of the atomic beam compared with the photon momentum transfer.

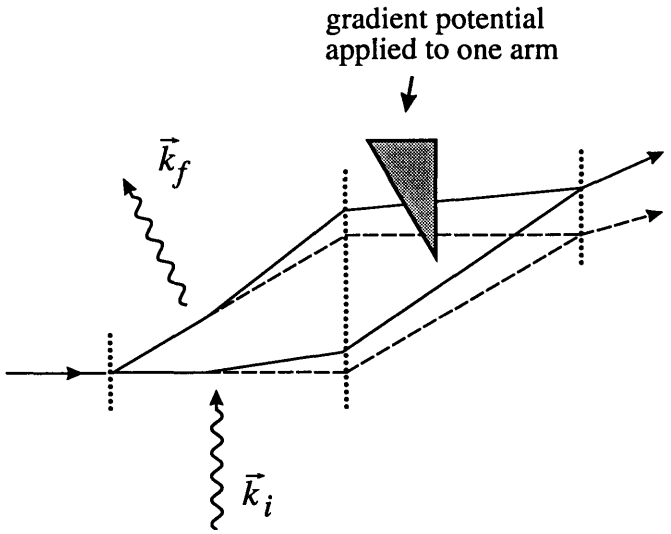

Fig. 2.6.1 Using a gradient potential interaction applied to one arm of the interferometer to reverse the effects of the photon scattering.

A simple optical analog to our experiment

In Sec. 2.3.1, we discussed how the atom-photon interaction (when the scattered photon is measured) imparts a linear varying phase to the atom wavefunction which is analogous to the effects of an applied linear gradient field. This analogy suggested a optical analog to our experiment, which we will briefly describe. First we constructed a very simple three grating interferometer using a He-Ne laser as the light source and binary amplitude transmission gratings with a period of 175 μm. Remarkably, we made quite adequate gratings using a only laser printer and a photocopying machine. The laser printer is used to print out an array of 200 lines with a spacing of 1 mm. This original is then successively reduced four times at 0.64% reduction using the photocopying machine, with the final copy being made on a sheet of transparency.

Three of these gratings spaced ~40 cm apart are used to make an laser interferometer analogous to our atom interferometer. To simulate the effects of the atom-photon interaction, a wedged piece of glass is placed after the 1st grating. Just as for in the atom-photon case, the wedge imparts a relative phase shift between the two arms of the interferometer that depends both on the separation of the arms and on the orientation of the wedge. The wedge is mounted in a bearing and is rotated using a small electric motor. When the wedge is situated just after the first grating, the contrast of the interferometer is unaffected, but as the position of the wedge is translated further downstream, one can observe both the loss and subsequent revival of the contrast just as in our experiment. The rotating wedge is completely analogous to the case of isotropic scattering without the initial momentum transfer as discussed in Fig. 2.3.4, and indeed the π phase shift between successive revivals can be observed.

3. Molecular Interferometry

3.1. Introduction

In this chapter, I will discuss our demonstration of a molecular interferometer operating exclusively in the Hilbert space of the external molecular coordinates. We were able to fully spatially isolate the two paths of the interferometer (as we have done with our atom interferometer) and introduce a neon gas cell into one path to measure the index of refraction of neon for the molecule waves. This experimental work should, on the one hand, pave the way for interferometry with more and more complex molecules and clusters and, on the other hand, lead to the use of matter-wave interferometry techniques in the fields of molecular and chemical physics. An example of the former would be a study of environmentally induced decoherence as the system (particle) size is varied, and an example of the latter would be measuring the tensor components of the electric polarizability of different molecules. Additionally, a grating interferometer with heavy molecules could provide a very sensitive inertial sensor (for a grating interferometer with a thermal beam, the sensitivity to accelerations increases in proportion to the particle mass, and for rotations, it increases like the square root of the mass).

The historical trend in interferometry is generally towards larger mass particles and shorter wavelengths (see Fig. 3.1). More importantly perhaps, the system complexity, or the number and density of internal energy states, has also continued to increase. One of the important areas of research in matter-wave interferometry will be the exploration of the limits, either fundamental or practical, to interferences of larger and larger particles.

A grating-based interferometer such as ours is a natural tool for this investigation, because the gratings are not specific to particular atomic or molecular species as is the case for interferometers based on entangled internal and external states [BCB94].

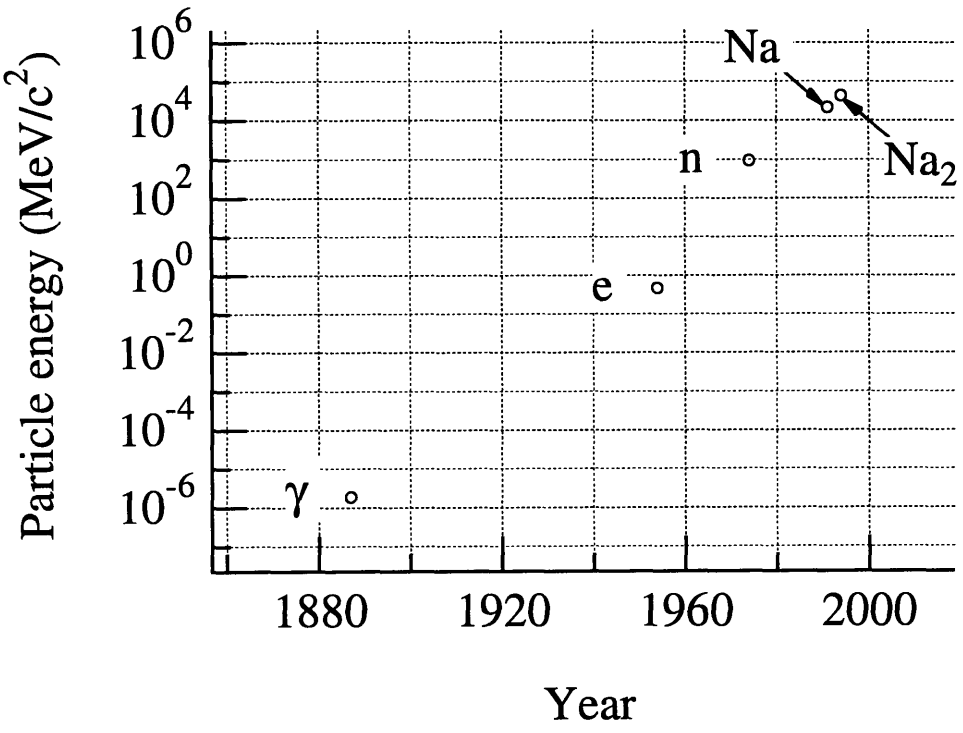

Fig. 3.1 The historical trend showing the increase in particle energy $E = \sqrt{p^2c^2 + m^2c^4}$ in separated beam interferometers. Except for the case of the photon interferometer, the energy is dominated by the rest mass of the particle. The plotted points are for the Michelson-Morley light interferometer [MIM87], the electron bi-prism [MOD54], neutron single crystal interferometer [RTB74], and our atom and molecule separated beam interferometers.

Indeed, much of our work in developing this interferometer was in the development of a high flux molecular beam, which we accomplished by using radiation pressure to selectively remove atoms and isolate the molecules in a mixed atom-molecule beam. The

molecule used for this study was the sodium dimer, Na_2, chosen primarily because of its natural formation in our type of source. It also has additional advantages that are discussed in the following paper on this work to appear in Physical Review Letters.

3.2. Optics and Interferometry with Na_2 Molecules (to appear in Phys. Rev. Lett.)

Michael S. Chapman [1], Christopher R. Ekstrom[1], Troy D. Hammond [1], Richard A. Rubenstein [1], Jörg Schmiedmayer [1,2], Stefan Wehinger [1,2] and David E. Pritchard [1]

[1] *Department of Physics and Research Laboratory of Electronics*
Massachusetts Institute of Technology, Cambridge, Massachusetts 02139, USA.

[2] *Institut für Experimentalphysik, Universität Innsbruck, A-6020 Innsbruck, Austria*

We have produced an intense, pure beam of sodium molecules (Na_2) by using light forces to separate the atomic and molecular species in a seeded supersonic beam. We used diffraction from a micro-fabricated grating to study the atomic and molecular sodium in the beam. Using three of these gratings, we constructed a molecule interferometer with fully separated beams and high contrast fringes. We measured both the real and imaginary parts of the index of refraction of neon gas for Na_2 molecule deBroglie waves by inserting a gas cell in one arm of the interferometer.

PACS numbers: 3.75.-b, 34.20.Gj, 07.77.Gx,

Quantum mechanical treatment of the center of mass motion of increasingly complex systems is an important theme in modern physics. This issue is manifest theoretically in studies of the transition from quantum through mesoscopic to classical regimes and experimentally in efforts to coherently control and manipulate the external spatial coordinates of complex systems (e.g. matter wave optics and interferometry). Recently, matter wave optics and interferometry have been extended to atoms with the many techniques for the coherent manipulation of the external degrees of freedom of atoms constituting a new field called atom optics [1]. The present work extends and develops techniques of atom optics into the domain of molecules---systems characterized by many degenerate and non-degenerate internal quantum states. Whereas internal state coherences in complex molecules have long been cleverly manipulated in spectroscopy in both the radio [2] and optical frequency domains [3,4], here we coherently manipulate exclusively the center of mass motion [5]. This work, which culminates in the use of a molecule interferometer with spatially separated beams to determine hitherto unmeasureable molecular properties, demonstrates the applicability of molecular interferometers to precision measurements in molecular physics, some of which may have applications to fundamental physics experiments using specific molecules [6].

Our experiment combines several techniques from atom optics to make and use a molecule interferometer whose paths are well separated in position and momentum. Using an incident supersonic beam containing both Na atoms and dimers (Na_2), we apply resonant light forces to selectively remove the Na atoms, leaving a pure Na_2 beam. We then use nanofabricated diffraction gratings, first to study the characteristics of the molecular beam and subsequently as coherent beam splitters to make a molecule interferometer with high contrast fringes. Finally, we insert a gas cell in one path of the separated beam interferometer and measure the complex index of refraction for Na_2

deBroglie waves in Ne gas. This provides new information on the long range part of the Na_2-Ne potential.

The beam of sodium atoms and dimers was produced in a seeded supersonic expansion using either argon or krypton as the carrier gas. By heating the Na reservoir to 800°C (Na vapor pressure ~300 torr), we were able to enhance the population of sodium dimers in the beam to as much as 30% of the detected beam intensity [7]. At a carrier gas pressure of 2000 torr with a 70 μm nozzle aperture, we produced a cold Na_2 beam with only 3.5% rms longitudinal velocity spread, corresponding to a (longitudinal) translational temperature of 2K.

To create a pure molecular beam, we used resonant light pressure forces acting on the atoms to deflect them sideways out of the collimated beam (Fig. 1). The deflecting laser beam was produced with a dye laser (Coherent 599) tuned to the F=2 $\rightarrow$ F'=3 transition of the D_2 line in Na (589.0 nm). The frequency was maintained at the Doppler free resonance by servoing the laser frequency to keep a fluorescent spot centered in the spreading atomic beam before the first collimating slit [8]. An electro-optic modulator was used to generate frequency sidebands at an offset of 1.713 GHz to deflect atoms in the F=1 hyperfine state. The laser light was applied at a position centered between two 20 μm collimating slits separated by 85 cm. With this geometry, $\sim 3\hbar k$ of transverse momentum transfer is required to deflect the atoms out of the beam. A knife edge was positioned directly upstream from the laser beam to prevent any atoms that would normally miss the second collimation slit from being deflected back into the molecular beam. The molecules are not resonant with the deflecting laser beam and are therefore unaffected. (The $X^1\Sigma_g^+ \rightarrow A^1\Sigma_u^+$ transition to the first excited dimer state is strongest around 680 nm [9]).

We investigated molecular diffraction with 100, 140, and 200 nm period microfabricated diffraction gratings. Since the sodium atoms and molecules coming from the supersonic expansion have nearly the same velocity [10], their momenta and hence their deBroglie wavelengths differ by a factor of two because of their mass difference. For a source temperature of 770°C and Kr carrier gas, $\lambda_{dB}(\mathrm{Na}) = 0.21\,\mathring{\mathrm{A}}$ and $\lambda_{dB}(\mathrm{Na_2}) = 0.11\,\mathring{\mathrm{A}}$. A diffraction pattern obtained with a 100 nm grating and the mixed Na-Na_2 beam (deflecting laser off) is shown in Fig. 2a. The various diffracted orders of the sodium atoms are sufficiently separated to permit easy identification of the intermediate molecular diffraction peaks at half the diffraction angle of the atoms. When the atoms are removed from the beam (Fig. 2b, deflecting beam on), we resolve the molecular diffraction out to the 4th order. From a comparison of Fig. 2a and Fig. 2b we can determine that our Na_2 beam contains less than 2% residual atoms.

These diffraction patterns provide us with a powerful tool for analyzing the atoms and molecules in the expansion. We determined the mean fraction of molecules and the center and width of the velocity distributions for both atoms and dimers from these diffraction patterns. We observed as much as a 3.5(6)% velocity slip between the atoms and slower moving molecules at low source pressures (400 torr) [10]. At a typical source pressure of 1500 torr the slip was less than 1%. Using diffraction to investigate molecular beams has the advantage of being non-destructive and therefore applicable to very weakly bound systems such as He_n molecules or other van der Waals clusters. Indeed, our method and our gratings have recently been used to produce unequivocal evidence of the existence of He_2 molecules [11].

We have employed three 200 nm fabricated gratings to construct a Mach-Zender interferometer for molecules (Fig. 3), similar to our atom interferometer [12]. This configuration produces high contrast fringes with our pure Na_2 molecular beam (inset Fig. 4). For both the mixed interferometer (atoms + molecules) and the pure molecule

interferometer, the maximum observed contrast $(I_{max} - I_{min})/(I_{max} + I_{min})$ was nearly 30%.

The period and phase of the molecular interference pattern is the same as would be observed for atoms, even though the molecules traverse the interferometer on different paths than the atoms (Fig. 3). This is because the three grating geometry produces a white light interference pattern [13] whose period and phase are independent of the deBroglie wavelength of the particle. Therefore, in addition to using the previously described laser deflection scheme to produce a pure beam of Na_2, we used two other methods to verify that the observed interference is from molecules: we introduced a (decoherence) laser which destroys the atomic interference by scattering resonant light from the split atomic wave function inside the interferometer, and we checked that the interference signal $(I_{max} - I_{min})/2$ varied as expected with the transverse position of the third grating.

The results from a study combining both methods are shown in Fig. 4. For each third grating position, we observe the largest interference signal from the combined atom and molecule fringe pattern (both lasers off). With either the deflection or decoherence laser beam on, the interference signal is reduced the same amount, indicating that only molecules contribute to the interference. This interpretation is confirmed because the interference signal does not decrease further when both lasers are on simultaneously.

The measured variation of the interference signal as a function of third grating position is compared with curves calculated by convolving the beam profiles with the detector acceptance. The atom or molecule interference fringes at the third grating have a trapezoidal spatial envelope with a width determined by the collimating slits [2] and an offset from the collimation axis determined by the diffraction angle (different for atoms and molecules) and the distance between the gratings (Fig. 3). In addition to the

interfering paths shown in Fig. 3, there are also interfering paths symmetric to the collimation axis as well as (small) contributions at larger offsets from the third grating involving the 1st and 2nd order diffraction from the first grating. Thus, the detected interference signal is a convolution of the spatial envelope(s) of the interference signal with the acceptance of the detector, which is determined by the 50 μm width of the third grating and its lateral position. We observe a peak in interference signal for the predominately atomic beam at ~50 μm from the collimation axis, as expected from the diffraction angle for Ar carrier gas v_{beam} = 1000 m/s. A similar peak is not resolved in the Na_2 signal because of the smaller diffraction angle. The upper curve is normalized to the maximum observed interference signal and the lower curve is predicted from the known fraction of molecules (27%) (i.e. it is not independently normalized).

We observed no degradation in molecular interference signal despite the plethora of close lying ro-vibrational states in the molecules. This is not entirely surprising. The fact that two nearby molecules are very unlikely to have the same quantum numbers for both ro-vibrational state and total angular momentum projection is not important since the first order interference observed in an interferometer involves only the interference of each particle with itself. Although the 300K thermal background photon energies typically exceed the internal level spacing of molecules (~1 cm^{-1} for rotations and ~100 cm^{-1} for vibrations), decoherence effects due to transitions between vibrational or rotational levels or spontaneous emission are minimized because electric dipole transitions between ro-vibrational levels in the same electronic state are not allowed in a homonuclear diatomic molecule [9]. Scattering of the molecules on the micro fabricated diffraction gratings could also cause rotational or vibrational transitions, since a beam velocity of 1000 m/s and a grating *thickness* of 200 nm produces Fourier components up to 5 GHz (or 0.17 cm^{-1}). However, this is less than the smallest rotational splitting 2B (B is the rotational constant) of 0.31 cm^{-1} and much smaller than the vibrational spacing of

159 cm^{-1}. As expected, we did not observe any contrast reduction, indicating an absence of these transitions.

Using Kr as the carrier gas, our Na_2 interferometer produces a molecular beam separation of 38 μm at the second grating. This just exceeds the beam width at that position and allows insertion of an interaction region with a thin mylar barrier between the interfering beams. The foil casts a shadow 20 μm wide, which partially blocks the edges of the two beams, reducing the contrast from 19% without the foil to 7% with the foil. The lower observed contrast with krypton as the carrier gas (even without the inserted foil) is attributed to the slower beam velocity which enhances the inertial sensitivity of the interferometer, making it more vulnerable to vibrations of the apparatus. A similar contrast reduction is observed with atoms.

We have used this separated beam molecule interferometer to measure the ratio of the real to imaginary parts of the index of refraction for the Na_2 deBroglie waves passing through a Ne gas cell in one path of the interferometer, as we have done with atoms [14]. In analogy to light optics, the wave propagation through the gas cell of length L is modified by the factor $\exp[i(n-1)k_{lab}L]$, where the index of refraction $n-1=2\pi N f(k,0)/k_{lab}k$ is characterized by the complex forward scattering amplitude $f(k,0)$, the number density N of the Ne gas and the wave-vector in both the lab (k_{lab}) and center of mass (k) frame of the collision. By measuring both the phase shift and attenuation of the interferometer for different target densities, we have measured the ratio $\mathrm{Re}[f(k,0)]/\mathrm{Im}[f(k,0)]=1.4(3)$ for Na_2 scattering from Ne. The corresponding value for atomic Na waves passing through Ne is 0.98(2), a value considerably in excess of the 0.72 expected for a pure C_6/R^6 potential [14]. We have separately measured the total absorption of Na_2 by Ne (i.e. $\frac{4\pi}{k}\mathrm{Im}[f(k,0)]$) to be 57(2)% larger than the corresponding absorption of Na, whereas a 32% increase would expected for a pure C_6/R^6 potential if C_6 for Na_2-Ne were twice that for Na-Ne. Our measurements are in qualitative

agreement with Na-Ne potentials from [15] if extended to Na_2 using combination rules from [16]. More detailed studies will allow us to investigate how the long range interactions for combined systems can be predicted from the simple systems.

In conclusion, we have demonstrated the production and diffraction of an intense beam of sodium dimers. We find that the diffraction of a seeded supersonic sodium beam by a transmission grating can serve as a sensitive intrinsically nondestructive probe of the constituents of an atomic beam. Further, we built a three grating interferometer for molecules and observed no degradation in interference signal compared with atoms. We then spatially isolated the two interfering molecular beams and measured the index of refraction of neon gas as seen by the molecular matter waves.

This work opens up the field of molecular optics and molecular interferometry with new possibilities of making fundamental and precision experiments on molecules similar to the ones recently conducted in atom interferometry. Separated beam molecule interferometry provides a new way to study interactions of the molecular ground states. For example, these techniques could be used to investigate the electric polarizability of diatomic molecules [17]. By measuring the phase shift and contrast as a function of applied electric field one could determine both the parallel and perpendicular (to the molecular axis) polarizabilities. This experimental technique may also be used to measure the interaction of a polar molecule with the background electromagnetic field to investigate decoherence of external degrees of freedom caused by the interaction with a thermal bath.

We would like to acknowledge the technical contributions of Bridget Tannian, and help with this manuscript from Alan Lenef. The atom gratings used in this work were made in collaboration with Mike Rooks at the National Nanofabrication Facility at Cornell University. This work was supported by the Army Research Office contracts

DAAL03-89-K-0082, and DAAL03-92-G-0197, the Office of Naval Research contract N00014-89-J-1207, and the Joint Services Electronics Program contract DAAL03-89-C-0001. J.S acknowledges the support of the Austrian Academy of Sciences, and T. H. acknowledges the support of the National Science Foundation.

References

1. For an overview of the field, see the following special issues and review articles: J. Opt. Soc. Am. B **6**, (1989), Appl. Phys. B **54**, (1992), J. de Physique **4**, (1994), C.S. Adams, M. Sigel and J. Mlynek, Phys. Rep. **240**, 143 (1994), "Fundamental Systems in Quantum Optics" App. Phys. B to appear in 1995.

2. N.F. Ramsey. *Molecular Beams* (Oxford University Press, Oxford, 1985)115-139

3. V.P. Chebotayev, J. Opt. Soc. Am B **2**, 1791-1798 (1985)

4. C.J. Bordé, N. Courtier, F.d. Burck, A.N. Goncharov and M. Gorlicki, Phys. Lett. A **188**, 187 (1994)

5. As Bordé has pointed out, many laser spectroscopy experiments on molecules may be regarded as interferometers because the components of the molecules wavefunction in different internal states travel on slightly different spatial paths. See C.J. Bordé, Phys. Lett. A **140**, 10 (1989)

6. P.G.H. Sandars, Phys. Rev. Lett. **19**, 1396 (1967)

7. Measurements by D.D. Parrish and R.R. Herm, J. Chem. Phys. **51**, 5467 (1969) carried out on Li_2 indicate that it is possible that the hot wire detector we use detects two counts for every molecule.

8. P. Gould. Ph.D. Thesis, Massachussets Institute of Technology, 1985 (unpublished).

9. G. Herzberg. *Spectra of Diatomic Molecules* (D. vs Nostrand, Princeton, 1950)

10. G. Scoles. *Atomic and Molecular Beam Methods* (Oxford University Press, New York, 1988).

11. W. Schöllkopf and J.P. Toennies, Science **266**, 1345 (1994)

12. D.W. Keith, C.R. Ekstrom, Q.A. Turchette and D.E. Pritchard, Phys. Rev. Lett. **66**, 2693 (1991)

13. J. Schmiedmayer, C.R. Ekstrom, M.S. Chapman, T.D. Hammond and D.E. Pritchard. in *Fundamentals of Quantum Optics III* , p. 21, edited by F. Ehlotzky (Springer-Verlag, K\"{u}thai, Austria, 1993).

14. J. Schmiedmayer, M.S. Chapman, C.R. Ekstrom, T.D. Hammond, S. Wehinger and D.E. Pritchard, Phys. Rev. Lett. **74**, 1043 (1995)

15. P. Barwig, U. Buck, E.Hundhausen and H. Pauly, Z. fur Physik **196**, 343 (1966); R.A. Gottscho et al., J. Chem. Phys. **75**, 2546 (1981).

16. K.T. Tang and J.P. Toennies, Z. f. Phys D **1**, 91 (1986)

17. T.M. Miller and B. Bederson. in *Advances in Atomic and Molecular Physics* , 13, p. 1-55, edited by (Academic Press, 1978).

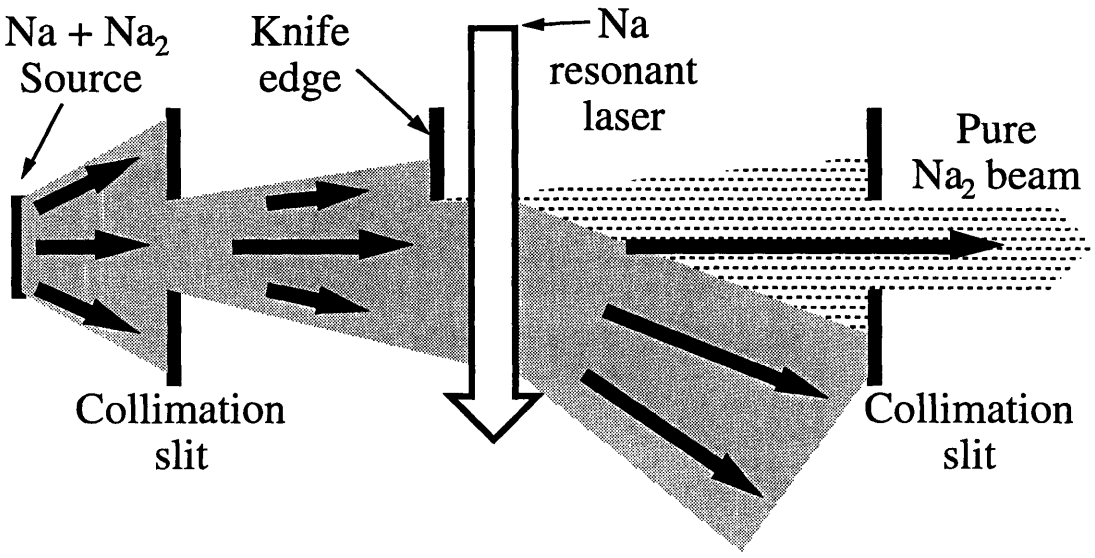

Figure 1: Removal of the sodium atoms from the beam. The deflecting laser imparts a transverse momentum to the sodium atoms, deflecting them away from the second collimation slit.

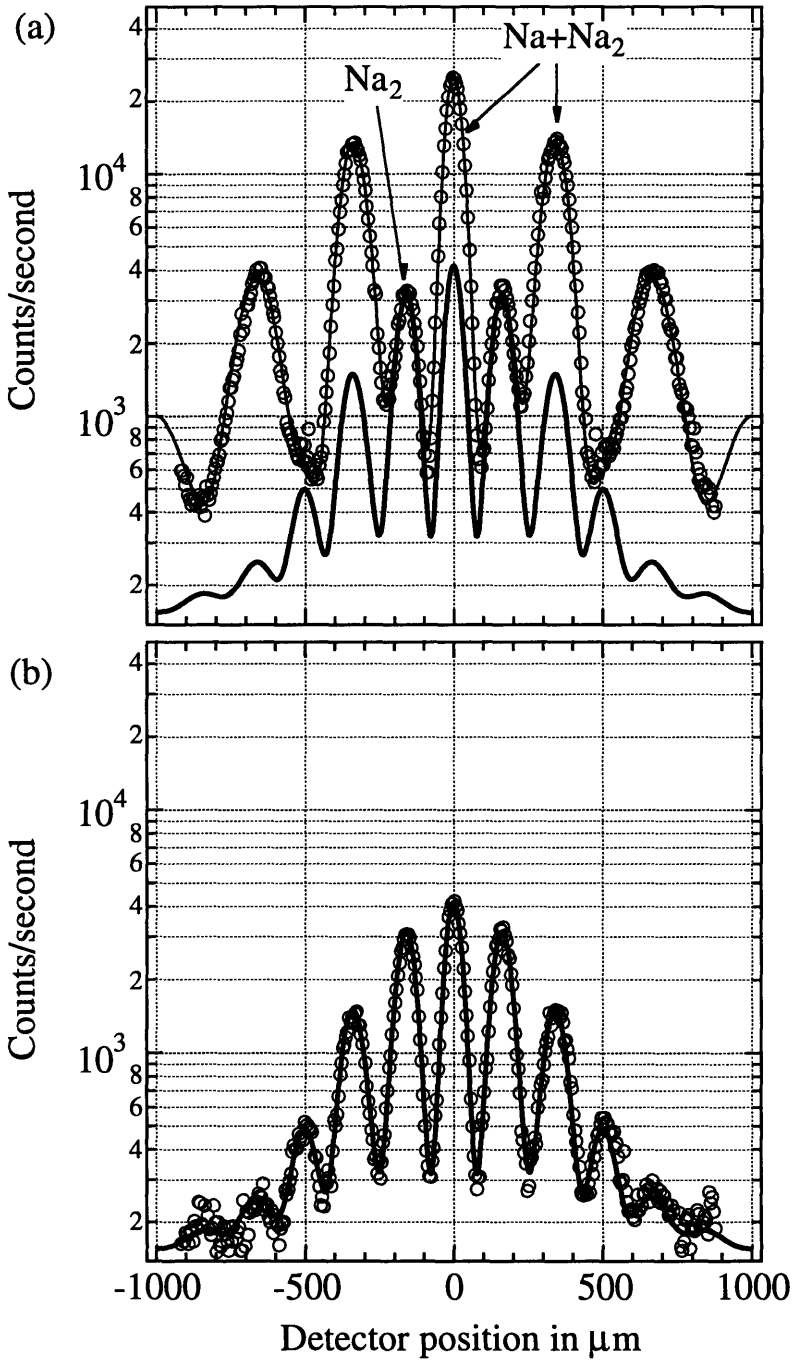

Figure 2: (a) Diffraction of the mixed atom-molecule beam (deflecting beam off) and (b) molecule beam (deflecting beam on) by a 100 nm period grating. The thin solid line in (a) is a fit to the diffraction pattern indicating that 16.5% of the detected intensity is molecules. The thick solid line in both graphs is the fit to the Na_2 diffraction pattern in (b). Both fits are for a diffraction grating with 30% open fraction and a beam velocity of 820 m/s (Kr as a carrier gas).

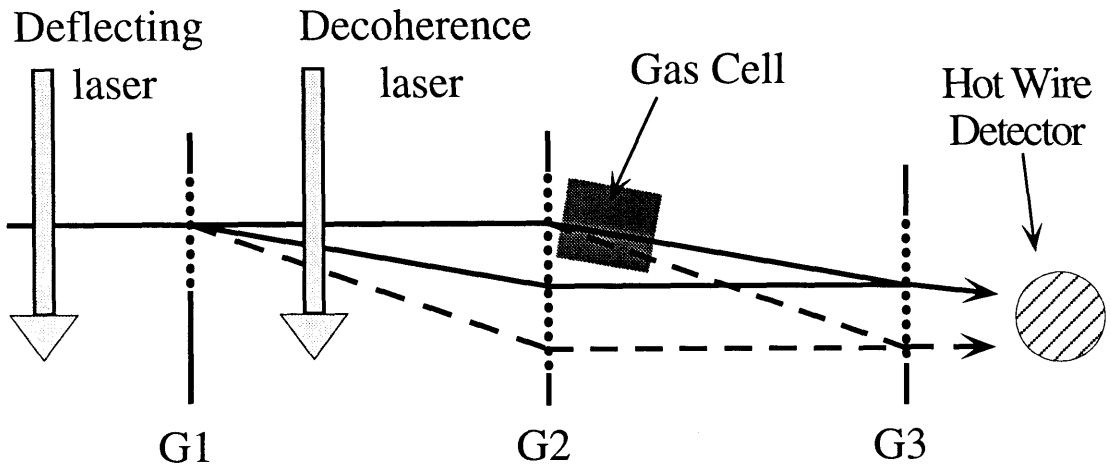

Figure 3: Schematic of our interferometer showing the paths of Na (dashed line) and Na_2 (solid line). G1, G2, and G3 indicate the three diffraction gratings.

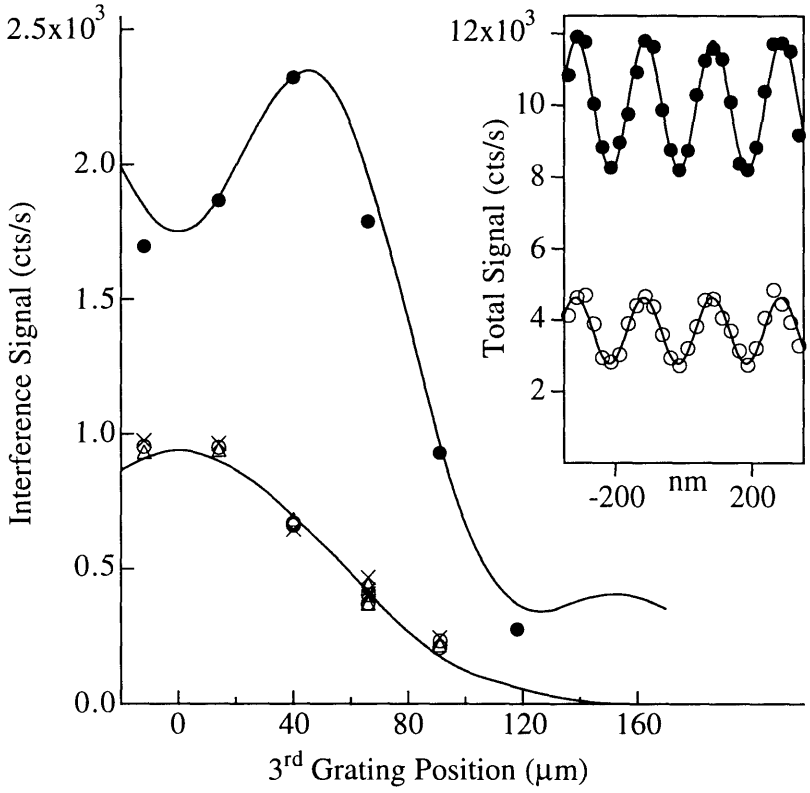

Figure 4: The variation of the interfering signal vs. third grating position relative to the collimation axis is shown for the mixed Na-Na_2 beam (● = no laser on) and the pure Na_2 beam (×=decoherence laser on, Δ=deflecting laser on, ○=both lasers on). Calculated curves are discussed in the text. The inset shows the interference fringe data for the mixed Na-Na_2 beam (●) and the pure Na_2 beam (○) observed with the 3rd grating at -10 μm..

3.3. Additional Data

The vapor pressure of atomic and diatomic sodium vs. pressure is shown in Fig. 3.3.1. For an effusive (non-jetting) source, the detected intensity of the atoms and molecules (and hence their relative intensity) is proportional to the vapor pressure. The situations changes somewhat for a jetting source, where the formation of dimers can be enhanced or suppressed depending on the particular conditions of the expansion. This has been studied in detail in the work by Gordon, Lee and Hershbach [GLH71] as well as in later work by Bergmann (see [BEH79] and references therein). There has also been previous experience with supersonic Na_2 and Li_2 beams in this laboratory (see J. Serri's thesis [SER80] and A. Migdall's thesis [MIG77], respectively).

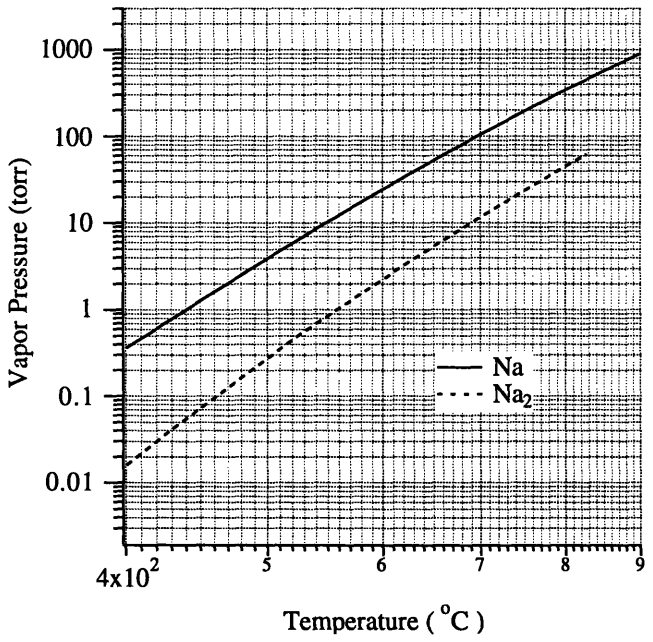

Fig. 3.3.1 Vapor pressures for atomic and diatomic sodium. Source: Liquid Metals Handbook, Sodium supplement, ed. C.B. Jackson, 3rd Ed. 1955 (Atomic Energy Commission).

Although it was not our intention to undertake a detailed study of our molecular source, some data we have taken along the way is presented in Fig 3.3.2 (Data B in this figure are from [EKS93]). For Data A, the nozzle temperature was held at 740°C, while for Data B, the nozzle temperature increased monotonically from 700°C to 770°C. In both cases, the carrier gas was argon (p = 1850 torr). Note that in Data A, the ratio of detected dimer fraction (left graph) exceeds that predicted from the ratio of the vapor pressures (solid curve) and increases much more rapidly than expected. For Data B, the rate of increase is also larger than expected, but the measured ratio does not exceed the ratio of the vapor pressures except for higher reservoir temperatures. The dramatic difference between the two sets of data likely due to the different nozzle temperatures and points to the important role of the nozzle expansion in determining the dimer fraction.

The right graph shows the atomic and molecular intensities separately for Data A (scaled by a common factor in order to compare the data with the vapor pressure curves), from which we see that the increased slope of the fraction of molecules in the beam is entirely due to the suppression of atomic sodium in the beam.

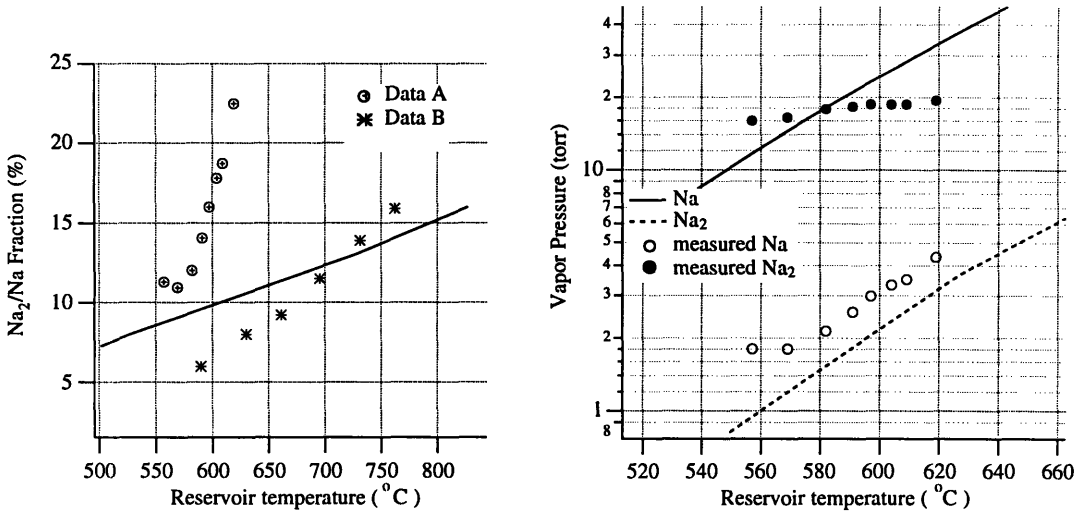

Fig: 3.3.2 Left graph: measured fraction of molecules in beam for different reservoir temperatures on two different runs. The solid curve is the ratio of the atomic and molecular vapor pressures. Right graph: measured atomic and molecular intensities (Data A, scaled by a common factor to compare with the vapor pressures) showing that deviation from the expected temperature variation of the fraction of molecules is due to a suppression of atomic sodium in the source.

Note that there is an inherent uncertainty in our determination of the ratio of dimers to atoms in our beam because it is unclear whether we detect one or two ions per molecule (that is, do we detect a single Na_2^+ ion or two Na^+ ions for every molecule). Time correlation measurements we performed suggested that we principally detect a single count for each molecule, however other studies using an ionization detector for Li_2 indicated (at least in that case) that two ions were detected for each molecule. Whether we detect one or two ions per molecule has no effect on our results except that we may be underestimating the counting statistics by a factor of $\sqrt{2}$.

The beam velocity in a supersonic source is given to a good approximation by $\sqrt{5kT/m}$ where m is the average mass of the gas. For most seeded sources such as ours, the partial pressure of the seed gas is much less than the carrier gas, and hence the average mass of the expansion gas mixture is largely determined by the mass of the inert

carrier gas. We noticed a significant departure from this situation, particularly when operating the reservoir at temperatures exceeding 700°C, where the vapor pressure of sodium can exceed 200 torr, a significant fraction of the typical carrier gas pressure (~1800 torr). To account for these effects, we use a simple model in which the mass of the carrier gas is replaced with the effective mass which is the weighted average of the masses of the carrier gas and seed. As shown, in Fig. 3.3.3, this correction provides reasonable agreement with the beam velocities measured from the diffraction patterns.

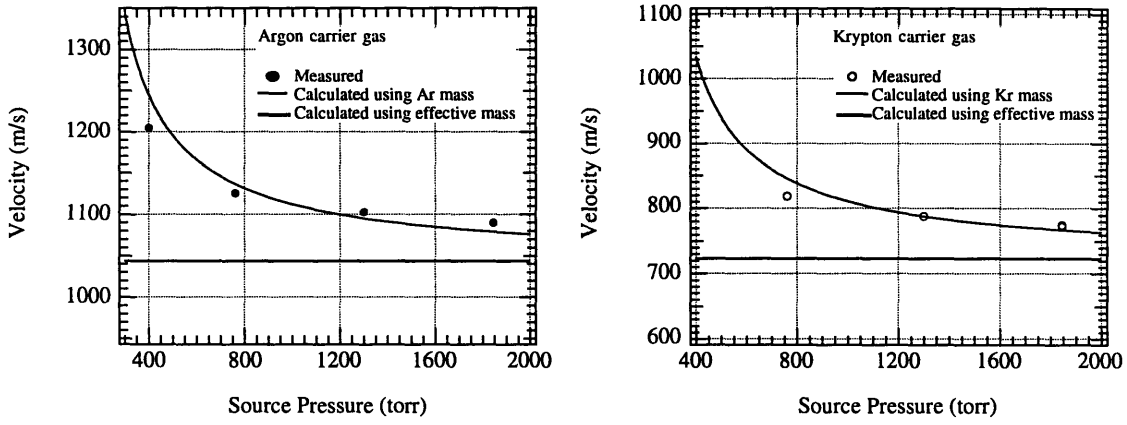

Fig 3.3.3 Deviation from the $v \approx \sqrt{5kT/m_{carrier}}$ relation when the vapor pressure of the sodium becomes comparable to the carrier gas pressure.

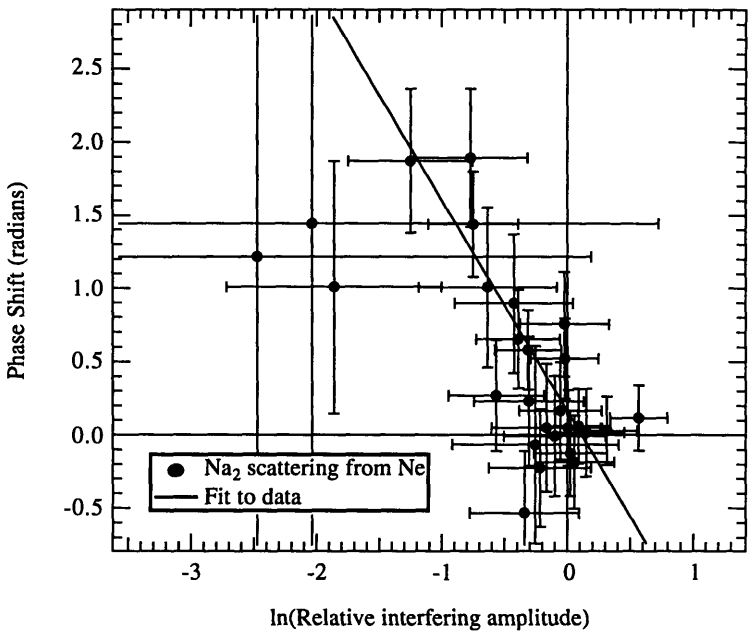

Fig. 3.3.4 Phase shift of the Na_2 interference pattern versus natural logarithm of the interfering amplitude (fringe height) when passing through the Ne gas cell. The slope of the fit directly determines the ratio of the real to imaginary part of the forward scattering amplitude. From this data, we find $\mathrm{Re}[f(k,0)]/\mathrm{Im}[f(k,0)] = 1.4(3)$.

In Fig 3.3.4, the experimental data used to determine the ratio of the real to imaginary parts of the Na_2-Ne forward scattering amplitude are shown. The signal to noise ratio of this data is considerably smaller than the data for the Na-Ne forward scattering amplitude we recorded with our atom interferometer [SCE95]. This is due to a combination of reasons: the intensity of the Na_2 beam is only 15-30% of the atomic beam, using Kr as the carrier gas (necessary to separate the interfering beams at the second grating), reduces the intensity by 50% or so, and finally, the septum clipped a sizable fraction of the beams and caused a loss in contrast.

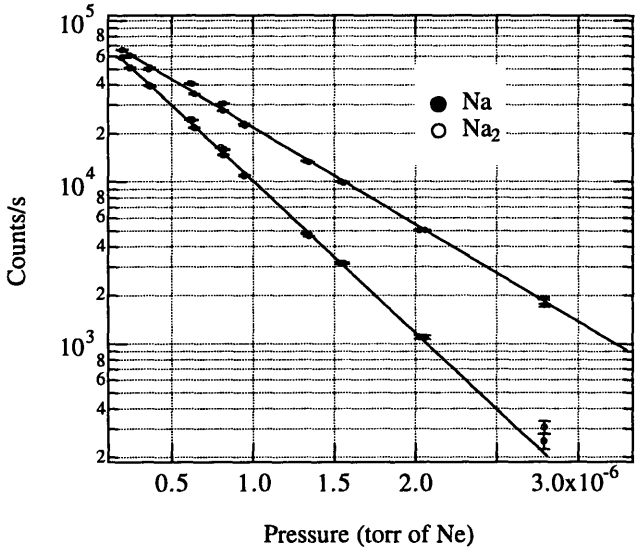

Fig 3.3.5 Measurement of the relative total scattering cross-section for atomic and molecular sodium scattering from neon. The detector counts are plotted versus the ion gauge pressure reading. From exponential fits to these data of the form $y = A\exp(-Bx)$, where x is the pressure increase, we determine the decay constants B of 2.15(3) x 10^6/torr for Na_2 and 1.38(3) x 10^6/torr for Na and their ratio 1.56(3).

In Fig 3.3.5, one of the data scans for the measurement of the total cross-section for Na_2-Ne scattering relative to Na-Ne is shown. This measurement was performed using a simple collimated beam and leaking a variable amount of Ne gas into the main vacuum chamber while recording the total on-line intensity. The measurement for a pure Na_2 and a mixed Na_2/Na is alternated every second or so by chopping the deflection laser beam for the atoms. The final result for this measurement was determined by three scans as in Fig. 3.3.5—the final results are shown in Fig. 3.3.6.

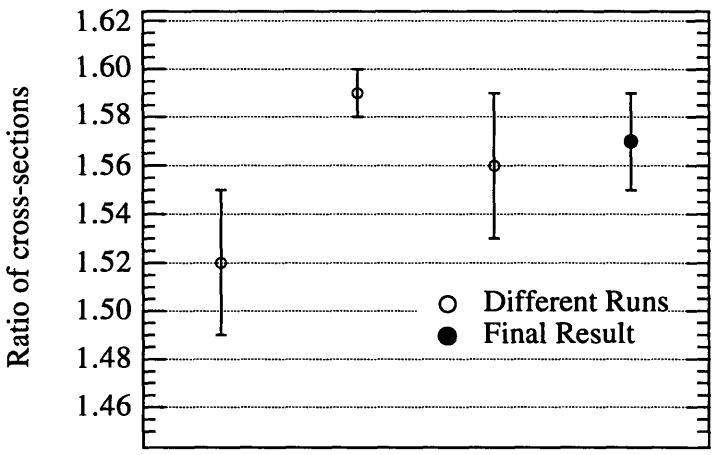

Fig 3.3.6 Determination of ratio of the total scattering cross-section for atomic and molecular sodium scattering from neon. The final result of 1.57(2) is determined by a weighted average of the three different measurements.

4. The Talbot Effect

In this chapter, I will discuss our demonstration of the Talbot effect using atom waves.* This is a near-field diffraction phenomena in which an illuminated periodic object (such as a grating) produces high quality real images of itself at locations downstream of the object. This is one of the few observation of near-field diffraction with atom waves to date (others include diffraction from a slit [LEB69] and demonstration of a zone plate [CSS91], [EKP92]). As we point out in our paper, it may have important applications to the field of atom lithography. Prior to our initial demonstration of the effect [SEC93], there was only one paper relating to self-imaging with atom waves [CLR89]. Since then Clauser et al. has demonstrated an interferometer based on the effect [CLL94] and other groups have proposed their use for atom lithography [JAW95] and atom localization for cavity QED experiments [CTK95]. A brief description and historical background of the phenomena will be followed by a copy of the paper we wrote on our work and, finally, the results of calculations we did to compare our results to theory.

---

* This chapter is a continuation of the experimental discussion in Ekstrom's thesis [EKS93]. No additional data is reported, however I will describe our analysis of the results and include our paper reporting this experiment.

4.1. Introduction and Background

First, a brief introduction. When a periodic object, such as a diffraction grating, is illuminated by a sufficiently coherent light source, high-quality images of the object are formed at periodic distances down-stream of the object. For plane wave illumination, these images are located at integer multiples of $d^2/\lambda \equiv L_{Talbot}/2$ where d is the periodicity of the object and λ is the wavelength of the source, and L_{Talbot} is known as the Talbot length. These self-images (often referred to as "Fourier images") arise from the (near-field) interference of the different diffracted components of the incident wave as suggested in Fig 4.1.1. It is characteristic of the images at odd multiples of d^2/λ to be out of phase with the object while those at even multiples are in phase.

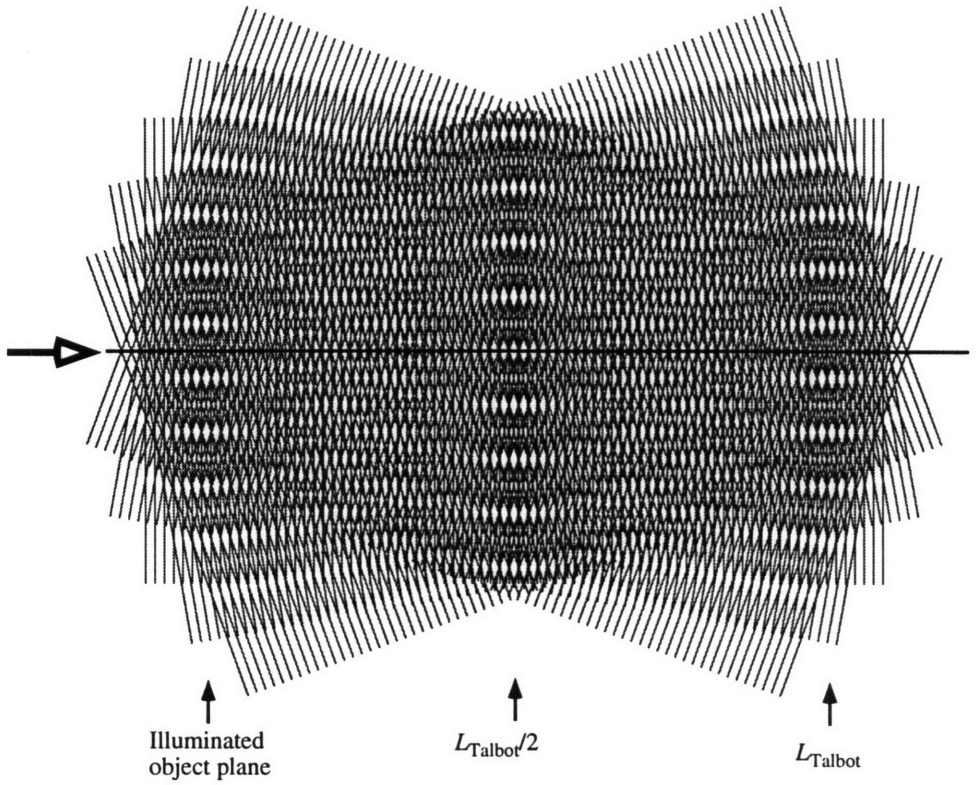

Fig. 4.1.1: A simple cartoon illustrating the Talbot effect. A period object is illuminated from the left with a monochromatic plane wave. The superposition of the 0th, 1st and 2nd order diffracted orders give rise to images of the object at particular locations downstream. The straight line emphasizes the phase shift of the image located at $L_{Talbot}/2$. (after a figure in [HIB59])

This phenomena was first discovered in 1836 by H. F. Talbot who was studying diffraction using a grating provided by Fraunhofer. The following excerpt is from Talbot's original paper [TAL36] and is included for historical perspective:

> Although so much has been explained in optical science by the aid of the undulatory hypothesis, yet when any *well-marked phenomena* occur which present unexpected peculiarities, it may be of importance to describe them, for the sake of comparison with theory. Such appears to me to be the case with those which I am about to mention...
>
> In order to see these appearances in their perfection, it is requisite to have a dark chamber and a radiant point of intense solar light, which, for the sake of convenience, should be reflected horizontally by a mirror. I will relate a few, out of several experiments which were made in this manner.

> About ten or twenty feet from the radiant point, I placed in the path of the ray an equidistant grating† made by Fraunhofer, with its lines vertical. I then viewed the light which had passed through this grating with a lens of considerable magnifying power, The appearance was very curious, being a regular alternation of numerous lines or bands of red and green colour, having their direction parallel to the lines of the grating. On removing the lens a little further from the grating, the bands gradually changed their colours and became alternately blue and yellow. When the lens was a little more removed, the bands again became red and green.
>
> It was very curious to observe that though the grating was greatly out of focus of the lens, yet the appearance of the bands was perfectly distinct and well defined.
>
> This however only happens when the radiant point has a *very small* apparent diameter, in which case the distance of the lens may be increased even to one or two feet from the grating without much impairing the beauty and distinctness of the coloured bands. So that if the source of light were a mere mathematical point it appears possible that this distance might be increased without limit; or that the disturbances in the luminous undulations caused by the interposition of the grating, continues indefinitely, and has no tendency to subside of itself.

Although brief by modern standards, this report includes most of the important aspects of the phenomena: the images are located at periodic distances away from the grating, the effect is chromatic, and very (spatially) coherent illumination is required.

In contrast to the familiar Fraunhofer diffraction observed at large distances (i.e. in the far-field), these images are located in the near-field characterized by Fresnel diffraction. Rayleigh provided the first analytical explanation for the formation of these images almost 50 years after their discovery [RAY81]. Modern interest in the phenomena can be traced to the "rediscovery" of the effect by Cowley and Moodie [COM57], who considered these images for use in electron microscopy to produce highly magnified images of period structures and coined the term "Fourier images." Their work, combined with the widespread availability of coherent lasers, has prompted considerable work in the field. An excellent comprehensive review of the self-imaging phenomena and its applications was recently written by Patorski [PAT89]. Self-imaging has been studied in a variety of wave systems including ultrasonic surface waves [HIB59], visible

---

† A plate of glass covered with gold-leaf, on which several hundred parallel lines are cut, in order to transmit the light at equal intervals.

and x-ray electromagnetic waves, and electron waves. Some of the more interesting applications of the Talbot effect include optical testing (a variation of the Ronchi method) and x-ray lithography [HCP81].

The use of atom waves for self-imaging was first suggested by Clauser and Reinsch [CLR89] who proposed a near-field three grating interferometer for atoms based on the Lau effect [LAU48]. This configuration was first studied by Chang et al. [CAL75] and others as discussed in [PAT89]. The Lau effect is an extension of the Talbot effect in which the point source (spatially coherent) illumination is replaced by an extended source and a grating. Although this offers considerable advantages in terms of signal intensity compared to the Talbot effect, the Lau effect, like the Talbot effect, is chromatic, and this presents considerable disadvantages for applications in atom optics, particularly when compared to our achromatic three-grating Mach-Zender interferometer, which also does not require a spatially coherent source [CAL75].

Our interest in self-imaging was initially motivated as a means to verify the dimensional uniformity of our diffraction gratings. By using one grating to measure the self-image of another (in a moiré fashion), we were able to set a maximal limit to the dimensional imperfections of both gratings. Our measurement of the Talbot effect for atom waves is presented in the following paper that recently appeared in Phys. Rev. A [CEH95].

4.2. Near Field Imaging of Atom Diffraction Gratings: the Atomic Talbot Effect, Phys. Rev. A **51**, R14 (1995)

Michael S. Chapman, Christopher R. Ekstrom,* Troy D. Hammond,

Jörg Schmiedmayer,† Bridget E. Tannian, Stefan Wehinger,† and

David E. Pritchard.

Department of Physics and Research Laboratory of Electronics

Massachusetts Institute of Technology, Cambridge, Massachusetts 02139, USA.

We have demonstrated the Talbot effect, the self-imaging of a periodic structure, with atom waves. We have measured the successive recurrence of these self-images as a function of the distance from the imaged grating. This is a near field interference effect that has several possible applications which are discussed.

PACS numbers: 03.75.Be, 07.60.–j, 42.25.Fx, 42.30.–d

* present address: Department of Physics, University of Konstanz, Germany

† permanent address: University of Innsbruck, Austria

Classical wave optics recognizes two limiting cases, near and far field. As the field of atom optics evolves, it is natural to expect interesting developments in both regimes. To date, developments in diffractive atom optics have been concentrated in the far field regime [1], in which the optical element may be regarded as imparting particular momenta to the atom wave, thereby directing it toward a set of final directions. This is usually accomplished by the absorption of pairs of photons or by diffraction from fabricated structures with locally periodic structure[2]. In the far field, the intensity pattern of the beam is characterized by Fraunhofer diffraction in which the curvature of the atom wave fronts can be neglected. In the near field, however, the curvature of the wave fronts must be considered, and in this case the intensity pattern of the beam is characterized by Fresnel diffraction. Of interest in this paper is a remarkable class of near field phenomena–the self-imaging of a periodic structure known as the Talbot effect.

Self-imaging of a periodic structure illuminated by quasi-monochromatic coherent light is well-known in classical optics and has many applications to image processing and synthesis, photo-lithography, optical testing and optical metrology [3]. This effect is also well-known in the field of electron optics and has many applications to electron microscopy [4]. It was first observed by Talbot in 1836 [5] and later explained by Rayleigh in 1881 [6]. Rayleigh showed that for a periodic grating illuminated by plane waves, identical self-images of the grating are produced downstream at observation distances that are integral multiples of $L_{Talbot} = 2d^2/\lambda$, where d is the grating period, λ is the wavelength of the incident radiation and L_{Talbot} is known as the Talbot length. Later workers [7-9] showed that identical self-images, laterally shifted by half a period, are also produced at distances midway between those explained by Rayleigh and that other images with smaller periods d/n $(n = 2,3,4...)$ are produced at intermediate distances.

The basic Talbot effect can be understood by considering the image formed at $\frac{1}{2} L_{Talbot}$ as shown in Figure 1. For this case, the path length differences between different

openings in the grating to a point on the observation plane along the optical axis are integer multiples of λ, and hence an image is formed with the same period as the grating but laterally shifted by half a period. The existence of spatial structure with the period of the grating is also expected downstream of the grating because this region contains overlapping waves whose momenta differ by the reciprocal grating vector. Full treatment of the problem, including predictions of the positions and contrast of the subperiod images, requires solving the Fresnel diffraction problem with more formal techniques [3].

Here, we present measurements of the contrast of successive self-images with atom waves using transmission gratings with two different periods, 200 nm and 300 nm [10]. After discussing the apparatus, procedure, and results, we point out the use of Talbot images for checking grating coherence and suggest a scheme for their use in direct-write atom lithography.

A schematic of the experiment is shown in Figure 2. Illuminating the first transmission grating by a collimated atom beam produces Talbot self-images of the grating downstream. To detect these images, a second transmission grating is placed downstream to mask the image. If the period of the second grating matches that of the image, it will alternately block and transmit the image as it is laterally scanned, and the total transmitted intensity measured by the detector will display a moiré fringe pattern with respect to the lateral position of the second grating. We measure the contrast of these moiré fringes as a function of the separation between the two gratings. In this experiment, we used gratings of the same period for the first and second gratings and hence expect to see high contrast fringes for grating separations that are half-integral multiples of L_{Talbot}.

The atomic beam system used for this experiment is the same used for our atom interferometer studies and has been recently described elsewhere [10-12]. We use a well-collimated sodium beam produced by a seeded supersonic source with argon as the

carrier gas. Beam collimation is provided by two 20 μm slits separated by 85 cm, yielding a ribbon-shaped beam approximately 20 μm wide by 0.5 mm high with a beam divergence of 23 μrad. The sodium beam propagates through an evacuated drift region containing two transmission gratings. The transmitted sodium atoms are individually detected by a channel electron multiplier after being ionized by a 50 μm rhenium wire heated to ~850°C. The background of the detector is typically less than 50 cps. The beam has a mean velocity of ~1000 m/s (corresponding to $\lambda_{dB} = 0.17\,\text{Å}$) and has an rms velocity width of 3.7%.

The gratings consist of a periodic array of slots etched through a thin (~100 nm) silicon nitride membrane [13]. The gratings are rotationally aligned by maximizing the measured contrast with respect to rotation of the second grating. The second grating is mounted on a translation stage, and the distance between the two gratings, z, can be varied from 3.5 mm to 13.5 mm. The point-to-point error associated with each grating translation is less than 10 μm, however, the absolute grating separation is known only to within 0.5 mm due to the grating mounting system. Grating vibrations are minimized by mechanically isolating the mechanical vacuum pumps in the apparatus, but we made no attempt to measure the residual relative vibrations of the gratings.

We have performed this experiment with 200 nm and 300 nm period transmission gratings, which for our atomic beam yield Talbot lengths of 4.7 mm and 10.6 mm, respectively. The transverse position of the second (mask) grating is scanned using a piezo-electric transducer (PZT) that is calibrated with the laser interferometer described in Ref. [11]. To measure the Talbot image, the total transmitted intensity is recorded as a function of the PZT position. A typical scan is shown in Figure 3. The distance between the gratings is then varied, and the contrast of the moiré fringe pattern is determined as a function of grating separation.

The experimental results are shown in Figure 4 for both the 200 nm and 300 nm gratings. The data demonstrate high contrast self-images of the first grating at approximate grating separations of L_{Talbot} and $\frac{3}{2}L_{Talbot}$ for the 200 nm gratings and $\frac{1}{2}L_{Talbot}$ for the 300 nm gratings. The contrast of the images damps out for larger grating separations primarily because of the transverse incoherence of the source determined by the collimation of the beam. This effect is illustrated with a simple model in which an extended incoherent source is modeled as an incoherent superposition of point sources [3]. For a grating illuminated by two mutually incoherent point sources laterally separated by x, it is readily shown that the two self-images produced by these point sources are displaced laterally by $\Delta x = xz/R$, where R is the distance from the point sources to the grating and z is the distance from the grating to the image plane. Because the two sources are mutually incoherent, the intensities add (not the amplitudes) and the two self-images will wash out when Δx is on the order of half the image period. For our experimental configuration, $\Delta x \approx 10^{-4} z$, and hence we would expect the contrast to damp out at ~10 mm of grating separation for the 200 nm gratings and at ~15 mm for the 300 nm gratings.

In order to compare our results to theory in more detail, we have performed numerical calculations based on a coherent ray tracing algorithm that was developed to model our atom interferometer [14]. Starting with an extended incoherent polychromatic source, this algorithm performs a coherent sum of the amplitudes for each path through the collimators and gratings. Notably, the calculations do not include effects due to vibrations of the apparatus or grating imperfections such as local variations in grating bar positions or larger-scale phase errors of the gratings. These effects will reduce the contrast of the images and will have a larger effect on the finer period gratings. The maximum measured contrast is ~60% of the calculated value for the 200 nm gratings and ~70% of the calculated value for the 300 nm gratings. The calculated contrast as a

function of grating separation is compared with our observations in Figure 4–the curves are normalized to match the measured contrast at the first peak.

Best agreement with the data was obtained by varying two parameters of the calculation–the collimator widths and open-fractions of the gratings (defined as the ratio of slot width to grating period). The collimator slits are nominally 20 microns wide, but can be narrower due to clogging. The best agreement with the data was obtained for a slit width of 13 μm for the 200 nm data and 17 μm for the 300 nm data. We attribute this discrepancy to clogging of the collimators, which is consistent with the fact that the collimators were cleaned between the time the 200 nm and 300 nm data were taken. Effectively narrower collimation slits improves the transverse coherence of the beam and increases the visibility of the contrast revivals as discussed above. The width of the calculated contrast revival peaks depends on the open fractions of the gratings, with larger grating open fractions yielding broader peaks. Best agreement with the 300 nm data was obtained for a 50% open fraction, which agrees well with our estimation of the grating open fraction determined by measuring the relative transmission through the gratings. Similar measurements with the 200 nm gratings indicate an open fraction of ~25%, which is somewhat smaller than the 40% open fraction used in the calculation to obtain the best fit. The greater open fraction required to fit the 200 nm data may reflect the greater effect of contrast-lowering imperfections in these finer gratings.

Because of the limitations in the calculations discussed above, a fully quantitative comparison of our experimental results with our calculations is not warranted. However, with reasonable variations of the experimental parameters, we have obtained good agreement with the widths and relative amplitudes of the successive grating images that we observed.

The measurement of the contrast of the self-images sets a limit to the extent of grating imperfections such as variations in the open fractions and large-scale phase errors,

and therefore provides an experimental test of overall grating quality. Indeed, an ancillary motivation for this experimental work was to test the spatial coherence of the gratings we use in our atom interferometer.

As Lau showed in 1948 [15], the requirements on good source collimation to preserve the contrast of the Talbot self images can be circumvented by using an additional grating placed in front of an extended source. In the Lau effect, which is closely related to the Talbot effect, an additional grating is placed in front of an extended incoherent source, and for particular grating separations, self-images of the second grating are formed. Clauser and Li [16] have recently reported the observation of Lau images in a three grating atom interferometer [3,11]. Whereas they report the observation of a superposition of reduced period images for a single set of grating separations, we have measured the recurrent self-images of a single grating for a range of observation distances.

A promising application of Talbot (or Lau) imaging with atoms is in the emerging field of atomic lithography [17]. Recent efforts in this field have used resonant light forces. Obviously fabricated gratings like the ones used here are species inspecific and should work with a variety of materials. This has the additional advantage that the period of the structures produced does not depend on the wavelength of the light resonant with that species. In addition, it should be possible to write smaller features using the reduced period intermediate images discussed above. These images have been used successfully in x-ray lithography to write half-period gratings [18]. It may be possible to use atom beams for this process to write an image directly with the desired material (e.g. silver), which could be subsequently enhanced by electroplating or photographic development. Grating self-images may also be used in quantum optics experiments to produce a periodic atom density in an optical resonator [19].

In conclusion, we have demonstrated the Talbot effect with atom waves. This is a completely diffractive phenomena that occurs in the Fresnel diffraction region. We have demonstrated the recurrence of the self-images as a function of the distance from the imaged grating and shown that the results are qualitatively consistent with theoretical predictions.

We acknowledge the technical contributions of Richard Rubenstein. We also thank Michael Rooks and other staff members at the National Nanofabrication Facility. This work was supported by the Army Research Office contracts DAAL03-89-K-0082, and ASSERT 29970-PH-AAS, the Office of Naval Research contract N00014-89-J-1207, and the Joint Services Electronics Program contract DAAL03-89-C-0001. TDH acknowledges the support of a National Science Foundation graduate fellowship. JS and SW acknowledge support from the University of Innsbruck, Austria.

References

1. Two notable exceptions are near-field atomic diffraction from a slit by J.A. Leavitt and F.A. Bills, Am. J. Phys. **37**, 905 (1969) and focusing of an atomic beam with a Fresnel zone plate by O. Carnal, M. Sigel, T. Sleator, H. Takuma and J. Mlynek, Phys. Rev. Lett. **67**, 3231 (1991).

2. See, for example, I. Estermann and O. Stern, Z. Phys. **37**, 905 (1930). P.L. Gould, G.A. Ruff and D.E. Pritchard, Phys. Rev. Lett. **56**, 827 (1986). D.W. Keith, M.L. Schattenburg, H.I. Smith and D.E. Pritchard, Phys. Rev. Lett. **61**, 1580 (1988). M. Kasevich and S. Chu, Phys. Rev. Lett. **67**, 181 (1991). O. Carnal, A. Faulstich and J. Mlynek, Appl. Phys. B **53**, 88 (1991).

3. See the recent review by K. Patorski. in *Progress in Optics* , vol.XXVII, edited by E. Wolf (North-Holland, Amsterdam, 1989).

4. R.D. Heidenreich. *Fundamentals of Transmission Electron Microscopy* (Interscience Publishers, New York, 1964).

5. H.F. Talbot, Philos. Mag. **9**, 401 (1836).

6. L. Rayleigh, Philos. Mag. **11**, 196 (1881).

7. J. Cowley and A. Moodie, Proc. Phys. Soc. B **70**, 486, 497, 505 (1957).

8. G.L. Rogers, Br. J. Appl. Phys. **15**, 594 (1964).

9. J.T. Winthrop and C.R. Worthington, J. Opt. Soc. Am. **55**, 373 (1965).

10. J. Schmiedmayer, C. R. Ekstrom, M. S. Chapman, T. D. Hammond and D. E. Pritchard, in *Fundamentals of Quantum Optics III*, Proceedings, Kühtai, Austria, Ed. F. Ehlotzky, Lecture Notes in Physics 420 (Springer-Verlag, 1993). In this paper, we reported the observation of Talbot images for atoms at a single grating separation.

11. D.W. Keith, C.R. Ekstrom, Q.A. Turchette and D.E. Pritchard, Phys. Rev. Lett. **66**, 2693 (1991).

12. C.R. Ekstrom, J. Schmiedmayer, M.S. Chapman, T.D. Hammond and D.E. Pritchard, *submitted for publication.*

13. C.R. Ekstrom, D.W. Keith and D.E. Pritchard, App. Phys. B **54**, 369 (1992).

14. Q.A. Turchette, D.E. Pritchard and D.W. Keith, JOSA B **9**, 1601 (1992).

15. E. Lau, Ann. Phys. (Germany) **6**, 417 (1948).

16. J.F. Clauser and S. Li, Phys. Rev. A **49**, R2213 (1994).

17. G. Timp, R.E. Behringer, D.M. Tennant, J.E. Cunningham, M. Prentiss and K.K. Berggren, Phys. Rev. Lett. **69**, 1636 (1992) and J.J. McClelland, R.E. Scholten, E.C. Palm and R.J. Celotta, Science **262**, 877, 1993.

18. D.C. Flanders, A.M. Hawryluk and H.I. Smith, J. Vac. Sci. Technol. **16**, 1949 (1979).

19. O. Carnal, Q.A. Turchette and H.J. Kimble, submitted for publication.

Figure Captions

Figure 1: A simple model illustrating the self-imaging of a grating illuminated by plane waves. It is readily shown that the path lengths s_n from an opening on the grating to the point P are given by $s_n \approx s_0 + n(n+1)\lambda/2$. Hence, any two path lengths differ by integral multiples of λ, resulting in an intensity maximum at P and, by symmetry, at the other indicated points.

Figure 2: Schematic of the experimental apparatus. The distance between the two gratings, z, can be varied from 3.5 mm to 13.5 mm. The lateral position of the second grating is scanned using the PZT.

Figure 3: Detection of the Talbot self-image. The upper graph shows the lateral position of the second grating. The lower graph shows the intensity transmitted through both gratings. A moiré fringe pattern of the intensity is seen as the second grating is scanned across the self-image. The more rapid oscillations come from the fly-back of the PZT. This data was taken with 300 nm gratings separated by $z \approx \frac{1}{2} L_{Talbot}$.

Figure 4: The experimental data and calculations (see text) showing the contrast of the self-image as a function of grating separation for 200 nm gratings (above) and 300 nm gratings (below). The error bars are statistical only, and positional errors are discussed in the text. The arrows indicate grating separations that are half-integral multiples of L_{Talbot}.

Figure 1

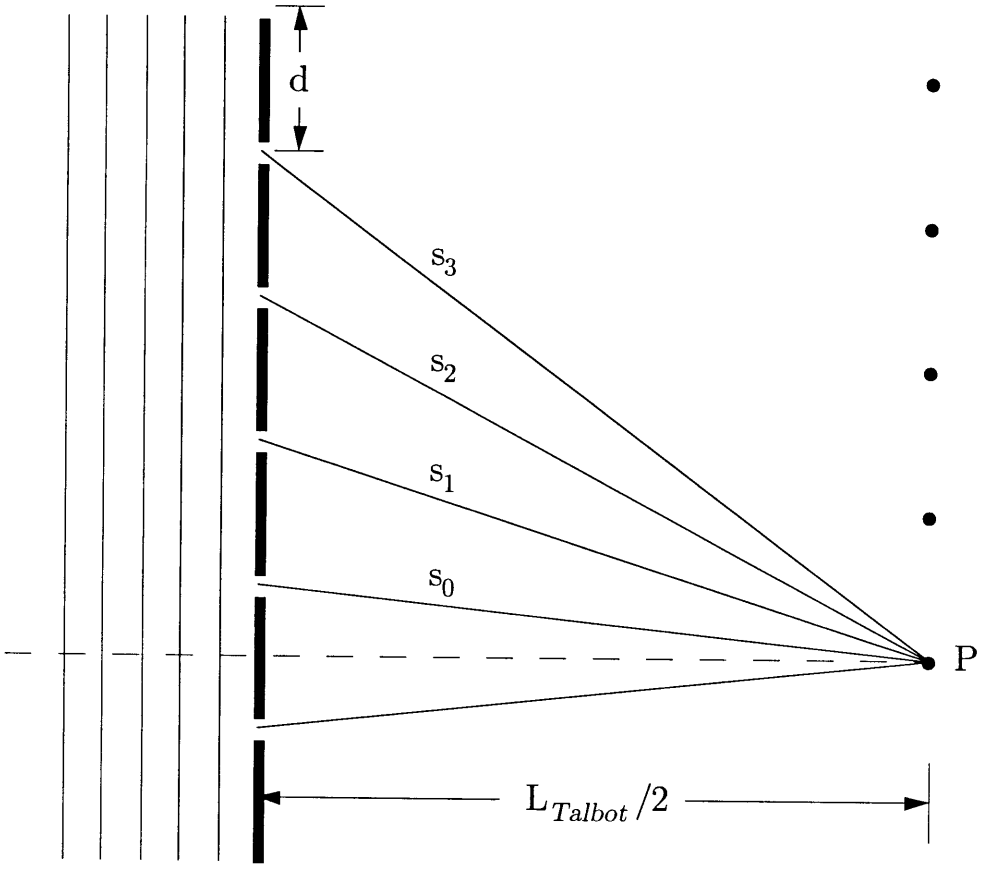

Figure 2

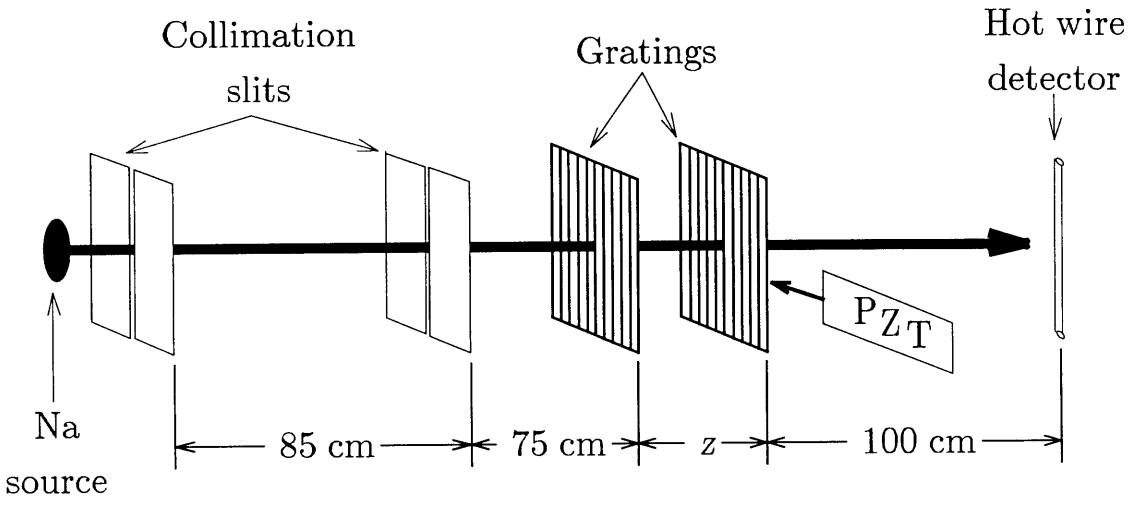
Collimation
slits
Gratings
Hot wire
detector
PZT
Na
source
85 cm
75 cm
z
100 cm

Figure 3

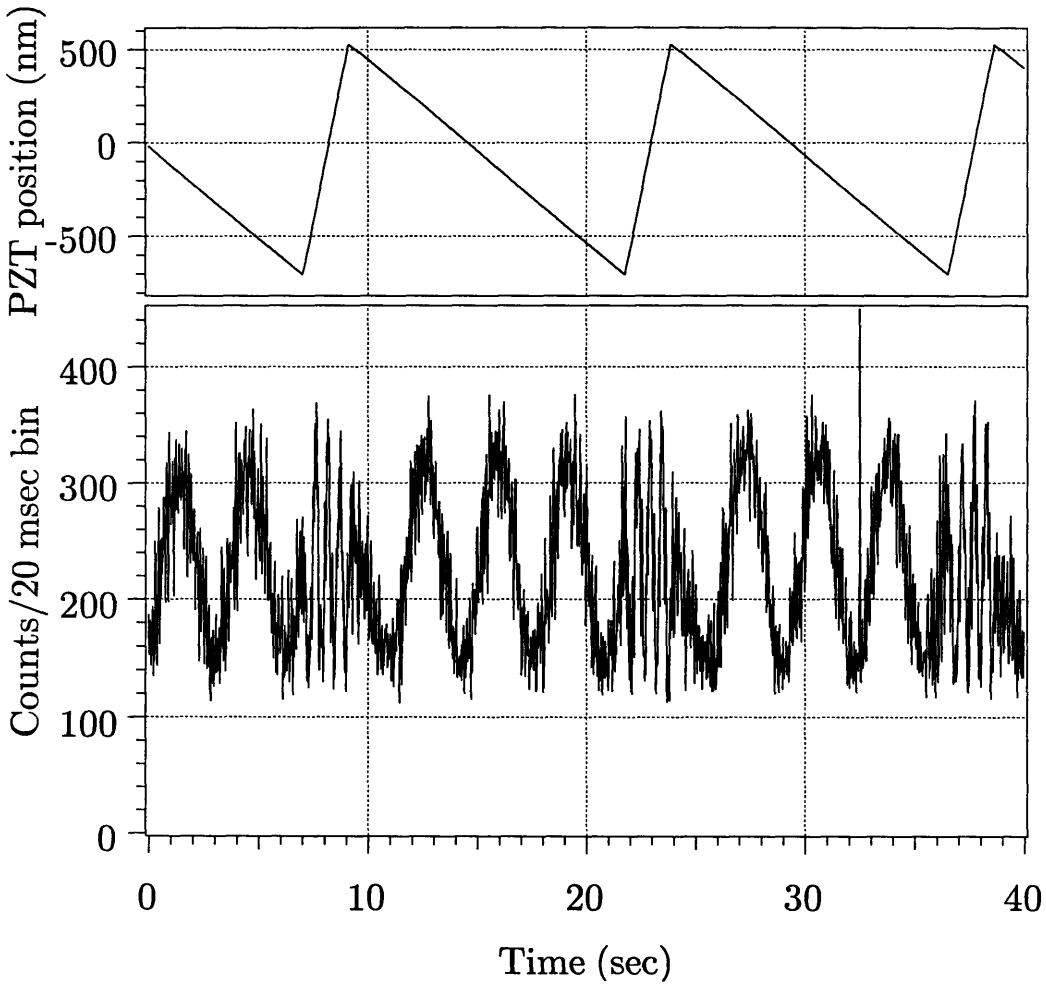
PZT position (nm)
500
0
-500
Counts/20 msec bin
400
300
200
100
0
0
10
20
30
40
Time (sec)

Figure 4

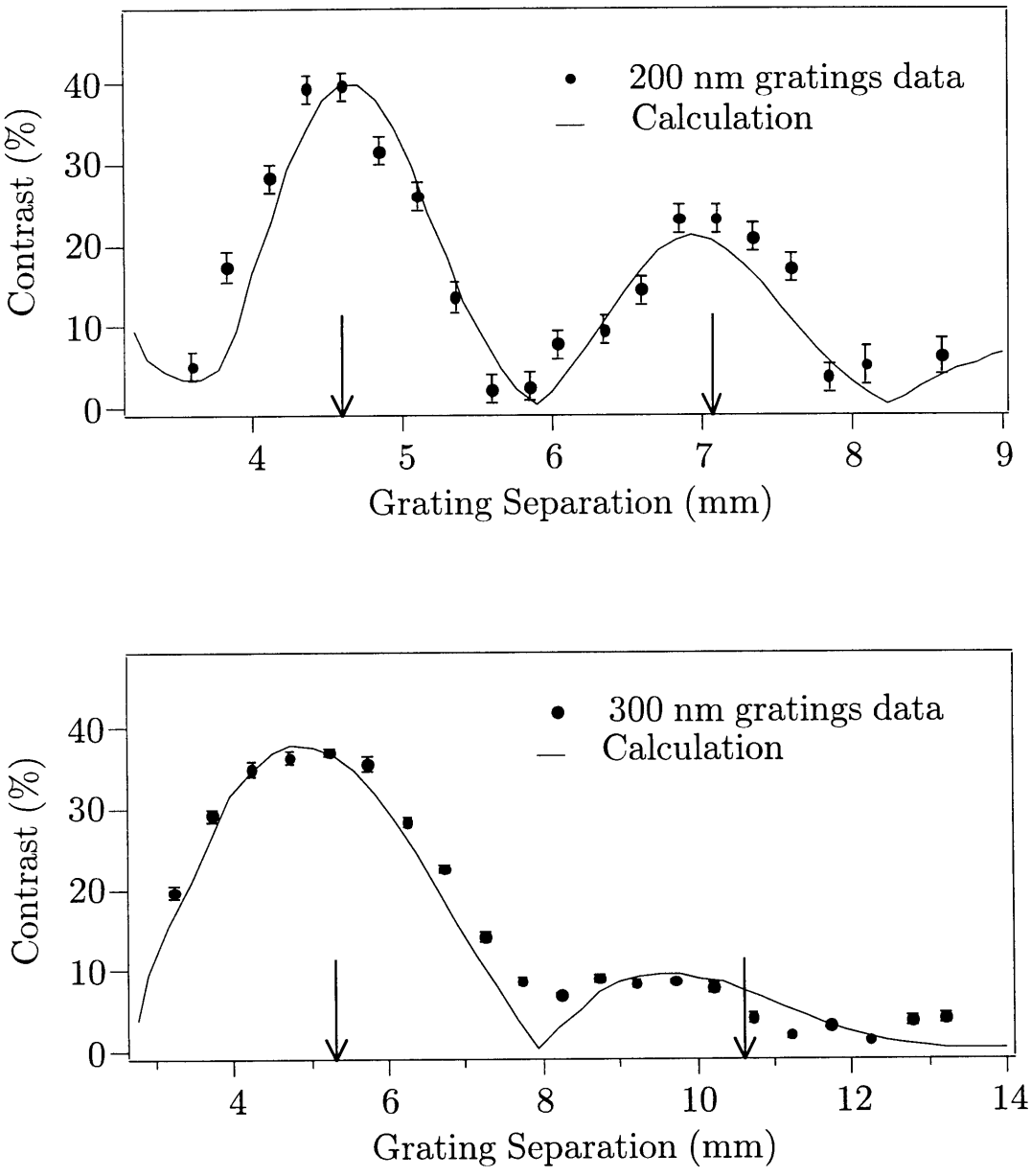
200 nm gratings data
Calculation
Contrast (%)
Grating Separation (mm)
300 nm gratings data
Calculation
Contrast (%)
Grating Separation (mm)

4.3. Basic Theory

The Talbot effect is one of the few near-field diffraction problems with analytic solutions,. In that sense, it is perhaps surprising that it is not more widely taught. The effect is easily demonstrated with a He-Ne laser and a simple binary transmission grating with a 1 mm period,* for which the Talbot length is on the order of 0.6 m from the grating.

We begin with the general Fresnel-Kirchoff integral formula for diffraction from a planar aperture (see e.g. [BOW80], [COW75], the treatment below closely follows the latter reference)

$$\psi(x,y)=\frac{i}{2\lambda}\iint\frac{\exp\{-ikr'\}}{r'}q(X,Y)\frac{\exp\{-ikr\}}{r}[\cos(\hat{Z},r')-\cos(\hat{Z},r)]dXdY \quad (4.1)$$

where the coordinates are indicated in Fig 4.3.1 and $q(X,Y)$ is the complex transmission function of the aperture.

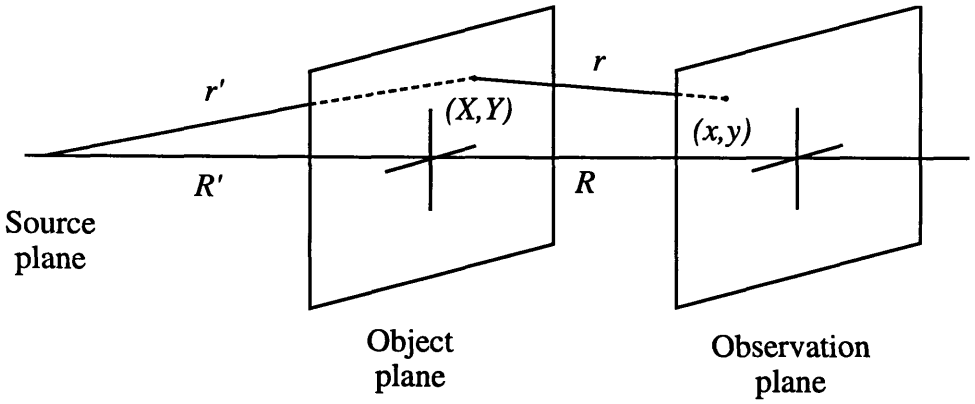

Fig. 4.3.1: Diagram showing the coordinates used for the Fresnel diffraction of a planar object.

* Such a grating can be easily made with a laser printer and transparencies.

We make the usual paraxial (small angle) assumption, with which the obliquity factor $\cos(\hat{Z},r')-\cos(\hat{Z},r)\approx -2$ and the denominators within the integral are set to R' and R, the distance from the source and observation screen normal to the plane of the object. To simplify matters a bit, we will restrict ourselves for the moment to plane wave illumination with $\hat{k}\ \|\ \hat{Z}$ in which case the first exponential term may be taken out of the integral and we have

$$\psi(x,y)\propto\iint q(X,Y)\frac{\exp\{-ikr\}}{r}dXdY. \tag{4.2}$$

We now make the usual Fresnel (parabolic) approximation for r, keeping terms up to 2nd order:

$$\begin{aligned} r&=\sqrt{(x-X)^2+(y-Y)^2+R^2}\\ &\approx R+\frac{(x-X)^2+(y-Y)^2}{2R} \end{aligned} \tag{4.3}$$

and restrict ourselves to one dimensional objects $q=q(X)$ so that we have

$$\psi(x,R)\propto\int q(X)\exp\left\{\frac{-ik(x-X)^2}{2R}\right\}dX. \tag{4.4}$$

This is the general one-dimensional Fresnel diffraction formula for plane wave illumination. Generally, this integral cannot be solved analytically, and one resorts to numerical techniques or expresses the integral as a sum of Fresnel integrals for which the results are tabulated.

However, if we consider the transfer function $q(X)=\cos\left(n\frac{2\pi}{d}X\right)$, the integral can be solved analytically to give

$$\psi(x,R)\propto\exp\left(i\pi\lambda\frac{n^2}{d^2}R\right)\cos\left(n\frac{2\pi}{d}X\right) \tag{4.5}$$

and hence for any transfer function that can be expanded in a Fourier series, $q(X)=\sum_n a_n \cos\left(n\frac{2\pi}{d}X\right)$, we can immediately write

$$\psi(x,R)\propto\sum_n a_n \exp\left(i\pi\lambda\frac{n^2}{d^2}R\right)\cos\left(n\frac{2\pi}{d}X\right). \tag{4.6}$$

When $R=m2d^2/\lambda$, the exponent is $2\pi mn^2$ which is modulo 2π, and hence an *identical* image of the initial transmission function appears.

For $R=md^2/\lambda$ where m is now *odd,* the exponent is πmn^2 which is an odd multiple of π when n is odd and an even multiple of π when n is even hence we can write

$$\begin{aligned}\psi(x,R)&\propto\sum_n a_n \exp(i\pi n)\cos\left(n\frac{2\pi}{d}X\right)\\ &\propto\sum_n a_n \cos\left[n\frac{2\pi}{d}\left(X\pm\frac{d}{2}\right)\right]\end{aligned} \tag{4.7}$$

which is just the original image shifted by a half period.

The analytic techniques can be extended with a little more algebra to the case of spherical (or point source) illumination* for which there is a magnification of the images given by $M=(R'+R)/R'$ (which is less than 10% for our experimental configuration), as well as a shift in their axial location $R=2md^2R'/\left(\lambda R'+2md^2\right)$. With these solutions, the effects of a finite source size and spectral distribution can be simply handled by summing up the *intensity* distributions (i.e. summing up the square of the equation analogous to Eq. 4.7 for the spherical wave illumination).

---

* see especially the treatments in [COM57] and [WIW65] as well as the nice presentation in [CTK95]

4.4. Numerical Calculations

Although the treatment outlined above is quite complete within the approximations specified, we used a numerical ray tracing algorithm to compare our results to theory. This algorithm is a modified version of the one we used to model our interferometer [TUR91], [TPK92]. The primary advantage of using a ray-tracing algorithm for our problem is that it allows us to include the effects of gratings of finite extent (in our experiment, we illuminated ~200 bars). The other advantage is that the algorithm was fully developed—already incorporating the finite width of our source and the velocity distribution of the beam—and required only slight modifications for our problem.

We studied the variation of many different parameters of the model to investigate the longitudinal variation of image contrast and to obtain the best fit with the experimental data (see Fig. 4 in the proceeding paper) . Some of the results of these calculations are given below.

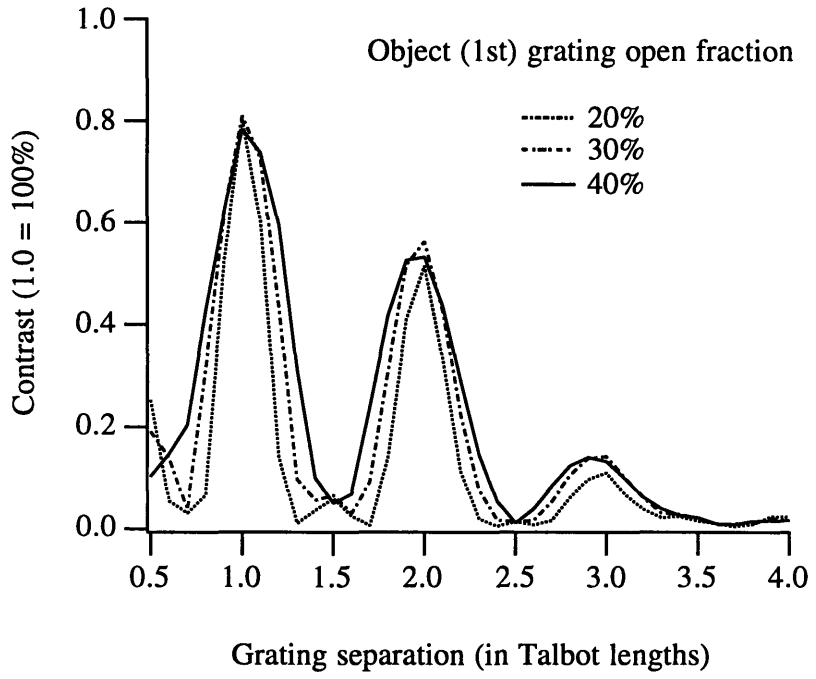

Fig. 4.4.1: Calculated curves showing the variation of the Talbot image visibility for different open fractions of the 1st (object) grating. Note the narrowing of the recurrences for smaller open fractions.

The open fraction of the object grating was found to have a strong influence on the width of the image recurrences (i.e. depth of field of the images). This can be understood heuristically from Eq. 4.6. Smaller open fractions correspond to a larger range of higher order harmonics a_n contributing to the sum, which implies that the exponential term in Eq. 4.6 will be much more sensitive to deviations from $R = m2d^2/\lambda$. The opposite extreme is for a cosinusoidal grating as in Eq. 4.5, for which the image contrast is independent of R.

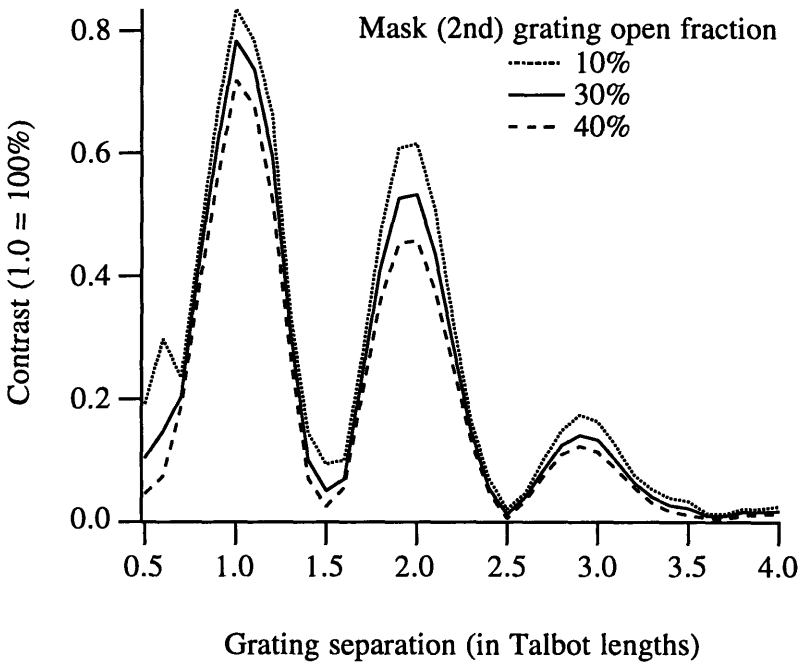

Fig. 4.4.2 Calculated curves showing the variation of the Talbot image visibility for different open fractions of the 2nd (mask) grating. The curves are qualitatively very similar.

As expected, varying the 2nd grating open fraction affected the overall contrast of the detected images, but had little effect on the width of the recurrences or their relative contrast.

Varying the width of the collimating slits had a significant effect on the relative contrast of the recurrent self-images. Larger collimation slits correspond to poorer spatial coherence of the source and hence lower visibility of the recurrences is expected. As explained in the proceeding paper, this effect can be understood heuristically by considering a finite-width source as an incoherent superposition of point sources. The self-image generated by each point source is displaced in the observation plane relative to the others, thereby reducing the contrast of the resultant image formed by the incoherent sum of the images due to each source element.

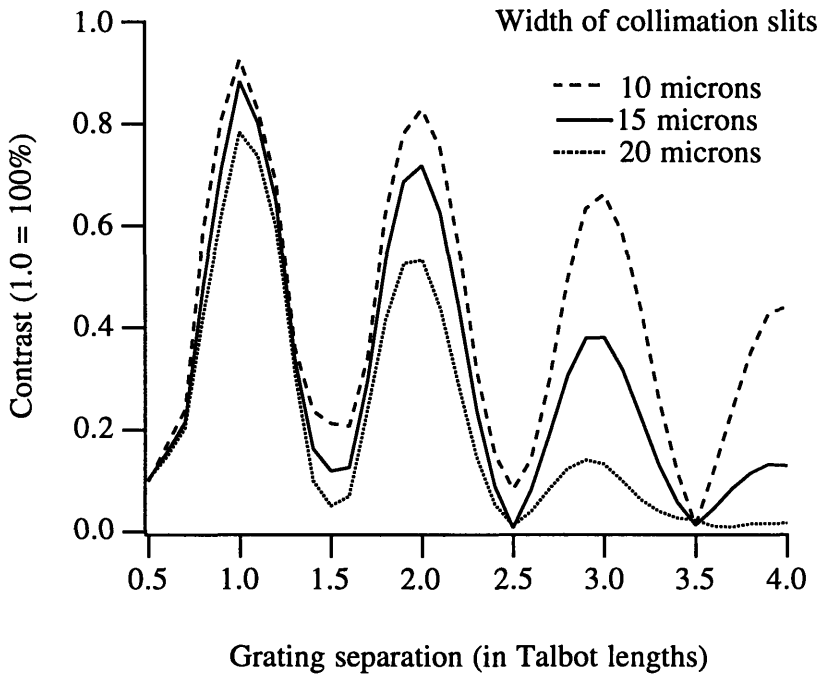

Fig. 4.4.3 Calculated curves showing the variation of the Talbot image visibility for different widths of the collimation slits. The images damp out much more rapidly for wider slits that correspond to less spatial coherence of the source.

Appendix A: Na Polarizability Reconsidered

In this appendix, I will discuss the methods and results of an independent partial reanalysis of the experimental results of our measurement of the ground state dc-electric polarizability of atomic sodium. This reanalysis was prompted, in part, by referees' comments made in the course of the review process of our paper reporting this measurement [ESC95], but mostly by our determination to understand possible systematic errors in our interferometer. Although this reanalysis uses a different strategy for handling the drift and fluctuations of the phase of the interference fringes, the final result we obtain falls well within the originally quoted uncertainty.

The polarizability experiment was the first measurement we performed with our unique separated-beam interferometer, and it is described in detail in Chris Ekstrom's thesis [EKS93] and a paper [ESC95]. Our measurement, with an overall accuracy of 0.35%, was over 20 times more accurate than the previous best absolute measurement [HAZ74], and 7 times more accurate than the uncertainties in the previously accepted value obtained from a comparison of relative measurements of the polarizabilities of Na and He^* to the theoretically calculated polarizability of He^* [MSM74]. This increased accuracy allows us to discriminate between ten or so theoretical calculations of this important atomic parameter.

In most precision measurements, it is necessary to quantify the uncertainties or potential errors of many different experimental (and perhaps theoretical) contributions to

the final result. Additionally, the measurements are often repeated many times to reduce the statistical uncertainties of the measurement. The final result is then obtained by combining the results of these different measurements each weighted according to their relative uncertainty. There is often more than one "right" way to combine the many measurements into a final result, and it is necessary for the experimentalist to exercise his or her best judgment. Of course, a very reasonable approach is to try different strategies to see if the final results are consistent, and it was in this spirit that this reanalysis was undertaken.

Brief review of the experiment

To measure the ground state polarizability of sodium, a uniform electric field was applied to one side of the interaction region in the separated-beam atom interferometer (see Fig A.1). The potential energy of the atom in the electric field is shifted by an

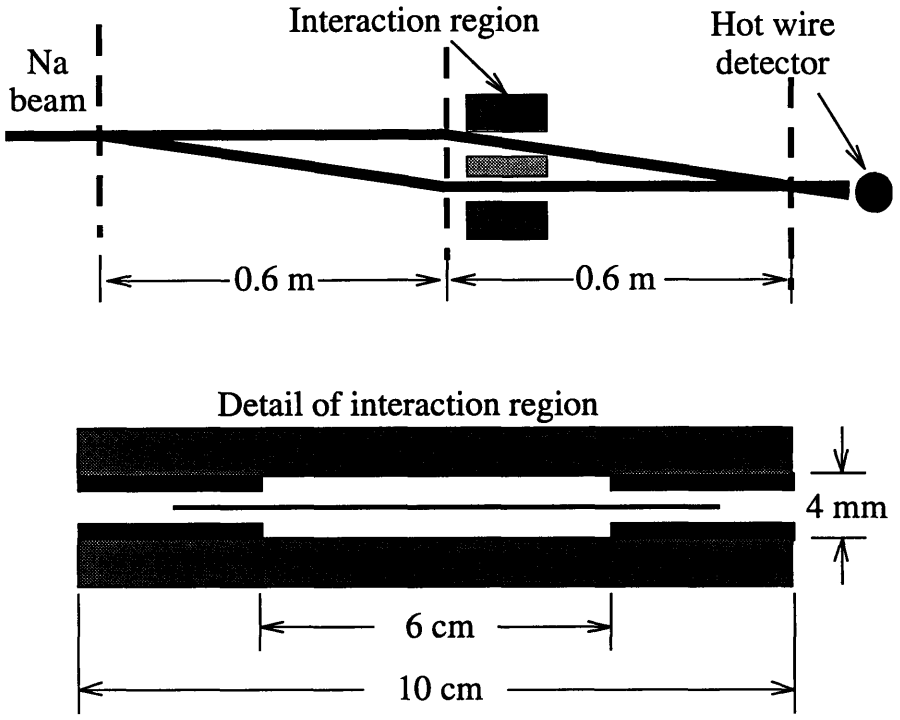

Fig. A.1: A schematic of the separated-beam atom interferometer showing the interaction region with a conducting foil physically isolating the two interfering beams.

amount $U(z) = -\frac{1}{2}\alpha\left|\vec{E}(z)\right|^2$ where α is the dc-polarizability of the atom and $\vec{E}(z)$ is the applied electric field—this is the well-known quadratic Stark shift. This produces a phase shift we can easily calculate using the JWKB method

$$\Delta\phi(v) = \int k(x)dz - \int k_0 dz \approx \frac{1}{\hbar v}\int U(z)dz \tag{A.1}$$

Determination of Alpha

We measured the phase shift of the interferometer for different applied voltages, which when combined with measurements of the beam velocity, and the interaction region geometry allowed us to determine the polarizability through the relation

$$\alpha = \left(\frac{\Delta\phi_{Stark}}{V^2}\right)\left(\frac{D^2}{L_{eff}}\right)(2\hbar v) \tag{A.2}$$

The first term on the right-hand side is determined by a quadratic fit of the phase shift versus the applied voltage. The second term is solely determined by the interaction region geometry where D is the measured electrode spacing and the effective length of the interaction region, $L_{eff} \equiv \left(\frac{D}{V}\right)^2 \int \left|\vec{E}\right|^2 dz$, is found from a numerical calculation of the electric fields. Finally, the beam velocity v and the width of the velocity distribution of the beam are determined by measuring the atomic diffraction pattern from a single grating. It is necessary to apply small corrections (~0.4%) to the measured phase shift to account for the dispersive nature of the phase shift and for the fact that the interaction region selectively blocks faster atoms (smaller diffraction angle) thus altering the velocity distribution of the interfering atoms relative to those in the atomic beam.

Phase drifts and noise

The phase of the atomic interference fringes (measured with respect to the laser interferometer) varies with time even when there is no applied interaction. There is a long term phase drift of the fringes on the order of 1 rad/hour, as well as short term phase fluctuations or noise as large as 150 mrad/min rms [EKS93]. Much of the long term phase drift of the machine is almost certainly due to thermal expansion and contraction of the machine. We have observed a much larger drift rate when the sun first strikes the machine in the morning, and we have covered the windows for this reason. To first order, the laser interferometer should compensate for any bending of the machine in the plane of the interferometer and any overall length change of the machine along the beam axis. Torsional deflections of the beam tube should also be compensated by the laser interferometer to the extent that the laser interferometer is in the same plane as the atom interferometer. One possible source of thermal expansion phase drifts could be thermal fluctuations of the aluminum bar on which the atom grating and laser gratings are mounted. The transverse distance between the atom and laser gratings is on the order of 1 cm which changes by 230 nm/^{o}C (the coefficient of thermal expansion of aluminum is

23 x $10^{-6}/^{o}C$). This would produce an atomic fringe phase of over $2\pi/^{o}C$ and hence is a likely contribution to the thermal phase drifts. Replacing the aluminum pieces with Invar (thermal expansion coefficient 1.3 x $10^{-6}/^{o}C$) and/or regulating the temperature of the laboratory have been considered as possible solutions to this problem.

Instead, we compensate for these drifts by measuring the zero phase of the interferometer between each applied phase measurement and interpolate away the phase drift. The effects of phase fluctuations are minimized by repeating the measurements many times.

Reanalysis

Addition phase noise

In the original analysis, the effects of the additional phase noise were included by increasing the statistical error of the quadratic fits to the data by the square root of the chisquared of the fit. The principle difference in the reanalysis was to increase the statistical error of each phase measurement by the measured rms phase noise of the interferometer for each run. Although these two methods are equivalent assuming that the additional phase noise is random, we felt it was important to verify the insensitivity of the final value to the method. In Fig. A.2, the fluctuation of the zero phase measurements is shown for the different experimental runs. The long-term drift in the zero-phase has been subtracted off—only the short-term fluctuations are shown. In each case, the rms fluctuation is larger than that expected from counting statistics alone (shot noise). The source of this additional noise is not clear: a possible candidate is short-term (e.g. minute time scale) intensity fluctuations or pointing instabilities in the He-Ne laser.*

---

* We have recently installed large area photodiodes for the laser interferometer signal to minimize the sensitivity to pointing instabilities. We have also installed an additional photodiode to detect the

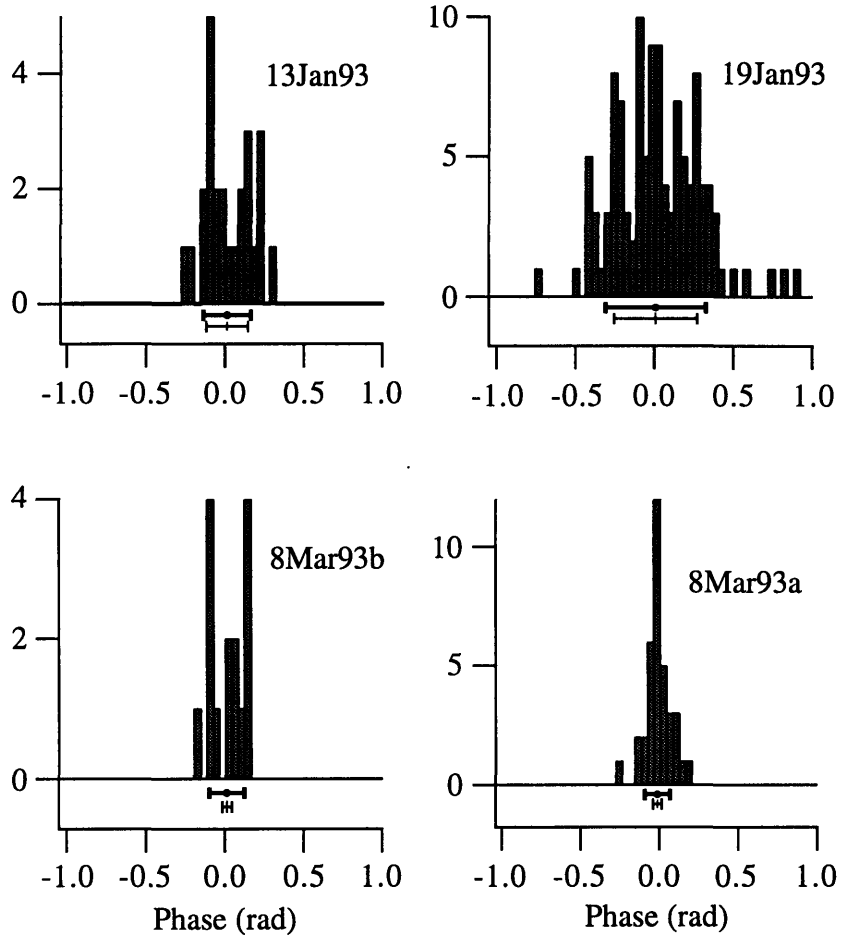

Fig. A.2 The measured zero-phase fluctuation of the atom interferometer for different runs. The dark horizontal error bars indicate the measured rms phase noise, and the light horizontal error bars indicate the rms phase uncertainty due to counting statistics alone (shot-noise).

quadrature component of the laser interferometer as well as an intensity stabilizer to compensate for intensity fluctuations. Preliminary tests do not indicate an improvement in the phase noise although work is still in progress.

Interaction region asymmetry

The other significant difference in the reanalysis was that the data for voltages applied to the different sides of the interaction regions were separately corrected for a small measured asymmetry of spacers of the interaction region (0.1%). In the original analysis, the mean value for the spacers was used for both sides. Again, we expected no significant difference in the final result but felt that the two methods should be compared.

The spacer measurements are shown in Fig. A3. The measured asymmetry of 0.1% is consistent with the small phase shift we measured for voltages applied to the septum of the interaction region (for a perfectly symmetric interaction region, the electric fields would be identical on both sides and the phase shifts on each side would cancel).

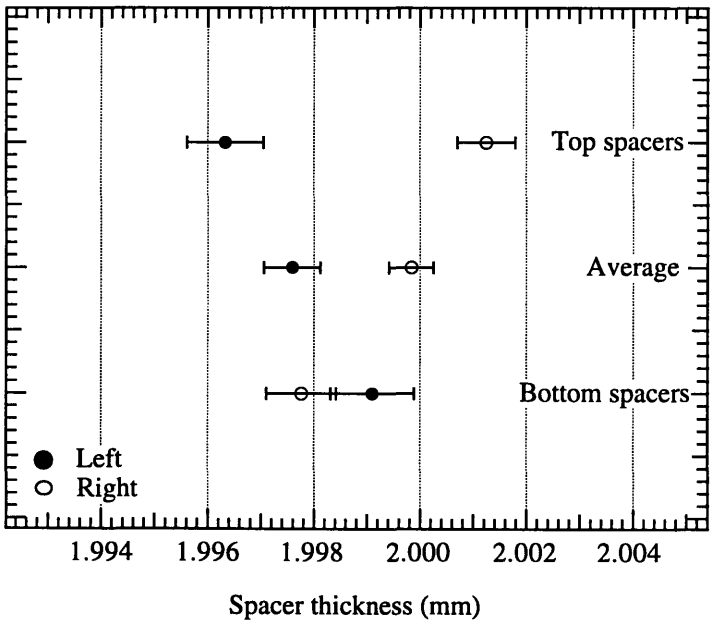

Fig A.3 The measured spacer thickness showing a 0.1% asymmetry in the interaction region.

For a voltage, V, applied to a single side of the interaction region, the phase shift we measure in our experiment is $\Delta\phi = \pm C_2 V^2$ where $C_2 \approx 172 \text{ x } 10^{-6}$ rad per volts

squared is the quadratic coefficient. For the slightly asymmetric spacers we actually used, a voltage applied to the septum should produce a phase shift

$$\Delta\phi_{left} - \Delta\phi_{right} = 4\varepsilon C_2 V^2 \approx 6.9 \text{ x } 10^{-7} V^2$$

where the numerical factor uses the measured $\varepsilon = (d_{left} - d_{right}) / d = 10^{-3}$. This agrees within errors with the measured value of $6.3(1.1) \text{ x } 10^{-7} V^2$ determined from a fit to the data in Fig. A4.

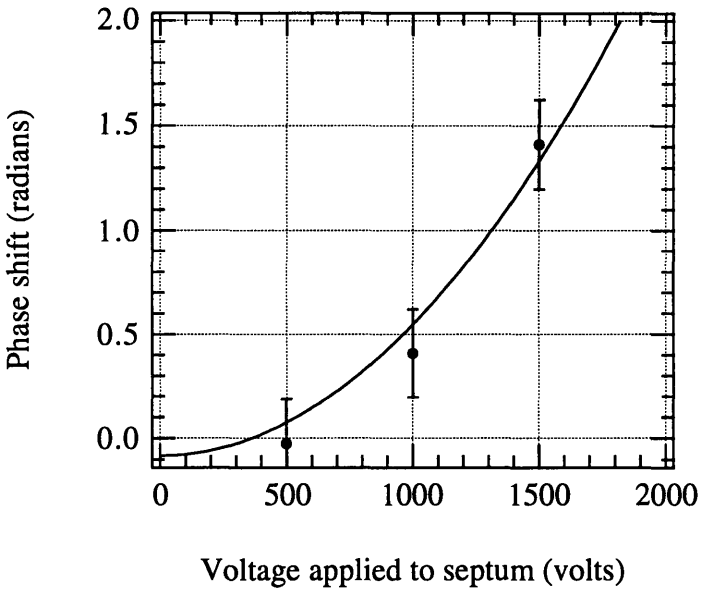

Fig A.4 The measured phase shift for voltage applied to the *septum*. (both side plates held at ground).

Results of reanalysis

In Figs. A5 and A6, the results for the individual runs are plotted for the original analysis and the reanalysis, respectively. In all cases, the differences between values for both individual and collective results are much less than the estimated uncertainty.

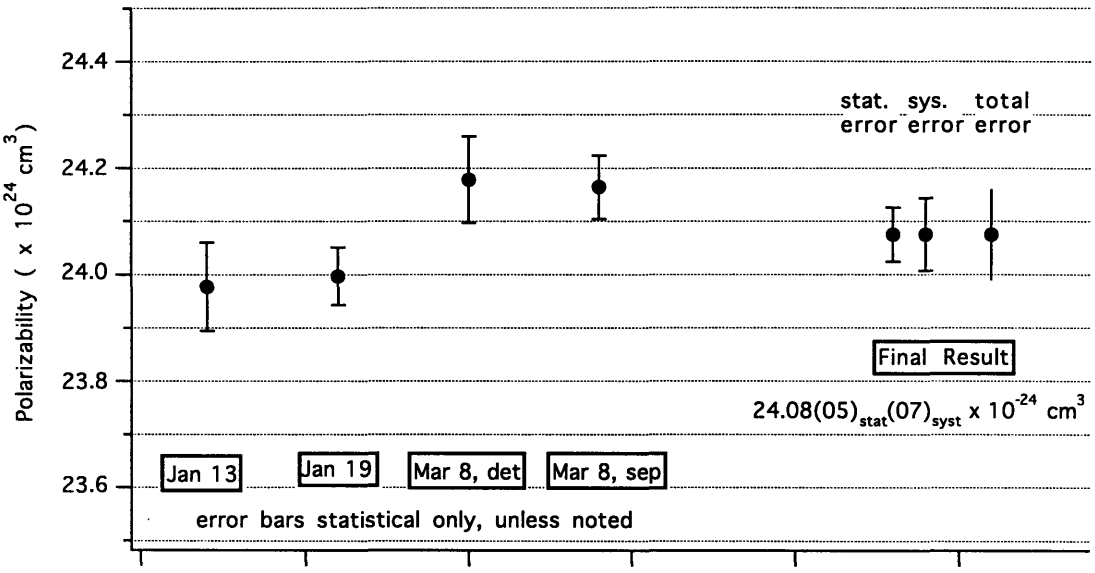

Fig A.5 Original analysis of the data treating left and right data together and accounting for the extra noise in the data by increasing the errors bars at intermediate steps.

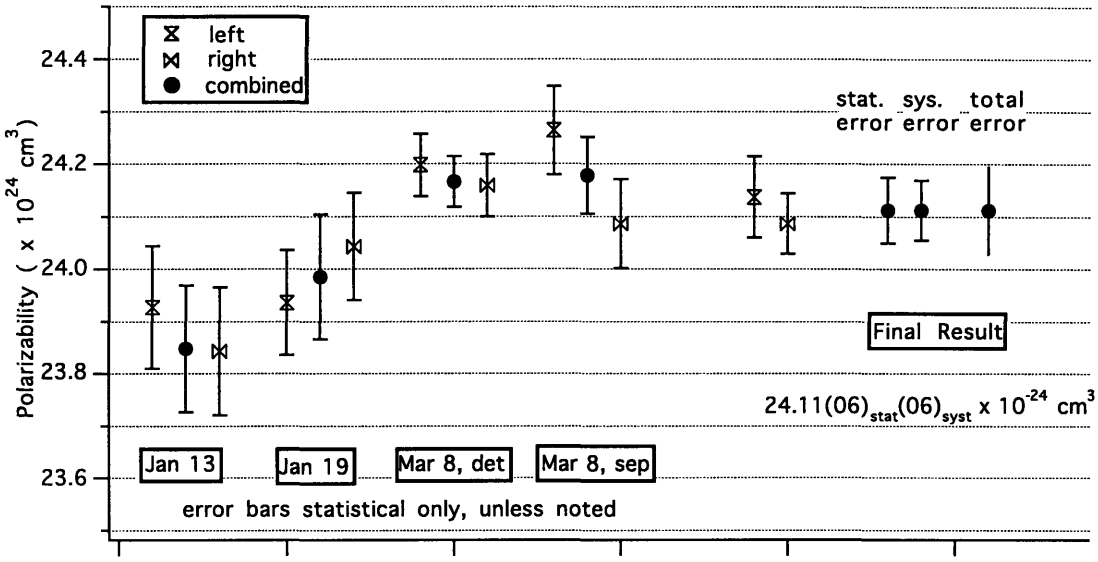

Fig A.6 Reanalysis of the data treating the left and right data separately (i.e. accounting for the 0.02% asymmetry) and increasing the errors bars of the original phase determination of the interference scan.

In Fig A.7, the final results are plotted for different methods of combining the individual measurements. In all cases, the differences are insignificant with respect to the estimated uncertainty of the measurement.

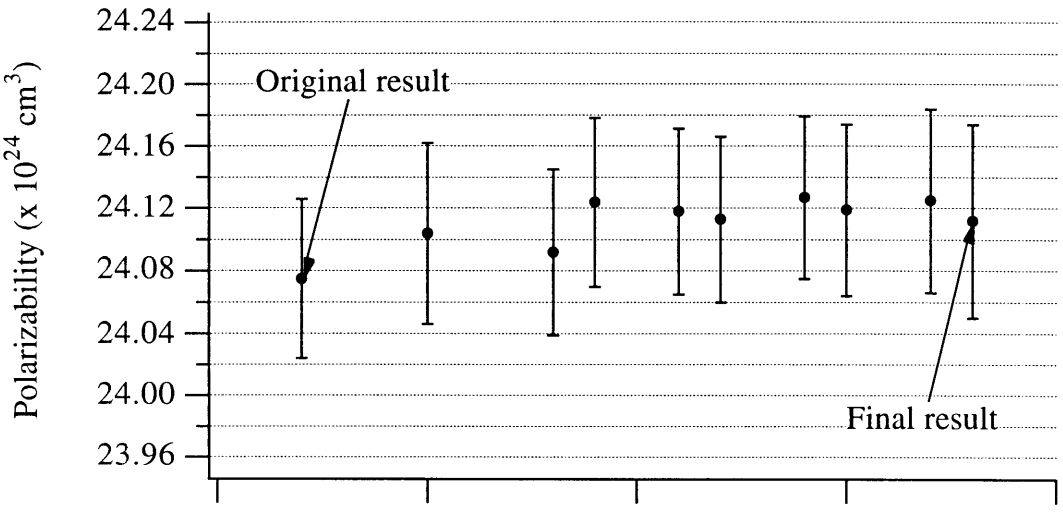

Fig A.7 Various different methods of combining the different results into the final result. The final result (rightmost) is slightly modified with respect to the original, but well within the quoted uncertainty.

Summary

In summary, we have reanalyzed the results of our polarizability measurement, using different methods to account for the additional phase noise in the interferometer and explicitly including the measured asymmetry of the interaction region in the analysis. The results of this reanalysis are in agreement with the original analysis within the errors of the measurement.

Appendix B

B.1 Using a separated beam interferometer to measure tensor components of the electric polarizability of molecules.

The first measurement we undertook with our separated beam atom interferometer was a measurement of the ground state electric polarizability of sodium. By shifting the phase of one arm of the interferometer with a well-characterized electric field, we were able to improve on previous measurements of this important physical property by an order of magnitude. Following the demonstration of a separated beam interferometer for molecules, it seems likely that similar techniques could be used to considerably improve on previous measurements of molecular polarizabilities (of which there are few [MIB88]). In this section, I will describe a possible method for a measurement of both the average and the in- and out-of-plane components.

The electric polarizability for an atom or molecule is generally a tensor object expect for special cases such as atom (like sodium) with spherically symmetric ground states. For homonuclear diatomic molecules such as Na_2, the polarizability tensor has two independent components, $\alpha_\perp$ and $\alpha_\parallel$ referring to the polarizabilities perpendicular and parallel to the molecular axis respectively. Heuristically, one expects $\alpha_\perp$ to be close to the atomic value, while $\alpha_\parallel$ will be modified due to interactions of induced dipoles moments. From these to components, one can define the average polarizability $\overline{\alpha}$

$$\overline{\alpha} = (\alpha_\parallel + 2\alpha_\perp)/3 \tag{B.1}$$

and the polarization anisotropy γ

$$\gamma = \alpha_{\parallel} - \alpha_{\perp} \tag{B.2}$$

The Stark shift of such a molecule is state dependent and can be written

$$\Delta U = \frac{E^2}{2}\left[\overline{\alpha} + \frac{\gamma}{3}\left(\frac{3M^2}{J(J+1)} - 1\right)\right] \tag{B.3}$$

If one could make a careful measurement of this energy shift for 2 or more states, the average polarizability and anisotropy could be uniquely determined. No such measurement has been performed to date for the alkali dimers, however, the average polarizabilities of different alkali dimers have been measured to 10% or so by Molof et al. [MMS74] using molecular beam deflection in a gradient electric field. Their measurements were made relative to the corresponding atomic polarizabilities by comparing the atomic and molecular deflections. Although the alkali dimer anisotropies have yet to be measured, there has been a 10% measurement of the polarizability anisotropy in NaLi [GDW72] using an electric resonance technique.

A separated beam molecular interferometer is a natural tool to measure these properties. The potential shift for an applied uniform electric field is measured directly as a phase shift of the interference fringes. However, because ΔU is state-dependent, an unselected molecular beam will acquire a range of phase shifts with a range proportion to $\Delta U_{\min} = \alpha_{\perp} E^2 / 2$ at the low end and $\Delta U_{\max} = \alpha_{\parallel} E^2 / 2$ at the high end. For Na_2, Müller and Meyer have calculated [MÜM86] $\alpha_{\perp} = 29.2$ and $\alpha_{\parallel} = 55.6$ x $10^{-24}/cm^3$ which gives $\overline{\alpha} = 38$ and $\gamma = 26.4$. The net result would be a dephasing of the atomic interference pattern as the electric field increased. By measuring the loss in contrast as well as the phase shift, it would be possible to determine $\overline{\alpha}$ and γ separately. The loss of contrast is due in part to the state-dependent energy term proportional to γ, however,

there will also be a significant contribution to the loss of contrast due to the average phase shift—this latter contribution is associated with the coherence length of the beam. Hence, using this technique to separately extract $\overline{\alpha}$ and γ is complicated by the fact that the information about the anisotropy must be deconvolved with the loss of contrast due to the mean applied phase shift.

An alternate method we suggest here is to measure the anisotropy directly by applying an electric field to both sides of the interferometer—but pointing in different directions on each side. In this case, the phase shift due to the average polarizability $\overline{\alpha}$ will cancel and the loss of contrast will be entirely due to the state-dependent phase shifts proportional to γ.

To illustrate this idea, it will be convenient to work in the large J (or classical) limit in which we may rewrite Eq. B.3 as

$$\Delta U = \frac{E^2}{2}\left[\overline{\alpha} + \frac{\gamma}{3}\left(3\cos^2\theta - 1\right)\right] \tag{B.4}$$

From this expression, it is easy to understand what we would measure for equal amplitude, but different direction, electric fields applied to both arms of the interferometer. Denoting θ_l and θ_r as the angle of the fields applied to the left and right arms of the interferometer (defined with respect to the molecular axis), we can calculate the difference in potential shift

$$\Delta U_l - \Delta U_r = \frac{E^2}{2}\gamma\left(\cos^2\theta_l - \cos^2\theta_r\right) \tag{B.5}$$

or, defining $-\delta \equiv \theta_l - \theta_r$

$$\Delta U_l - \Delta U_r = \frac{E^2}{2}\gamma\sin(2\theta_l + \delta)\sin\delta \tag{B.6}$$

Now, to calculate the effects of such an interaction on the molecular interference pattern, we have to average over all possible orientations.

$$\begin{aligned} C'\cos(k_g x+\phi') &= \int_0^{\pi} \mathrm{d}\theta_l \cos\left[k_g x + b\sin(2\theta_l+\delta)\sin\delta\right] \\ &= \cos k_g x \int_0^{\pi} \mathrm{d}\theta_l \cos\left[b\sin(2\theta_l+\delta)\sin\delta\right] - \\ &\qquad \sin k_g x \int_0^{\pi} \mathrm{d}\theta_l \sin\left[b\sin(2\theta_l+\delta)\sin\delta\right] \\ &= J_0(b\sin\delta)\cos k_g x \end{aligned} \tag{B.7}$$

where $b = \gamma E^2 \Delta t / 2\hbar$ is the proportionality constant relating the applied field to the phase shift (Δt is the transit time through field region), and $J_0(b\sin\delta)$ is the Bessel function shown in Fig. B.1. The last step in Eq. B.7 results from a change of variables $\beta = 2\theta_l + \delta$ and the integral expression $J_0(x) = \frac{1}{\pi}\int_0^{\pi} \cos(x\sin\beta)d\beta$ (the corresponding sin integral is zero from symmetry considerations).

The argument of the Bessel function is $b\sin\delta$, a factor determined by both the magnitude and the angle difference of the applied field. Hence, this method does not require any specific angle difference as long as $\delta \neq 0, \pi$—for any given angle difference, the contrast will be exhibit the same form, but just at a different field.

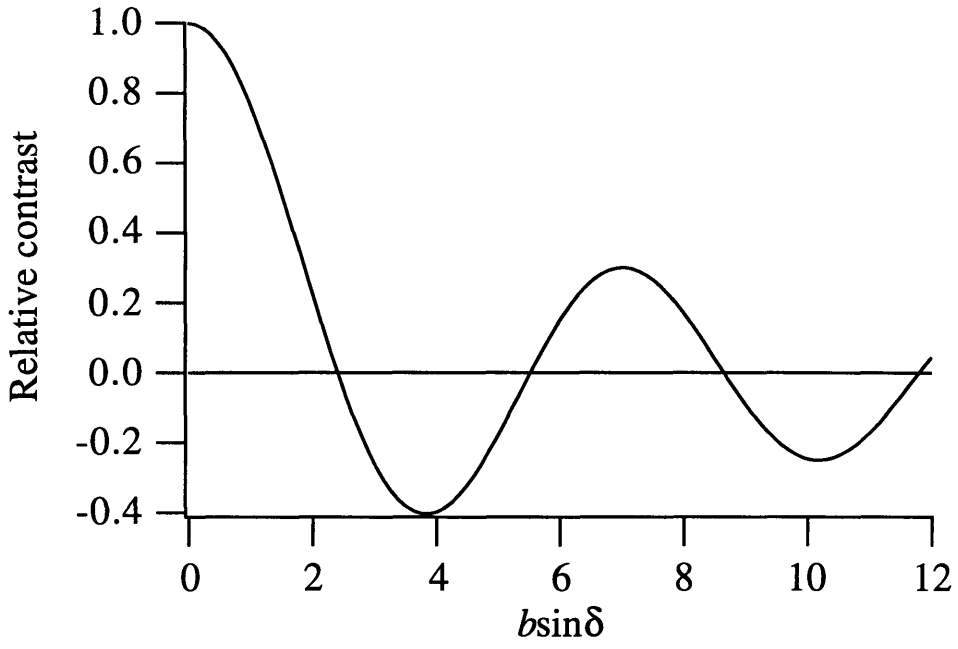

Fig. B.1 The loss in contrast as a function of $b\sin\delta$. The negative contrast values correspond to a π phase shift of the interference pattern.

In summary, we have discussed a new method to measure the anisotropic polarizabilities of dimers such as Na_2 using a separated beam interferometer, and presented a simple calculation illustrating the idea. This work should be extended to the regime of small angular momentum J relevant for supersonic dimer beams.

Acknowledgments

There are many people to thank for their help and support along the way. I would like to thank my parents for their continual support of all of my endeavors. Also, I would like to thank Elizabeth, my wonderful wife and friend, for helping me in so many ways but especially for her encouragement and understanding. Thanks to my brothers and sister, David, Bobby and Sybil and their families for their support and help—I truely appreciate all you have done for me over the years. And thanks also to John and Kathleen for your enthusiasm in my pursuits and your encouragement and support. Thanks of course to my friends scattered across the globe who help keep things in perspective.

I would like to especially thank Dave Pritchard, my advisor. I have had tremendous fun working in his group, and I consider myself very privileged to have learned from such a fine scientist. His physical insight continues to amaze me, and his congeniality and guidance make the laboratory an enjoyable place to do research. I am very grateful for his support during the course of this research, and I will value the experiences I've had here.

This thesis would not have possible without the talented help of my co-workers Troy Hammond, Alan Lenef, Jörg Schmiedmayer, Edward Smith, Richard Rubenstein and Stephan Wehinger. Also special thanks to Chris Ekstrom, my predecessor in this lab. Also, I am grateful for the assistance Bridget Tannian and Amrit Pant, two very talented undergraduate students who helped out in the lab. I have truly enjoyed working with you all, through the all-night (and sometimes all-day) runs and zany experiments and ideas—I wouldn't change a thing.

Special thanks to Mike Rooks at the NNF in Cornell for help in making the atom gratings, and to Quentin Turchette for his help during one of our trips to Cornell.

I have enjoyed much good camaraderie (and much bad coffee) with other the members of the Pritchard group: Mike Bradley, Fred Palmer, Mike Joffe, Frank DiFillipo and Vasant Natarajan.

I would also like to thank Prof. Wolfgang Ketterle and his students : Ken Davis, Marc-Oliver Mewes, and Michael Andrews. Laboratory life would not be nearly so exciting without you. Special thanks to Wolfgang and Ken for help and advice with our laser system. And the Kleppner folk: Robert Lutwak, Jeff Holley, Joel DeVries, Hong Jiao, and Neal Spellmeyer for always being willing to lend a spare piece of equipment or some friendly advice.

I would like Carol Costa for her friendly conversation and administrative assistance—I am very appreciate of all of her help over the last few years. I would also like to thank Peggy Berkowitz for making graduate life a little easier.

Finally, special thanks to Profs. Daniel Kleppner and Tomas Arias for serving on my thesis commitee and for your helpful suggestions.

References

[BCB94] C.J. Bordé, N. Courtier, F.d. Burck, A.N. Goncharov and M. Gorlicki, Phys. Lett. A **188**, 187 (1994). *Molecular interferometry experiments.*

[BEH79] K. Bergmann, R. Engelhardt, U. Hefter and P. Hering, Chem. Phys. **44**, 23 (1979). *Molecular beam diagnostics with internal state selection, II. Intensity distribution of a Na/Na_2 supersonic beam.*

[BOR49] N. Bohr, *A. Einstein: Philosopher - Scientist* (Library of Living Philosophers, Evanston, 1949) p. 200-241 .

[BOR89] C. Bordé, Phys. Lett. A **140**, 10 (1989). *Atomic interferometry with internal state labeling.*

[BOW80] M. Born and E. Wolf, *Principles of Optics* (Pergamon Press, Oxford, 1980) .

[CAL75] B.J. Chang, R. Alferness and E.N. Leith, Applied Optics **14**, 1592 (1975). *Space-invariant achromatic grating interferometers: theory.*

[CAM91] O. Carnal and J. Mlynek, Phys. Rev. Lett. **66**, 2689 (1991). *Young's double slit experiment with atoms: A simple atom interferometer.*

[CBA91] C. Cohen-Tannoudji, F. Bardou and A. Aspect in *Laser Spectroscopy X* , p. 3, edited by M. Ducloy, E. Giacobino and G. Camy (World Scientific, Singapore, 1991).

[CEH95] M.S. Chapman *et al.*, Phys. Rev. A **51**, R14 (1995). *Near field imaging of atom diffraction gratings: the atomic Talbot effect.*

[CLL94] J.F. Clauser and S. Li, Phys. Rev. A **50**, 2430 (1994). *"Heisenberg microscope" decoherence atom interferometery.*

[CLL94] J.F. Clauser and S. Li, Phys. Rev. A **49**, R2213 (1994). *Talbot-vonLau Atom Interferometry with Cold Slow Potassium.*

[CLR89] J.F. Clauser and M.W. Reinsch, App. Phys. B **54**, 380 (1989). *New theoretical and experimental results in Fresnel optics with applications to matter-wave and x-ray interferometry.*

[COM57] J.M. Cowley and A.F. Moodie, Proc. Phys. Soc. B **70**, 486, 497, 505 (1957). *Fourier images.* (a three part article)

[COW75] J.M. Cowley, *Diffraction Physics* (North-Holland, Amsterdam, 1975) .

[CSS91] O. Carnal, M. Sigel, T. Sleator, H. Takuma and J. Mlynek, Phys Rev. Lett. **67**, 3231 (1991). *Imaging and focusing of atoms by a Fresnel zone plate.*

[CTK95] O. Carnal, Q.A. Turchette and H.J. Kimble, Phys. Rev. A **51**, 3079 (1995). *Near-field imaging with two transmission gratings for submicrometer localization of atoms.*

[EKP92] C.R. Ekstrom, D.W. Keith and D.E. Pritchard, App. Phys. B **54**, 369 (1992). *Atom Optics Using Microfabricated Structures.*

[EKS93] C.R. Ekstrom, Ph.D. Thesis, Massachusetts Institute of Technology, 1993. *Experiments with a Separated Beam Atom Interferometer.*

[ESC95] C.R. Ekstrom, J. Schmiedmayer, M.S. Chapman, T.D. Hammond and D.E. Pritchard, Phys. Rev. A **51**, 3883 (1995). *Measurement of the Electric Polarizability of Sodium with an Atom Interferometer.*

[FLS65] R. Feynman, R. Leighton and M. Sands, *The Feynman Lectures on Physics* (Addison-Wesley, Reading, MA, 1965) p. 1-1 Vol. 3.

[FRT78] A.P. French and E.F. Taylor, *An Introduction to Quantum Physics* (W. W. Norton & Co., New York, 1978) Chap. 2 .

[GDW72] J. Graff, P.J. Dagdigian and L. Wharton, J. Chem. Phys. **57**, 710 (1972). *Electric resonance spectrum of NaLi.*

[GLH71] R.J. Gordon, Y.T. Lee and D.R. Herschbach, j. Chem. Phys. **54**, 2393 (1971). *Supersonic molecular beams of alkali dimers.*

[GOU85] P.L. Gould, Ph.D. Thesis, Massachussets Institute of Technology, 1985. *Momentum transfer to atoms by absorption and emission of radiation.*

[HAZ74] W.D. Hall and J.C. Zorn, Phys. Rev. A **10**, 1141 (1974). *Measurement of alkali-metal polarizabilities by deflection of a velocity-selected atomic beam.*

[HCP81] A.M. Hawryluk, N.M. Ceglio, R.H. Price, J. Melngailis and H.I. Smith, J. Vac. Sci. Technol. **19**, 897 (1981). *Gold transmission gratings with submicrometer periods and thicknesses > 0.5 μm.*

[HIB59] E.A. Hiedemann and M.A. Breazeale, J. Opt. Soc. Am. **49**, 372 (1959). *Secondary Interference in the Fresnel Zone of Gratings.*

[HPC95] T.D. Hammond, D.E. Pritchard, M.S. Chapman, A. Lenef and J. Schmiedmayer, App. Phys. B **60**, 193 (1995). *Multiplex Velocity Selection.*

[HSK94] C. Henkel, A.M. Steane, R. Kaiser and J. Dalibard, J. Phys II France **4**, 1877 (1994). *A modulated mirror for atomic interferometry.*

[JAW95] U. Janicke and M. Wilkens, J. Phys. II **4**, 1975 (1994). *Atom Fresnel images and possible applications in atom lithography.*

[KAC91] M. Kasevich and S. Chu, Phys. Rev. Lett. **67**, 181 (1991). *Atomic Interferometry using Stimulated Raman Transitions.*

[KAC92] M. Kasevich and S. Chu, App. Phys. B **54**, 321 (1992). *Measurement of the gravitational acceleration of an atom with a light-pulse interferometer.*

[KEI91] D.W. Keith, Ph.D. Thesis, MIT, 1991. *An Interferometer for Atoms.*

[KET91] D.W. Keith, C.R. Ekstrom, Q.A. Turchette and D.E. Pritchard, Phys. Rev. Lett. **66**, 2693 (1991). *An Interferometer for Atoms.*

[KSR91] D.W. Keith, R.J. Soave and M.J. Rooks, J. Vac. Sci. Technol. B **9**, 2846 (1991). *Free-standing gratings and lenses for atom optics.*

[KSS88] D.W. Keith, M.L. Shattenburg, H.I. Smith and D.E. Pritchard, Phys. Rev. Lett. **61**, 1580 (1988). *Diffraction of Atoms by a Transmission Grating.*

[LAU48] E. Lau, Ann. Phys. (Germany) **6**, 417 (1948). *Beugungerscheinungen an Doppelrastern.*

[LEB69] J.A. Leavitt and F.A. Bills, Am. J. Phys. **37**, 905 (1969). *Single-Slit Diffraction Pattern of a Thermal Atomic Potassium Beam.*

[MAN79] L. Mandel, J. Optics (Paris) **10**, 51 (1979). *Distribution of atomic momentum in resonance flourescence.*

[MAR87] P.J. Martin, Ph.D. Thesis, M.I.T., 1987. *Momentum transfer to atoms moving through a standing wave of light.*

[MAT74] E.M. Mattison, Ph.D. Thesis, M.I.T., 1974. *Molecular beam study of van der Waals molecules: Spin-rotation interaction in potassium-argon.*

[MIB88] T.M. Miller and B. Bederson, Adv. At. Mol. Phys. **25**, 37 (1988). *Electric dipole polarizability measurements.*

[MIG77] A.L. Migdall, Ph.D. Thesis, M.I.T., 1977. *A study of low temperature rotationally inelastic collisions in a supersonic expansion.*

[MIM87] A.A. Michelson and E.W. Morley, Phil. Mag. **24**, 449 (1887).

[MMS74] R.W. Molof, T.M. Miller, H.L. Schwartz, B. Bederson and J.T. Park, J. Chem. Phys. **61**, 1816 (1974). *Measurements of the average electric dipole polarizabilities of the alkali dimers.*

[MOD54] G. Mollenstedt and H. Duker, Naturwissenschaften **42**, 41 (1954). *Frensnelscher interferenzversuch mit einem biprisma fur elektronenwellen.*

[MOW84] P.E. Moskowitz, Ph.D. Thesis, M.I.T., 1984. *The diffraction of an atomic beam by standing wave radiation.*

[MSM74] R.W. Molof, H.L. Schwartz, T.M. Miller and B. Bederson, Phys. Rev. A **10**, 1131 (1974). *Measurements of electric polarizabilities of the alkali-metal atoms and the metastable noble-gas atoms.*

[MÜM86] W. Müller and W. Meyer, J. Chem. Phys. **85**, 953 (1986). *Static dipole polarizabilities of Li_2, Na_2 and K_2.*

[OLD90] B.G. Oldaker, Ph.D. Thesis, M.I.T., 1990. *Multi-photon momentum transfer from light to atoms.*

[PAT89] K. Patorski in *Progress in Optics* , XXVII, p. 1-108, edited by E. Wolf (North-Holland, Amsterdam, 1989).

[PSK94] T. Pfau, S. Spalter, C. Kurstsiefer, C.R. Ekstrom and J. Mlynek, Phys. Rev. Lett. **29**, 1223 (1994). *Loss of Spatial Coherence by a Single Spontaneous Emission.*

[RAM85] N.F. Ramsey, *Molecular Beams* (Oxford University Press, Oxford, 1985) .

[RAY81] L. Rayleigh, Philos. Mag. **11**, 196 (1881). *On copying diffraction-gratings, and on some phenomena connected therewith.*

[RKW91] F. Riehle, T. Kisters, A. Witte, J. Helmcke and C.J. Bordé, Phys. Rev. Lett. **67**, 177 (1991). *Optical Ramsey Spectroscopy in a Rotating Frame: Sagnac Effect in a Matter-Wave Interferometer.*

[RMB91] J. Robert, C. Miniatura, S.L. Boiteux, J. Reinhardt, V. Bocvarski and J. Baudon, Europhys. Lett. **16**, 29 (1991). *Atomic Interferometery with Metastable Hydrogen Atoms.*

[RTB74] H. Rauch, W. Treimer and U. Bonse, Phy. Lett. **47A**, 369 (1974). *Test of a single crystal neutron interferometer.*

[RWK92] F. Riehle, A. Witte, T. Kisters and J. Helmcke, Appl. Phys. B **54**, 333 (1992). *Interferometry with Ca atoms.*

[SAI90] A. Stern, Y. Aharonov and Y. Imry, Phys. Rev. A **41**, 3436 (1990). *Phase uncertainty and loss of coherence: A general picture.*

[SCE95] J. Schmiedmayer, M.S. Chapman, C.R. Ekstrom, T.D. Hammond, S. Wehinger and D.E. Pritchard, Phys. Rev. Lett. **74**, 1043 (1995). *Index of refraction of various gases for sodium matter waves.*

[SCP91] T. Sleator, O. Carnal, T. Pfau, A. Faulstich, H. Takuma and J. Mlynek in *Laser Spectroscopy X* , p. 264, edited by M. Dulcoy, E. Giacobino and G. Camy (World Scientific, Singapore, 1991).

[SEC93] J. Schmiedmayer, C.R. Ekstrom, M.S. Chapman, T.D. Hammond and D.E. Pritchard in *Fundamentals of Quantum Optics III, Küthai, Austria, 1993,*

[SEC94] J. Schmiedmayer, C.R. Ekstrom, M.S. Chapman, T.D. Hammond and D.E. Pritchard, J. Phys. II France **4**, 2029 (1994). *Magnetic coherences in atom interferometry.*

[SER80] J.A. Serri, Ph.D. Thesis, MIT, 1980. *Angular distributions for rotational energy transfer.*

[SSM92] U. Sterr, K. Sengstock, J.H. Muller, D. Bettermann and W. Ertmer, Appl. Phys. B **54**, 341 (1992). *The Magnesium Ramsey interferometer: applications and prospects.*

[SST92] F. Shimizu, K. Shimizu and H. Takuma, Jpn. J. Appl. Phys. **31**, L436 (1992). *Stark Phase Shift and Deflection in the Ultracold Atomic Interferometer.*

[STC94] P. Storey and C. Cohen-Tannoudji, J. Phys. II France **4**, 1999 (1994). *The Feynman path integral approach to atomic interferometry. A tutorial.*

[TAL36] H.F. Talbot, Philos. Mag. **9**, 401 (1836). *Facts relating to optical science.*

[TAW93] S.M. Tan and D.F. Walls, Phys. Rev. A **47**, 4663 (1993). *Loss of coherence in interferometry.*

[TPK92] Q.A. Turchette, D.E. Pritchard and D.W. Keith, JOSA B **9**, 1601 (1992). *Numerical model of a multiple-grating interferometer.*

[TUR91] Q.A. Turchette, Ph.D. Thesis, MIT, 1991. *Numerical Model of a Three Grating Interferometer for Atoms.*

[WEI78] M. Weissbluth, *Atoms and Molecules* (Academic Press, San Diego, 1978) p. 503 .

[WIW65] J.T. Winthrop and C.R. Worthington, J. Opt. Soc. Am. **55**, 373 (1965). *Convolution formulation of Fresnel diffraction.*

[WOZ79] W. Wooters and W. Zurek, Phys. Rev. D **19**, 473 (1979). *Complementarity in the double-slit experiment: Quantum non-separability and a quantitative statement of Bohr's principle.*

[WYC93] D.S. Weiss, B.N. Young and S. Chu, Phys. Rev. Lett. **70**, 2706 (1993). *Precision Measurement of the Photon Recoil of an Atom Using Atomic Interferometry.*

[WYC94] M. Weitz, B.C. Young and S. Chu, Phys. Rev. Lett. **73**, 2563 (1994). *Atomic interferometer based on adiabatic population transfer.*

[ZEI86] A. Zeilinger in *New Techniques an Ideas in Quantum Mechanics* , p. 164, edited by (New York Acad. Science, New York, 1986).